THEORETICAL AND EXPERIMENTAL INVESTIGATION OF MAGNETIC FIELD ASSISTED HOT FILAMENT CHEMICAL VAPOUR DEPOSITION FOR DIAMOND COATED TOOLS

KWOK FUNG MING

PhD

The Hong Kong Polytechnic University

2026

The Hong Kong Polytechnic University

Department of Industrial and Systems Engineering

Theoretical and Experimental Investigation of Magnetic Field Assisted Hot Filament Chemical Vapour Deposition for Diamond Coated Tools

Kwok Fung Ming

A thesis submitted in partial fulfilment of the requirements for the degree of Doctor of Philosophy

July 2025

CERTIFICATE OF ORIGINALITY

I hereby declare that this thesis is my own work and that, to the best of my knowledge and belief, it reproduces no material previously published or written, nor material that has been accepted for the award of any other degree or diploma, except where due acknowledgement has been made in the text.

_____ (Signed)

KWOK Fung Ming (Name of student)

Abstract

This research presents an innovative approach to diamond coating by integrating magnetic fields into the Hot Filament Chemical Vapor Deposition (HFCVD) process. This novel method addresses the traditional challenges of HFCVD, such as slow growth rates and inconsistent film uniformity, by leveraging magnetic fields to enhance efficiency and quality in diamond coating technology.

The study begins by optimizing key parameters of the HFCVD process, including methane concentration, substrate temperature, and chamber pressure. Through experimental design, response surface methodology, and parameter optimization, significant improvements in film uniformity and growth kinetics were achieved. After obtaining the optimum coating parameters for diamond film in HFCVD, an application of magnetic field in HFCVD is demonstrated. Notably, applying a 400 mT magnetic field increased diamond nucleation rates by 45% and overall growth rates by nearly 45%, crucial for producing high-quality, consistent films for industrial applications. Incorporating a magnetic field during the HFCVD process also enhanced the structural and morphological characteristics of the diamond films. The magnetic field facilitated the formation of larger, more uniform columnar grains with a dominant (111) crystallographic orientation, known for superior mechanical strength and thermal conductivity. These properties are advantageous for high-performance applications, such as cutting tools and thermal management systems. The research further explored the impact of rotational dynamics in the magnetic field system during deposition. Rotating the magnetic field at speeds up to 2 RPM significantly improved the uniformity and thickness of the diamond films, addressing issues related to non-uniform magnetic influence and plasma stability common in static configurations. Additionally, various magnetic field configurations, including balanced and

unbalanced setups, were investigated. The South-North (SN) orientation proved particularly effective in promoting uniform grain size and consistent coating thickness.

Complementing the experimental work, comprehensive Finite Element Modelling (FEM) was employed to analyse the effects of magnetic fields on temperature distribution and reactive gas flow within the HFCVD reactor. The simulations demonstrated that the magnetic field optimized the distribution of reactive species, improved plasma stability, and ensured a uniform temperature profile across the substrate, providing predictive insights into optimal conditions for diamond film growth.

This study significantly advances HFCVD technology by demonstrating the potential of magnetic field assistance in diamond coating. It promises to reduce production costs, increase productivity, and enhance the performance of cutting tools, particularly in specialized applications. The successful integration of this technology offers high levels of efficiency and quality, reshaping the landscape of cutting tool manufacturing and beyond.

Publication arising from this study

Journal papers

1. **Kwok, F. M.**, Sun, Z., Yip, W. S., Kwok, K. Y. D., & To, S. (2022). Effects of Coating Parameters of Hot Filament Chemical Vapour Deposition on Tool Wear in Micro-Drilling of High-Frequency Printed Circuit Board. *Processes*, 10(8).
2. **Kwok, F. M.**, Du, X., Sun, Z., Ng, M. C., Liu, Q., Luo, F. L., Yip, W. S., Kwok, D. K. Y., & To, S. (2024). Fabrication of diamond film under low methane concentration by hot filament chemical vapor deposition with magnetic field assistance. *Surface and Coatings Technology*, 483, 130802.
3. **Kwok, F. M.**, Du, X., Sun, Z., Ng, M. C., Yip, W. S., Kwok, K. Y. D., & To, S. (2025). Investigation of rotational magnetic field assisted hot filament chemical vapor deposition for diamond film growth. *Surface and Coatings Technology*, *495*, 131588.

Conference papers

1. **Kwok, F. M.**, & To, W. S. Y. S. (2022). Hot filament chemical vapour deposition on tungsten carbide milling tools with magnetic field assistance. ASPEN 2022.

Acknowledgements

First and foremost, I would like to express my deepest gratitude to my wife, Sarunchana Viputsakul, for her unwavering support throughout this journey. Her patience, encouragement, and assistance in numerous aspects of life during my research period have been invaluable. Without her, this achievement would have been much harder to reach.

I am sincerely grateful to my supervisor, Prof. Sandy To, and co-supervisor, Prof. Lenny Yip, for their guidance, encouragement, and insightful discussions. Their expertise, invaluable advice, and constructive suggestions have greatly influenced my research and allowed me to explore innovative ideas. Their mentorship has been instrumental in shaping both my academic and personal growth.

I would also like to extend my heartfelt appreciation to my family, especially my mum, dad and sister, for their unwavering support and belief in me. Their encouragement and assistance throughout my academic journey have been the foundation of my success. I would not be where I am today without them.

Furthermore, I would like to acknowledge my research group members, the staff at State Key Laboratory of Ultra-precision Machining Technology, and my friends. Their support, collaboration, and shared experiences have made my research journey not only intellectually stimulating but also enjoyable. I deeply appreciate the friendships and the memorable moments we have shared.

Finally, I want to thank everyone who has supported me in any way throughout this journey. Your kindness and encouragement have meant more than words can express.

Table of contents

List of figures

List of tables

List of acronyms

AFM=Atomic force microscopy

CFRP=Carbon fibre reinforced plastic

CNC=Computer numerical control

CMP=Chemical mechanical polishing

CVD=Chemical vapour deposition

DI=Deionised

FEM=Finite element method

FWHM=Full width at half maximum

HRC-DB=Daimler-Benz Rockwell-C adhesion test

HFCVD=Hot filament chemical vapour deposition

Lc=Critical load

MA=Magnetic assisted

MCD=Microcrystalline diamond

MEFC=Magnetic and electric fields coupling

MF=Magnetic field

MMC=Metal matrix composite

NCD=Nanocrystalline diamond

PCB=Printed circuit board

PCD=Polycrystalline diamond

PDI=Polydispersity index

PMF=Periodic magnetic field

PVD=Physical vapour deposition

RPM=Revolutions per minutes

SCCM=Standard cubic centimetres per minute

SEM=Scanning electron microscope

SmCo=Samarium-cobalt

SP2=Graphitic carbon bond

SP3=Diamond-like carbon bond

TiN=Titanium nitride

UTGM=Ultra-thin glass moulding process

WC-Co=Tungsten carbide-cobalt

ZrO_2=Zirconium dioxide

3D=Three-dimensional

Chapter 1 Introduction

1.1 Research background

In recent years, the development of advanced materials has led to significant improvements in product performance across various industries. However, as materials evolve to exhibit superior properties such as increased hardness, stiffness, and toughness, the challenges associated with manufacturing and processing these materials have also intensified. These challenges are particularly pronounced in the machining of 'difficult-to-cut' materials, which not only demand more robust manufacturing techniques but also result in higher production costs. These increased costs can impact the financial viability of manufacturing operations, highlighting the need for more efficient and cost-effective processing methods.

Diamond, known for its exceptional mechanical, physical, and chemical properties, has emerged as a promising material for addressing these challenges. Diamond films are valued for their high thermal conductivity, extreme hardness, high electrical resistivity, and chemical stability, making them suitable for a variety of applications, including electronic devices, cutting tools, and thermal management systems. Additionally, diamond films are resistant to wear and chemical deterioration, making them advantageous for use in harsh environments (Auciello & Aslam, 2021; Auciello & Sumant, 2010; Montes-Gutiérrez et al., 2018; Shen & Sun, 2009).

The HFCVD technique is widely used to grow diamond films by decomposing hydrocarbon gases, such as methane, in the presence of a hot filament. This process results in the deposition of carbon atoms on a substrate surface to form diamond crystals. The growth rate and grain size of the deposited films are significantly influenced by activated radicals and ions derived from the decomposition of methane

(CH_4) and hydrogen (H_2) molecules (Roy et al., 2002; Yu et al., 1997). Despite its widespread application, the HFCVD process faces challenges in producing high-quality diamond films with good crystalline quality and smooth surfaces, particularly under low methane concentrations. The reduced availability of carbon atoms in such environments makes it difficult to achieve a high density of nucleation sites, which is crucial for good crystalline quality (May et al., 1993; H. Wang et al., 2021; Wang et al., 2015).

Various strategies have been explored to improve the HFCVD process, including the selection of different precursor gases (e.g., acetone, methane, methanol), filament materials (e.g., tantalum, tungsten), along with surface pre-treatment techniques applied to the substrate (Kwok et al., 2022; Moustakas, 1989). Bias-assisted HFCVD has shown potential in enhancing the nucleation rate, but it also presents challenges, such as the antenna effect (edge effect), which can lead to uneven temperature distribution and potential overheating, particularly on complex geometries like cutting tools (Bohlmark et al., 2011; Kubečka et al., 2019; Macak et al., 2003).

Recent research has focused on the addition of magnetic fields in HFCVD as a novel approach to improving the growth rate and quality of diamond films(Long et al., 2015; Wang et al., 2016; Wang et al., 2018; You et al., 2009). However, there is still a lack of understanding regarding the effects of permanent magnetic fields within the HFCVD process. Previous studies have typically positioned magnetic field systems outside the reaction chamber due to the extreme temperatures inside the HFCVD machine, resulting in weak magnetic flux densities within the reaction zone (Li et al., 2017; Liu et al., 2023; Wang et al., 2017; Wu et al., 2012). Installing magnets inside the HFCVD machine, closer to the tungsten carbide tool, could potentially offer several advantages, including a stronger and more localized magnetic field in the coating zone.

This setup may allow for better control over the deposition process, potentially overcoming the limitations associated with external magnetic field systems. However, the effects of an internal permanent magnetic field system within the HFCVD chamber have not been thoroughly studied.

This research aims to investigate the impact of magnetic fields, including rotational permanent magnets with varying magnetic field configurations, on diamond film growth during HFCVD under low methane concentrations. Additionally, it aims to elucidate the underlying coating mechanisms. By examining the growth rate, film quality, and other properties of diamond films grown with and without magnetic field assistance, this study seeks to fill a gap in understanding the influence of localized magnetic fields on HFCVD processes. Specifically, understanding these fields is crucial for improving deposition uniformity, enhancing growth rates, and ensuring better film quality, which are all essential for high-performance applications. The lack of comprehensive studies on the internal positioning of permanent magnetic fields in HFCVD represents a significant gap in the existing literature, particularly in terms of how these fields directly influence deposition characteristics and film quality.

Both experimental and simulation approaches are employed to gain insights into how magnetic fields, particularly those generated by rotational permanent magnets, affect reactive gas species in HFCVD processes, including temperature distribution, gas flow dynamics, and chemical species concentration, and how these factors influence diamond deposition. The findings from this research are expected to contribute to the development of more efficient and controlled diamond deposition techniques, with significant potential applications in various industrial sectors. Specifically, this research provides a deeper understanding of the role of magnetic field

positioning within the HFCVD reactor, offering potential advancements in deposition uniformity, growth rates, and overall film quality.

1.1.1 Application scenarios and tools improved by diamond films

Diamond films support industrial use because the combination of high hardness, strong abrasion resistance, chemical stability, and, in many cases, high thermal conductivity can be transferred onto engineering substrates through a thin coating. Performance gains are most apparent in applications limited by wear, edge degradation, local overheating, or rapid surface damage.

Diamond-coated tools are widely used when conventional hard coatings cannot provide sufficient abrasion resistance, for example during machining of aluminium alloys with high Si content, metal matrix composites, fibre-reinforced polymers, and filled PCB materials. In such cases, diamond coatings reduce flank wear and crater wear, improve edge retention, and stabilise surface finish. For micro-drills and other small-feature tools, coating uniformity becomes a dominant factor because small variations in thickness or grain size change cutting-edge geometry and promote local heat generation, which accelerates chipping. Process improvements that increase coating uniformity and repeatability therefore translate directly into longer tool life and more consistent hole or surface quality.

Diamond films improve durability of sliding or contacting parts such as guides, bearing surfaces, seals, and precision components that operate under limited lubrication or in contaminated environments. The primary value comes from reduced abrasive wear and slower performance drift over time. Adhesion, surface morphology, and coating continuity remain critical, since local defects often become initiation sites for coating failure.

High thermal conductivity diamond films are attractive for thermal management, including heat spreading layers and coatings on substrates exposed to intense local heating. Film quality and thickness uniformity influence thermal performance, thermal stress, and reliability during thermal cycling. Deposition approaches that reduce temperature gradients and maintain uniform growth are therefore valuable for practical integration.

Diamond films provide chemical inertness in many environments and can protect surfaces against corrosion or erosion. Examples include components exposed to reactive gases, plasma environments, or particle-laden flows. For such uses, coating density, defect population, and coverage of edges and corners often matter more than maximum growth rate.

Across these application scenarios, recurring requirements of reliable nucleation and adhesion, uniform thickness and microstructure over complex geometries, sufficient growth rate for practical coating thickness, and stable thermal conditions during deposition. These requirements motivate process strategies that improve mass transport and temperature distribution in hot filament chemical vapour deposition. Magnetic-field assistance provides a route to enhance growth kinetics while improving coating uniformity, aligning with the objectives of this work.

1.2 Research objectives

The primary aim of this research is to enhance the understanding and optimization of HFCVD for diamond coatings, with a particular emphasis on the role of magnetic fields. This research is driven by the increasing technological demands in advanced material applications. The specific objectives are as follows:

This research aims to advance the understanding and optimization of HFCVD for diamond coatings through several key objectives. Firstly, the study seeks to establish correlations between coating properties, such as thickness and grain size, and standard coating parameters, including temperature, pressure, and gas flow. These parameters are critical as they directly affect the deposition environment, impacting nucleation rate, coating uniformity, and overall film quality. Understanding these relationships is fundamental for optimizing coating quality and performance.

Additionally, the research addresses the challenge of diamond film growth under low methane conditions in HFCVD. By employing magnetic field assistance, the study aims to enhance growth rate, film quality, and overall performance, particularly under low methane conditions. Understanding the influence of magnetic fields on chemical processes and nucleation is crucial for improving film properties.

Another objective is to characterize the influence of magnetic field orientation and dynamic rotation on the deposition characteristics of diamond films. The study investigates the effects of different magnetic field orientations, such as north-north, south-south, and south-north, and examines the combined effects of magnetic field orientation and rotation on the uniformity, crystal structure, and growth rate of the films. This research aims to uncover the potential of magnetic fields to enhance the uniformity and quality of diamond film growth.

Finally, the research aims to develop a comprehensive Finite Element Method (FEM) framework to simulate temperature distribution and chemical transport mechanisms in magnetic field-assisted HFCVD. The FEM simulations will predict the quality and characteristics of diamond coatings under various process parameters, such as temperature, gas flow, and magnetic field intensity. The simulation results will be validated against experimental data to ensure robustness and accuracy, providing

insights into any discrepancies and refining predictive capabilities. By achieving these objectives, the research seeks to offer improved deposition techniques, enhanced film uniformity, and better tool wear resistance, ultimately contributing to advancements in industrial processes.

In addition to validating experimental observations, the FEM framework is developed to provide insight and predictive capability for process optimisation. The model can be used to examine the influence of magnetic configuration and operating parameters on coating uniformity and growth rate, and to identify conditions that minimise temperature gradients and edge-related non-uniformity.

1.3 Thesis outline

This report is structured into six chapters, offering a comprehensive exploration of the role of magnetic fields in the Hot Filament Chemical Vapour Deposition (HFCVD) process for diamond coatings.

Chapter 1: Introduction provides an overview of the HFCVD process and the challenges currently limiting the effectiveness of diamond coatings. The proposed solution of integrating magnetic fields into the HFCVD process is introduced, setting the roadmap for the following chapters.

Chapter 2: Literature Review delves into the fundamental mechanisms of the HFCVD process, the influence of pre-treatment and equipment parameters on diamond coating attributes, and the definition and relevance of "difficult-to-cut material." The chapter also reviews established methods for evaluating diamond film quality and the potential of magnetic fields in improving the HFCVD process.

Chapter 3: High-Frequency PCBs and Tool Wear focuses on the first paper. It investigates the interrelationships among tool wear rate, diamond coating thickness, and grain size, with particular focus on their effects during the machining of fifth-

generation PCBs. The chapter details the challenges of 5G PCB designs, the role of ceramic particles, and the potential of HFCVD-coated drills in addressing these challenges.

Chapter 4: Diamond Films under low methane concentration delves into the second paper's content. It explores the challenges and intricacies of achieving high-quality diamond films under low methane concentrations in HFCVD. The chapter highlights the role of magnetic fields in potentially enhancing the quality and growth rate of these films.

Chapter 5: Influence of magnetic field orientations and rotation in HFCVD is dedicated to the third paper. It investigates the effects of different static magnetic field orientations and the rotation of the magnetic field system on diamond film growth. The chapter also touches upon the potential of the FEM in simulating and understanding these effects.

Chapter 6: Conclusion and Future Directions sums up the research findings from all three studies and their collective contribution to the broader knowledge base in the domain of HFCVD with magnetic fields. Suggestions for potential future research are made, with an emphasis on expanding the application of the findings.

Chapter 2 Literature review

2.1 Introduction

Diamond exhibits a unique giant covalent structure where each carbon atom is bonded to four others via covalent bonds. This arrangement leads to a regular tetrahedral configuration, as depicted in Figure 2.1. The bond distance between adjacent carbon atoms is approximately 0.15 nm (Gracio et al., 2010).

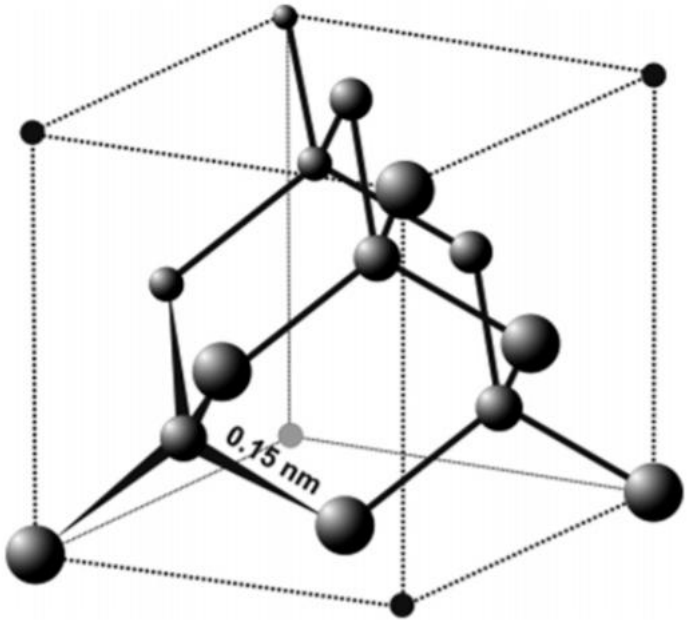

Figure 2.1 Diamond sp^3 structure (Gracio et al., 2010).

For methane to decompose on the diamond surface, it necessitates a substantial activation energy, typically ranging between 230-243 kJ/mol (Gracio et al., 2010). To facilitate this, various CVD enhancement techniques employ methods like thermal, plasma, or combustion processes to dissociate carbon-containing compounds. These processes effectively isolate the reactant species vital for diamond nucleation and subsequent growth. Among the multitude of diamond deposition techniques, HFCVD stands out as one of the most straightforward and consistent methods. Its scalability, combined with a typically lower operational cost compared to alternative diamond

deposition approaches, makes it an attractive choice. The core components of an HFCVD setup include a power source, a filament (typically made of tungsten or tantalum), and a gas source. Nonetheless, the efficiency of HFCVD is often found to be lower than plasma-enhanced CVD methods. To address this shortcoming, integrating a magnetic field assistance system into the HFCVD mechanism has been proposed to bolster its efficiency.

Research has indicated that a reduced gas chamber pressure during HFCVD is beneficial for nucleation in the early stages of diamond grain growth. Specifically, during the initial nucleation phase, the nucleation density sees a marked increase when the reactor pressure is reduced (Das & Singh, 2007). However, at higher pressures, the aggressive plasma, predominantly consisting of hydrogen atoms, tends to degrade the nuclei formed on the substrate. Conversely, elevated pressure conditions can be favourable for enhancing the grain growth rate during the deposition phase. This enhancement is attributed to the increased concentration of reactive species in the dense plasma, especially when a bias system is employed.

Previous studies on machine parameters have also been conducted on processing pressure, temperature and chemical concentration. Among these, substrate temperature and CH_4 concentration have been identified as pivotal determinants of both the growth rate and the overall quality of diamond films.

2.2 Pre-treatment for HFCVD coating process

The HFCVD process for diamond coating involves two principal phases: the initial pre-treatment and the subsequent diamond film growth. The primary goal of pre-treatment is to introduce diamond seeds within the substrate, which are crucial for initiating the growth of the diamond film. This seeding step must be executed before the commencement of the diamond coating phase.

Enhancing the density of nucleation sites on the surface has been shown to mitigate morphological irregularities and diminish the surface roughness of the diamond films. Moreover, a heightened nucleation density fosters the uniformity of the films and curtails the development of voids at the interface between the substrate and the coating layers, thereby bolstering the adhesion quality. This correlation between surface nucleation density and film properties was highlighted in the research of Liu and Dandy (Liu & Dandy, 1995).

Subsequent work by Liu & Dandy (1995) provided a comprehensive overview of how various surface pre-treatment techniques influence the nucleation density, as encapsulated in Table 2.1 of the study. They observed that untreated substrates exhibit a relatively low nucleation density, ranging from $10^3 - 10^5\ cm^{-2}$. In response, several pre-treatment methods underwent review, with effectiveness in enhancing nucleation density measured.

Table 2.1 Summaries different methods of nucleation density (Liu & Dandy, 1995).

Pretreatment Method	**Nucleation Density (cm^{-2})**
No pretreatment	10^3–10^5
Scratching	10^6–10^{10}
Ultrasonic scratching	10^7–10^{11}
Seeding	10^6–10^{10}
Biasing	10^8–10^{11}
Covering/Coating with	
Fe film	4.84×10^5
Graphite film	10^6
Graphite fiber	$>10^9$
a-C film (first scratched)	3×10^{10}
C_{70} clusters + biasing	= seeding effect
Y-ZrO_2, a-BN, cSiC layer	Enhancement
C^+ ion implantation on Cu	Enhancement
Ar^+ ion implantation on Si	10^5–10^6
Pulsed laser irradiation + coating a-C, WC, cBN layer	Enhancement
Carburization	Enhancement

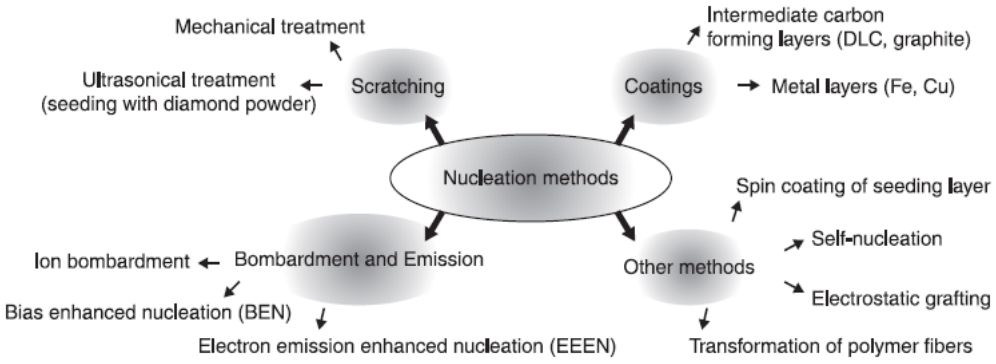

Figure 2.2 Coating Film Nucleation (Kromka et al., 2013).

Kromka et al. (2013) further expanded on this topic by categorizing pre-treatment methods into three distinct groups, as illustrated in Figure 2.2. These categories include electron bombardment of surfaces, involving use of energetic ions to create nucleation sites; application of a thin interlayer on substrates prior to final coating, serving as a preparatory layer; and mechanical pre-treatments, entailing abrasion of substrate surfaces through particles in an ultrasonic bath to generate nucleation sites.

2.2.1 Cobalt removal using chemical reagents

Several pre-treatment methods have been studied with the primary aim to reduce the cobalt content in tungsten carbide (WC) tools and increase surface roughness of the cemented carbides so as to maximise adhesion of diamond coating films. This can generally be done in two ways: using reagents to remove the cobalt (Co) composition or creating an interlayer film between the substrate with cobalt composition and the diamond film.

Cobalt serves as a binder phase within WC grains, significantly contributing to the toughness of WC-Co composites. In the carbon-cobalt (Co-C) system phase diagram, carbon exhibits considerable solubility (0.2–0.3 wt. %) and diffusivity in

cobalt, particularly under the typical diamond growth temperatures of 700 – 1000 °C, as noted by Polini (2006). The solubility and diffusion behaviour of cobalt promote the catalytic formation of graphitic, non-diamond phases at the early stages of diamond film deposition (Polini et al., 2010). Removal of cobalt on the substrate's surface is required as it will influence formation of the diamond film onto the said surface. Without carrying out this critical step, the cobalt will chemically react with the carbon source to form graphite (sp^2) instead of diamond (sp^3), resulting in the coating quality and hardness being reduced, as shown in Figure 2.3.

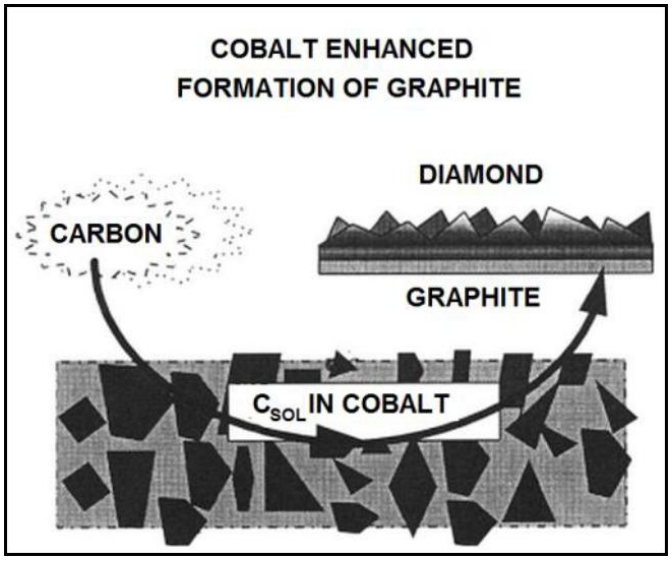

Figure 2.3 Cobalt reaction with carbon (Polini et al., 2006).

The most effective and widely used pre-treatment approach to remove cobalt from the substrate surface is to use chemical solution Deuerler et al. (1996), Haubner & Kalss (2010), and Polini et al. (2006). However, as mentioned, cobalt binds with tungsten carbide. This means that it helps increase mechanical properties of the substrate like toughness of the substrate surface. Its removal could induce the substrate to become porous and brittle. Thickness of the cobalt-etched zone remains important because even though cobalt adversely reacts with carbon, porosity in the substrate also results in reduced layer adhesion between the diamond film and the substrate (Haubner

& Kalss, 2010). Therefore, controlling the thickness of the cobalt-etched zone is crucial, as porosity also leads to reduced adhesion between the diamond film and the substrate.

The most common etching agents are aqueous solutions of either strong oxyacid or hydrochloric acid. Together with these etchants, WC-Co substrates are usually placed in ultrasonic bath for several minutes and then rinsed with deionised (DI) water. The etching time which determines the depth of the ‘‘etched layer’’ can be up to a few micrometres. Lei et al. (2014) carried out the chemical etching process on the tungsten carbide workpiece using two etching agents: etching with Murakami’s reagent (KOH: K_3(Fe (CN)$_6$): H2O = 1:1:10) for two, five and ten minutes, followed by etching with Caro’s acid (30 ml HCl:70 ml H_2O_2) for 10 seconds. The results analysis from Raman spectroscopy and scanning electron microscope (SEM) show that the optimised pre-treatment time for Murakami’s reagent should be more than 5 minutes for effective surface preparation conducive to subsequent acid pre-treatments. This is shown in Figure 2.4.

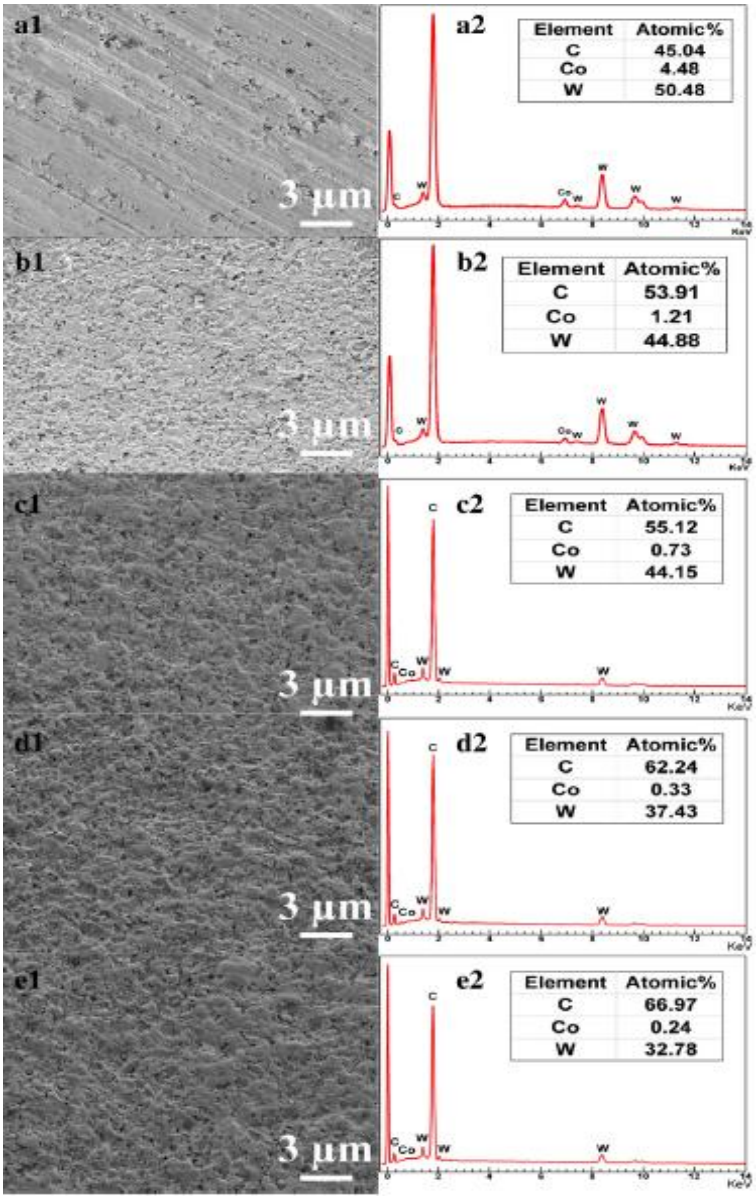

Figure 2.4 Pre-treatment with different etching time (Lei et al., 2014).

The application of Murakami reagent results in the modification of WC grains, leading to increased surface roughness and contact area of the substrate. This enhancement in surface texture significantly improves the mechanical interlocking properties of the diamond coating layer, as detailed by Zhang et al. (2019). Following this, Caro acid subsequently oxidises the binding cobalt, reducing the cobalt composition in the substrate.

However, controlling the reaction with Caro's acid poses challenges. The process is highly sensitive to etching duration and substrate size. Micro drills, for instance, often have small diameters, rendering their flexural stiffness particularly vulnerable to the acidic reagent, as noted by Lei et al. (2014). Consequently, the pre-treatment process must be optimised in order to guarantee not just the adhesion between diamond films and substrates, but also to take into consideration the thickness and flexural stiffness of the substrates.

In summary, the first step in preparing tungsten carbide cutting tools for diamond coating is to remove cobalt from the surface, to prevent formation of graphite films in place of diamond films. Cobalt etching is the pre-treatment type most processed in the cutting tool coating industry.

2.2.2 Interlayer coating

In an HFCVD diamond coating process, a mixture of gas is inherently required to deposit the diamond film onto a substrate's surface. In this context, an interlayer coating is employed as a strategic buffer layer, primarily to prevent the catalytic interaction between cobalt present in substrates and the carbon molecules in the gas mixture. This intervention is crucial in ensuring the formation of diamond rather than graphite.

Numerous scholars have proposed incorporating a buffer interlayer through the deposition of a thin transition layer (e.g., nitrides and carbides) on substrates as barriers to stop the diffusion and catalytic effect of the cobalt. The interlayer technique is normally processed using Physical Vapour Deposition (PVD) which can deposit various types of interlayer coating films before depositing the diamond film layer, e.g., Chromium-based (Chou et al., 2008; Hojman et al., 2013; Lu et al., 2013; Polini et al., 2010), Titanium-based (Contreras et al., 2000; Polini et al., 2006; Raghuveer et al.,

2002), Aluminium-based (Gaydaychuk et al., 2019; Li et al., 2019; Ye et al., 2016) and silicon-based (Cabral et al., 2008; Yuan et al., 2020).

Diamond films could adhere better to substrates with chromium carbide interlayer films than ones without interlayer coating (Chou et al., 2008; Polini et al., 2006). Polini et al. (2006) applied the PVD “arc” technique to create interlayer films on substrates. The reason to use the arc technique is it would produce droplet on the substrate surface during deposition, thus increasing the surface roughness of the substrate more than other PVD coating techniques generating interlayer. Six different samples were coated by the PVD arc technique, followed by being diamond coated for three hours, as shown in Figure 2.5. The two types of samples went through dry sliding wear tests for 30 minutes and three-dimensional (3D) optical profilers were used to analyse the wear caused by the tests, as shown in Figure 2.6. The result shows that the buffer layer Chromium Nitride (CrN) PVD film improves the diamond film properties.

Additionally, Chou et al. (2008) also investigated an experiment using Chromium based interlayer to analyse tribological and mechanical properties of cemented tungsten carbide substrates with 6% cobalt content. For chromisation, one of the chromium-based interlayer samples was placed in a double steel can with the temperature of 950℃ for 4 hours. Adhesion properties of diamond-coated WC-Co specimens were evaluated by Daimler-Benz Rockwell-C Adhesion Tests (HRC-DB). Microstructures of indentation craters on the PVD-coated substrates after the tests are shown in Figure 2.7. It was found that indentation occurred around the crater of the cemented tungsten carbide substrate without interlayer. Meanwhile, indentation on the interlayer chromium carbide substrate occurs only partially on the exposed surface. In addition, the sliding tests carried out detected no measurable wear volume. Thick diamond films deposited onto interlayer chromium-based substrates shows excellent

wear resistance behaviours. Therefore, the introduction of an interlayer enhances the adhesion between the diamond coating and the underlying substrate surface.

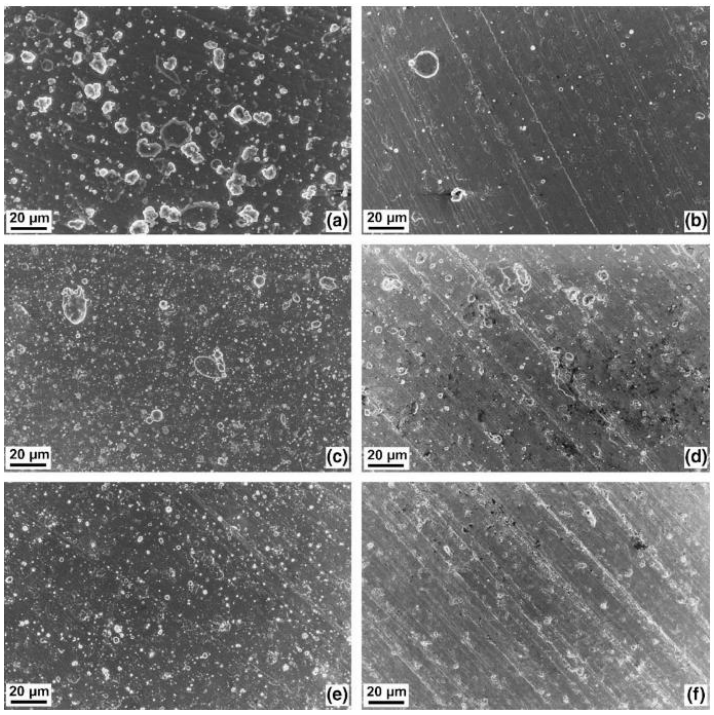

Figure 2.5 Six different PVD arc coating samples (Polini et al., 2006).

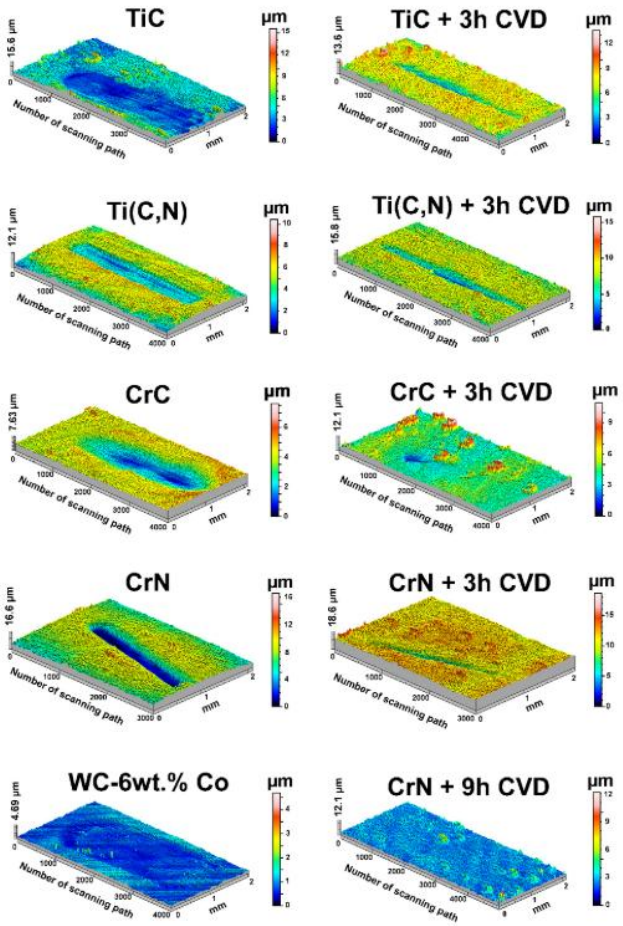

Figure 2.6 Wear analyse by using optical profilers (Polini et al., 2006).

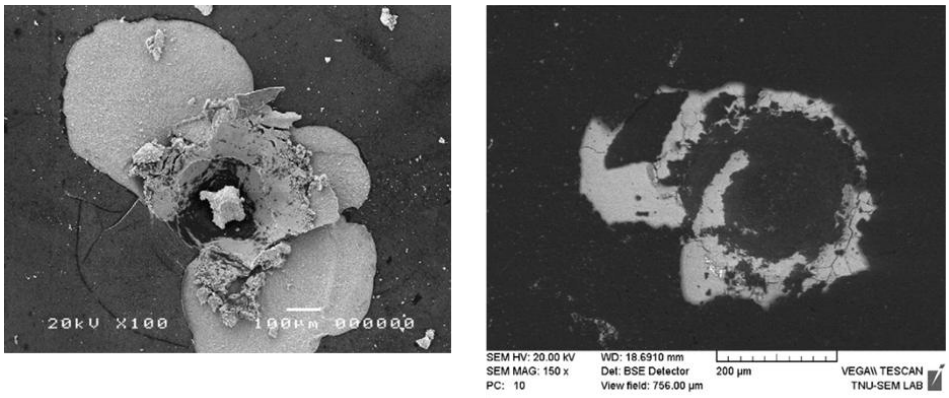

Figure 2.7 Indentation without and with CrN interlayer (Chou et al., 2008).

2.2.3 Surface quality

The importance of rough and corrugated surfaces in tungsten carbide substrates, particularly those with a high defect density, is well-recognized in the context of Chemical Vapor Deposition (CVD). As noted by Zhang & Zhou (1997) and Shen et al.

(2017), these surface properties contribute significantly to an increase in adhesive strength through mechanical interlocking and enhance the nucleation density during the CVD process. In preparation for this, mechanical treatments like peening and sandblasting are employed to intentionally scratch or mar the substrate surfaces. Such pre-treatments have been observed to effectively reduce the depth of the brittle Co-depleted layer, consequently improving the surface toughness of the substrate.

Shen et al. (2017) also carried out Rockwell indentation tests on substrates that underwent pre-treatment to verify the increase in coating film's adhesion strength. For comparative analysis, similar tests were also performed on samples that had not undergone sandblasting. The results showed a significant difference in response to a load of 1000 N: the indentation diameter was 599 μm for non-pre-treated substrates and significantly smaller at 305 μm for pre-treated ones, as depicted in Figure 2.8. Notably, the indentation regions on the sandblasted substrates were circular with minimal film delamination around the indented area. These findings suggest that the adhesion of diamond films is markedly better on substrates that have been both sandblasted and acid-etched compared to those that have not undergone such pre-treatment. This evidence underscores the efficacy of increasing surface roughness through mechanical treatments as a means to enhance the adhesive bond between diamond films and tungsten carbide substrates. By optimizing the substrate surface properties, the overall quality and performance of the CVD-coated tools are significantly improved.

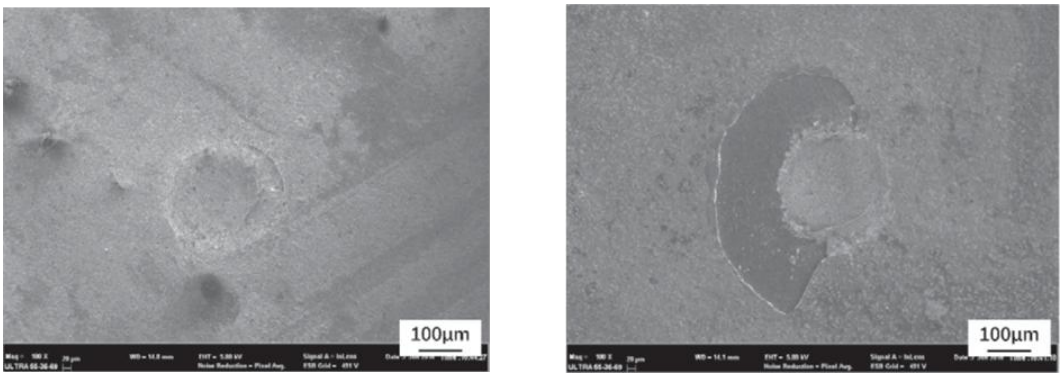

Figure 2.8 Sandblasting and no sandblasting sample (Shen et al., 2017).

2.3 HFCVD coating process

The HFCVD process for diamond coating is an advanced coating technique in which hydrocarbon gases serve as the carbon source, while heated filaments supply the thermal energy required for diamond film growth. The thermal energy generated by the filaments initiates chemical reactions that result in the nucleation and growth of diamond films on the substrate surface. The quality of these films is influenced by several factors, including pre-treatment methods, temperature, gas source, pressure, bias installation, and magnetic field intensity.

The diamond coating process using HFCVD requires a hot filament to react with the input gas carbon source methane (CH_4). Tantalum (Ta) and Tungsten (W) are commonly used as filament materials in HFCVD due to the thermal stability and mechanical integrity exhibited by tantalum and tungsten. At the beginning of the deposition process, the carbon source (CH_4) and hydrogen (H_2) would pass through the hot filament as shown in Figure 2.9. The interaction between the heated tungsten filament and the reactive gas mixture (CH_4 and H_2) results in carbon accumulation on the filament surface, causing structural embrittlement.

Figure 2.10 shows the tungsten filament carbonisation, set at the pressure of 3,000 Pa, being heated up to 1500$C°$. Flowing the mixed gas into the chamber, it was

discovered that increasing the voltage steadily would increase electricity resistivity of the filament (Kromka et al., 2013). During the carbonisation process, the tungsten would react with carbon and form tungsten carbide (WC). After a certain point of the power input, the electricity resistance of tungsten filaments no longer increases, and the carbonisation process stops. It is important to prepare the filaments by carrying out the carbonisation process before commencing the diamond coating process, because the filaments' electricity resistivity can be fluctuating, and this would result in the substrate not being uniformly coated by the diamond film.

After passing through the heated filament, the gas mixture absorbs sufficient thermal energy to dissociate hydrogen containing molecules (H_2, CH_4) into formation of hydrogen molecules (H^0, H_2) as shown in Eq. 1, and this dissociation into atomic forms makes diamond growth possible. The atomic hydrogen (H^0) can further interact with small hydrocarbon molecules (mostly CH_4) to form methyl radicals (CH_3), following Eq. 2. As schematically described in Figure 2.9, the chemical equations are as follows (Asmussen & Reinhard, 2002):

$$H_2 \quad \leftrightarrow \quad H^0 + H^0 \tag{1}$$

$$CH_4 + H^0 \quad \rightarrow \quad CH_3 + H_2 \tag{2}$$

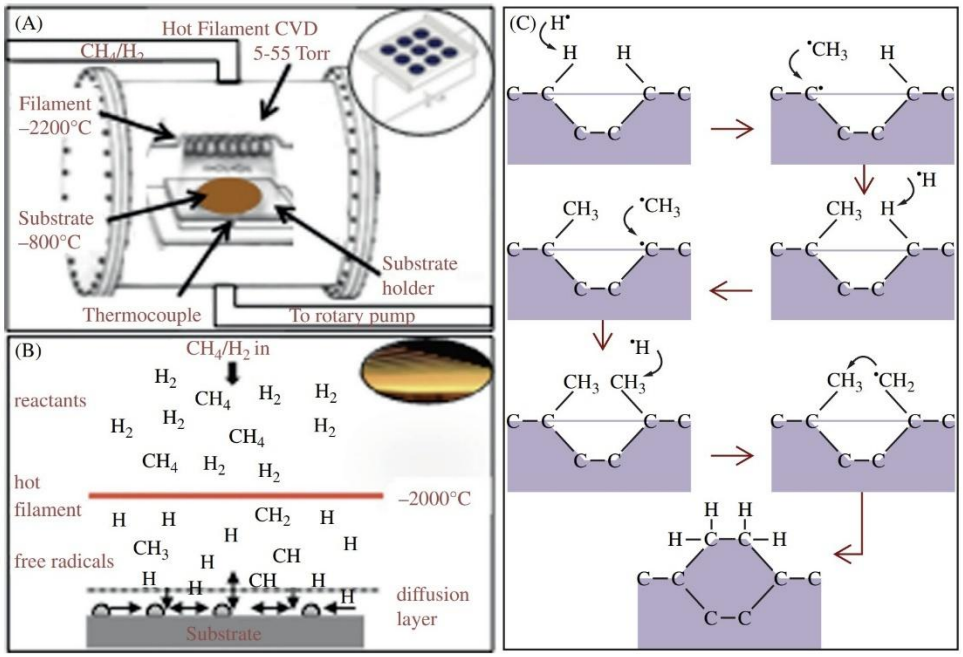

Figure 2.9 HFCVD mechanism (Chandran, 2018).

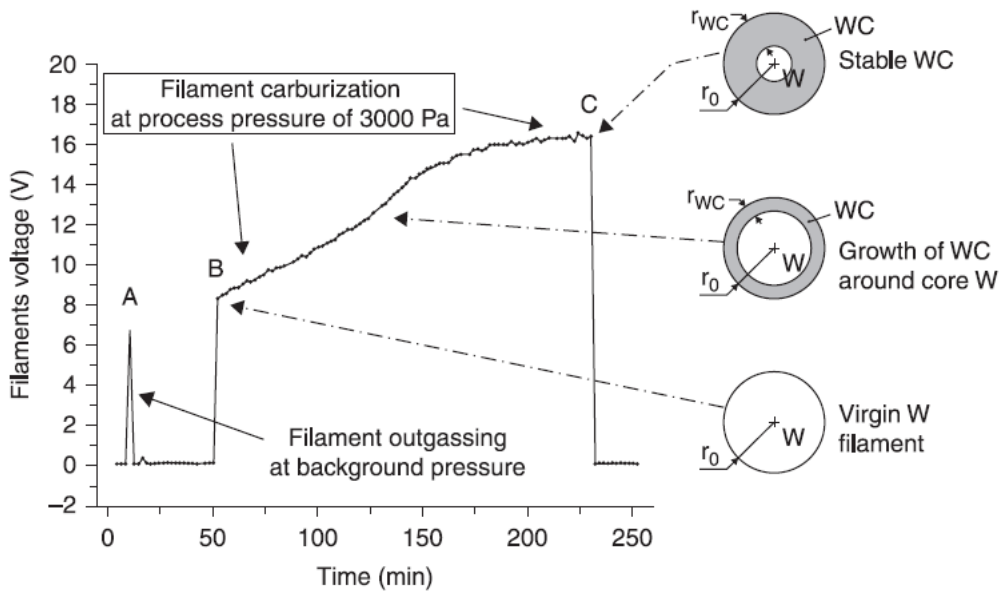

Figure 2.10 Filament carburization during diamond coating process (Kromka et al., 2013).

There are numerous techniques to enhance nucleation and growth of the diamond film. These include increasing methane content in the gas mixture, raising chamber pressure, seeding substrate surfaces with not only diamond but also metallic

or ceramic powders, applying bias, and scratching the substrate surface with abrasives to augment surface roughness and mechanical interlocking. Grain size control within the film is achievable by monitoring the gas composition and pressure, as suggested by Das & Singh (2007). The bias application method is particularly noted for its ease of control and minimal damage to the substrate surface during treatment, as detailed by Liu & Dandy (1995).

2.3.1 Methane concentration in gas mixture

Yan et al. (2019) conducted experiments using HFCVD to coat several cemented tungsten carbide tools using gas source with different methane concentrations of 1%, 3% and 5%, as shown in Table 2.2. The reason of experimenting on varying deposition time (between 6 and 10.5 hours) on each tool sample is to obtain the same coating layer thickness on all series of tools with different mixed gas concentrations and different rates of coating film grain growth. The methane concentration does not only influence the coating surface morphology (Taher et al., 1996) but also the adhesion strength of the diamond coating and the mechanical properties of the tooling. For surface morphology, Figure 2.11 shows that the lower the methane concentration, the larger the grains of the coating film. Larger coating grain translates to stronger mechanical properties of the coating film and larger contact area between the coating and the substrate. A strong mechanical anchoring is formed at the interface between the diamond coating and the tungsten carbide substrate.

Table 2.2 Deposition details of diamond coatings by HFCVD (Yan et al., 2019).

Sample number	CH_4 concentration	Deposition time (h)	Gas flow (Sccm)	
			CH_4	H_2
1	1%	10.5	8	800
2	3%	7.5	24	800
3	5%	6	40	800
4	1%/5%	8	8/40	800

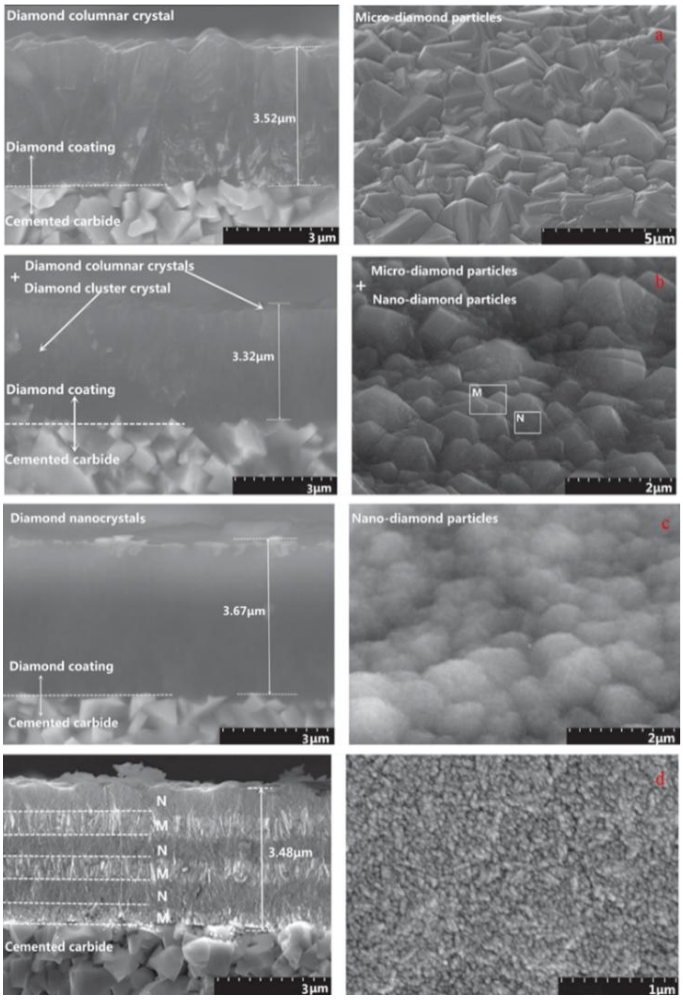

Figure 2.11 Gas Source with different Methane Concentration (a) 1% (b) 3% (c) 5% (d) 1 and 5% (Yan et al., 2019).

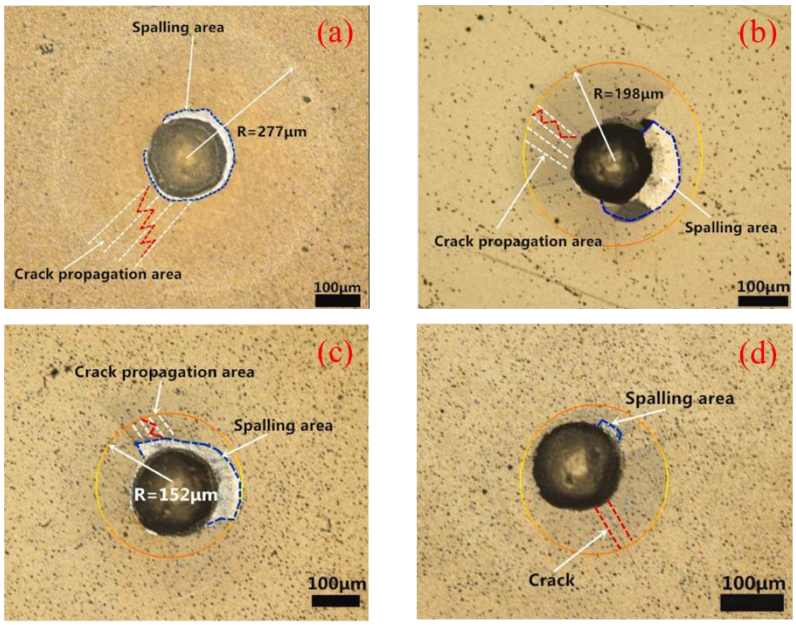

Figure 2.12 Rockwell indentation test results for HFCVD diamond coatings at varying CH_4 concentration (a) 1% (b) 3% (c) 5% (d) 1 and 5% (Yan et al., 2019).

2.3.2 Addition of precursor gases in gas mixture

Besides methane, argon, and nitrogen, other gases can be added to the mixed gas to enhance diamond film nucleation density. Each gas plays a specific role in the deposition process. Methane (CH_4) is the primary carbon source needed for diamond growth, and its concentration directly influences the growth rate, grain size, and quality of the diamond film. Low methane concentrations favour the growth of microcrystalline diamond (MCD), while higher concentrations encourage the formation of nanocrystalline diamond (NCD). Nitrogen (N_2) enhances nucleation density and improves film adhesion by creating additional nucleation sites, which increases the density of diamond crystals. However, excessive nitrogen can lead to reduced grain size, which may adversely affect the mechanical properties of the film. Argon (Ar) serves as an inert buffer gas that modifies the plasma environment during deposition. By diluting the reactive gases, argon helps reduce grain size and results in a smoother surface morphology, which is advantageous for applications requiring low

surface roughness. The nucleation stage significantly affects the growth stage in terms of grain growth rate, texture, roughness, and mechanical properties (Das & Singh, 2007). By adding these precursor gases into the gas mixture, film layers with smoother surfaces and reduced grain sizes can be generated, leading to NCD films.

In case of the gas mixture consisting of methane and nitrogen ($CH_4/N_2/H_2$), Locher et al. (1994) stated that the mixture with low methane concentrations (e.g., 0.5%) bore only minor influence on the nitrogen. On the other hand, slightly higher methane concentrations (1%-2%) would react rapidly with low concentration of nitrogen, tremendously increasing nucleation density of the film. However, Das & Singh (2007) recalled that while increasing higher concentration of methane in the $CH_4/N_2/H_2$ mixture beneficially improves the nucleation density, this comes at the costs of the grain size and the strength of the coating film being subsequently reduced.

In case of the gas mixture consisting of methane and argon, Marton et al. (2007) stated that gradually increasing the argon flow rate from 0 sccm to 14 sccm in the CH_4/H_2 gas mixture (of 3:300 sccm flow rate) would change the coating film morphology, from the typical MCD films with grain size around 500 nm to the NCD films with grain size around 1-100 nm.

2.3.3 Growth of single crystal films

Thin films of grains are generally grown from the bottom up (Francis et al., 2016). Under suitable growth conditions, low nucleation density would result in high growth rate of the diamond grains, due to less intense competition of grain growth (Das & Singh, 2007). Grains growing normal to the substrate surface have the highest probability of survival while ones growing off normal are more likely to be terminated (Das & Singh, 2007).

In less than ideal conditions, the nucleation rate also affects the grain size and film structure. Although low nucleation density leads to faster growth rate, it promotes heteroepitaxial growth of diamond films. Heteroepitaxy refers to the unmatched crystalline structures of the growing film layers (Francis et al., 2016).

In other words, lower nucleation density with higher growth rate of grain results in discrete large diamond crystals. Higher nucleation density with lower growth rate of grain results in rapid growth of multi-oriented nuclei and thus films with more polycrystalline morphologies.

As mentioned, besides addition of nitrogen and argon, the crystal size of the diamond film is mainly dependent on the methane concentration of the gas mixture. This implies that using gas mixture with low methane concentration of about 1% would result in lower nucleation density and hence the growth of MCD films with strong and large diamond grains. On the other hand, using gas mixture with high methane concentration of about 5% would result in higher nucleation density and hence NCD films with finer diamond grains.

Diamond films with smaller grain sizes exhibit reduced stiffness and hardness compared to those with larger crystallites. MCD film layers exhibit higher hardness, higher elastic modulus and superior adhesion characteristics while NCD film layers exhibit lower and more stable friction behaviour, due to presence of non-diamond phases at grain boundaries. MCD-coated tools are suitable for heavy duty works because of larger diamond grain, higher hardness and better film mechanical interlocking. On the other hand, NCD-coated tools process workpieces with smoother surface finishes. By using multilayer coats, workpieces can take advantage from both the MCD and NCD film properties. Recall is that whereas Interlayer is the diamond coating pre-treatment technique of generating metallic film layers to prevent graphite

formation and promote diamond film deposition, the multilayer diamond coating technique is aimed at improving properties of the diamond film.

Yan et al. (2019) further conducted Rockwell Indentation Test for examining adhesion properties by applying the load of 588 N onto the surface of the diamond coated cemented tungsten carbide substrate. Three different types of deformation can be observed: radial cracks, plastic deformation and spalling. It was proven that the substrate in which the multilayer strategy was applied exhibited the best adhesion properties, with relatively minimised coating delamination and cracking, as shown in Figure 2.12. Displayed in Figure 2.13, the first coating layer onto the substrate is the MCD layer, followed by the NCD layer as the surface coating layer. The MCD coating film has larger grains and is more advanced in adhesion strength while the NCD coating film exhibits higher nucleation density which leads to better ability to prevent internal crack propagation (Takeuchi et al., 2001).

Dumpala et al. (2015) used the multilayer coating technique to manufacture difficult-to-machine materials. Aluminium silicon carbide (Al-SiC) metal matrix composites (MMCs) and carbon fibre reinforced plastics (CFRPs) are widely utilized engineering materials in the aerospace and automotive industries owing to their high strength to weight ratios. These materials are classified as difficult-to-machine due to the presence of hard and abrasive reinforcing particles and fibres. Therefore, coating films are required to increase high wear resistance, reduce friction during machining and increasing quality of the surface finishing. Figure 2.13 shows comparison between the five machine inserts differently coated, used as substrates. One was uncoated, one TiN-coated by PVD, one diamond-coated with MCD layer, one diamond-coated with both MCD and NCD layers and one diamond-coated with slow transition from MCD layer to NCD layer. The experiment used the inserts in a turning machine in dry cutting

condition (without lubricants) to cut Al-SiC MMC of the diameter size of $100x300\ mm$. In Figure 2.14, flanks and noses of the inserts were measured before machining, to determine which coating type was suitable for processing the difficult-to-machine workpiece. The quality of the inserts is considered to be failed if either the maximum flank wear or of the maximum nose wear reaches 0.3 mm.

Figure 2.15 and Figure 2.16 display experimental results of utilising insert tools with different coatings. It was found that tools uncoated and PVD-coated by TiN were the worst performers, commencing to wear after less than 1 minute of machining time. Insert tools MCD coated and multilayer coated with MCD-NCD transition layer were the best performers, respectively wearing after 13.5 and 14.7 minutes of use.

Poor performance of the multilayer-coated tool with no MCD-NCD transition time could be due to sharp interface between the two layers (Figure 2.13). Long machining time for tools multilayer-coated with the MCD-NCD transition layer is due to its integration of the smooth dual-layer architecture.

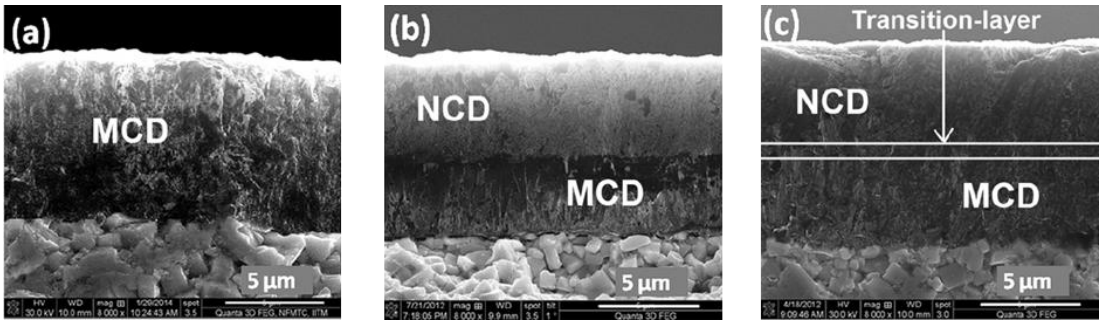

Figure 2.13 (a) MCD multilayer (b) multilayer (c) multilayer with transition layer (Dumpala et al., 2015).

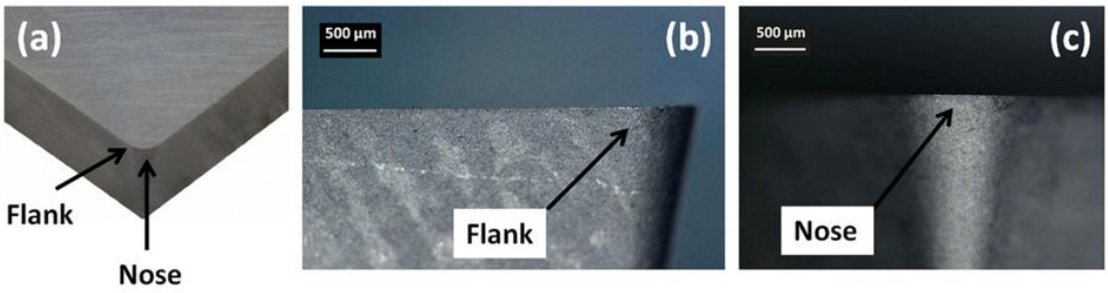

Figure 2.14 Flank and nose (a) MCD multilayer (b) multilayer (c) multilayer with transition layer (Dumpala et al., 2015).

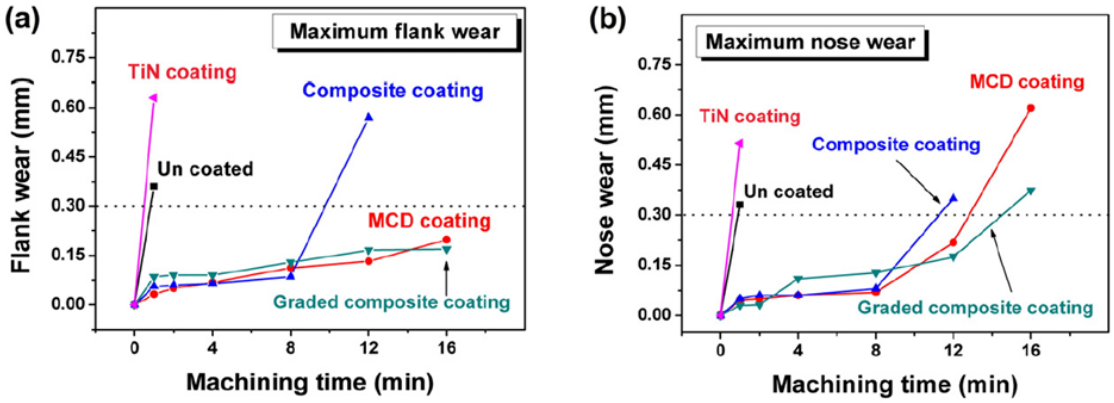

Figure 2.15 Insert flank and nose for different coatings (Dumpala et al., 2015).

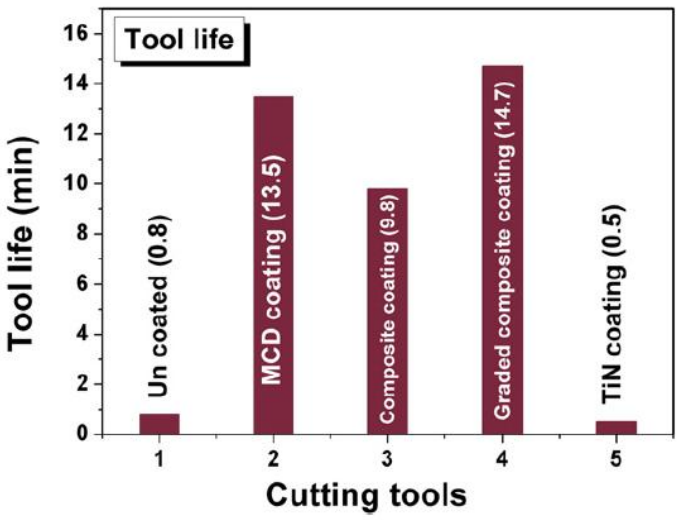

Figure 2.16 Machining time for different coatings (Dumpala et al., 2015).

2.3.4 Chamber pressure

The chamber pressure also affects the diamond film grain size and growth rate. Liang et al. (2007) investigated the effect of different pressure levels in the HFCVD chamber with fixed temperature and the gas mixture of 1% CH_4 concentration in H_2. Figure 2.17 presents SEM images illustrating the surface morphology of the deposited diamond films. It was found that an increase in chamber pressure resulted in a corresponding increase in the diamond film's grain size. The grain growth rate was however highest when the chamber pressure was 2.8 kPa (Figure 2.18).

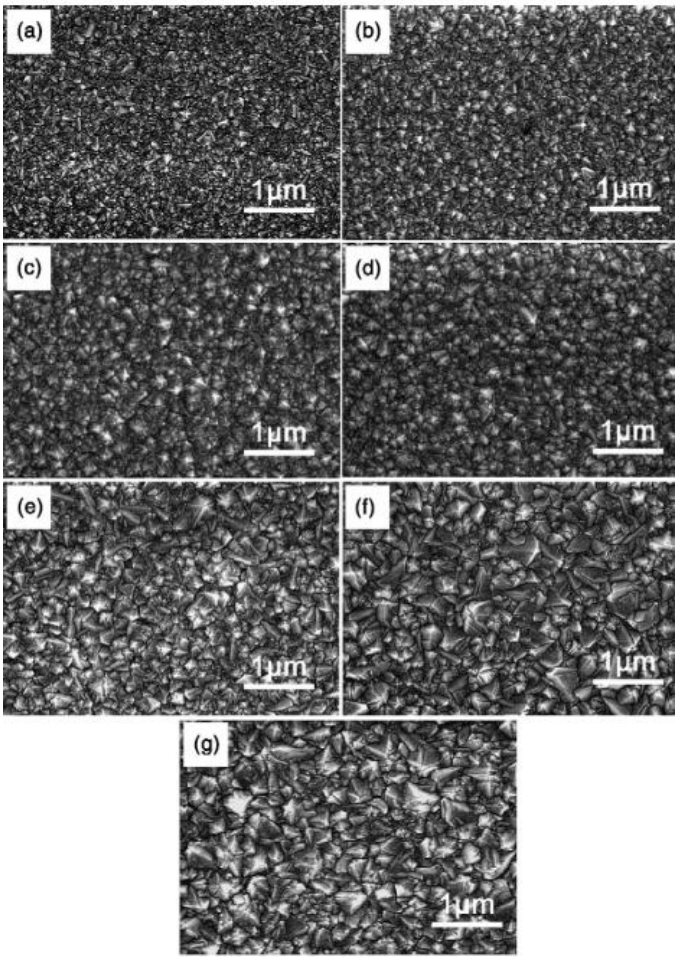

Figure 2.17 SEM images of the films deposited at 850 °C with 1% CH_4 concentration under various pressures: (a) 0.125 kPa, (b) 0.25 kPa, (c) 0.5 kPa, (d) 1.0 kPa, (e) 2.8 kPa, (f) 4.0 kPa, (g) 5.0 kPa (Liang et al., 2007).

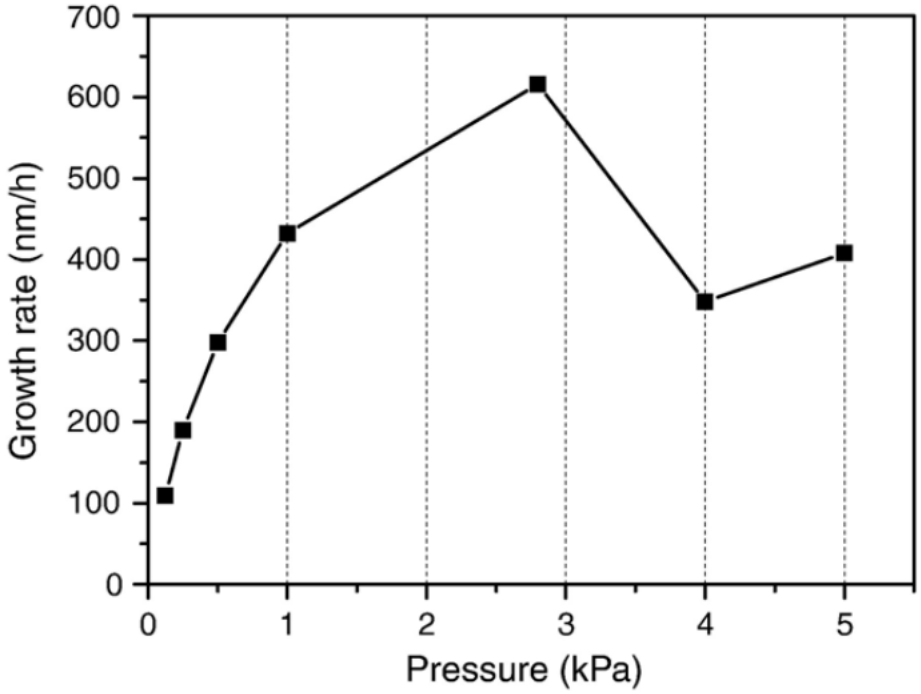

Figure 2.18 Growth rate in various pressure levels (Liang et al., 2007).

2.3.5 Bias system

Bias in HFCVD refers to an applied electrical potential difference between substrate holder and filament or an auxiliary electrode. Positive substrate bias promotes electron bombardment and can increase nucleation density and modify surface morphology. Installing bias system in the HFCVD machine is one of the methodologies used to enhance nucleation, affecting grain growth rate and surface morphology. When the bias system is turned on, positive voltage to the substrate platen and negative voltage to the filament caused electrons bombard onto the surface of the substrate and the growing film. Hence, the diamond film surface is altered.

Cui & Fang (1996) studied on surface morphology of the coating film when applying positive bias and when not using bias. Figure 2.19 compares the surface morphology of diamond films deposited for 2 hours, with 200 V bias applied and without bias applied. From the SEM images, it is clear that the film surface grown on

the substrate is much smoother when the positive bias is applied. However, in Figure 2.20, the Raman spectra shows that the film obtained under positive bias has a weaker and broader Raman diamond first-order line than that obtained without bias. This may be due to the difference in the size of the diamond crystallites, as indicated in Figure 2.19. In addition, they found that nucleation density dramatically increased after 120 V of positive bias voltage was applied, as shown in Figure 2.21.

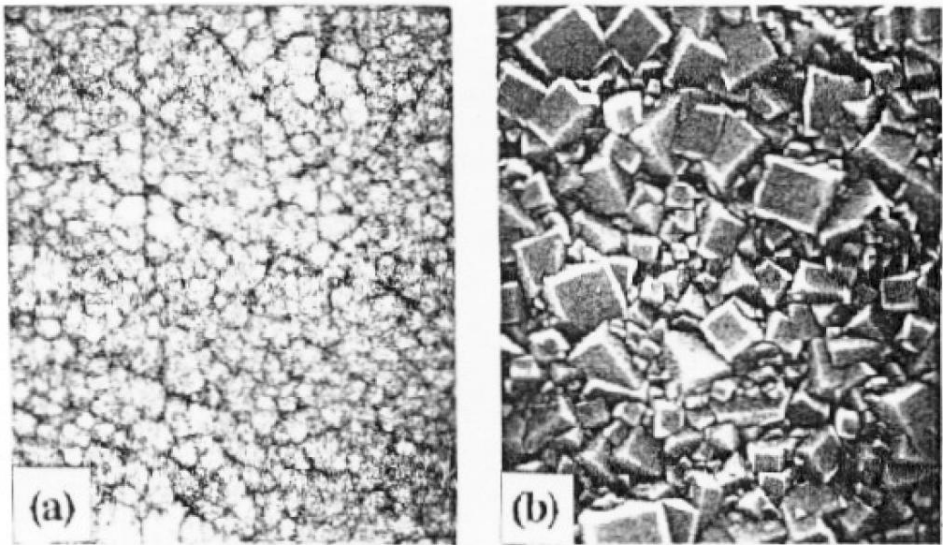

Figure 2.19 a) With bias applied. b) Without bias applied. (Cui & Fang, 1996).

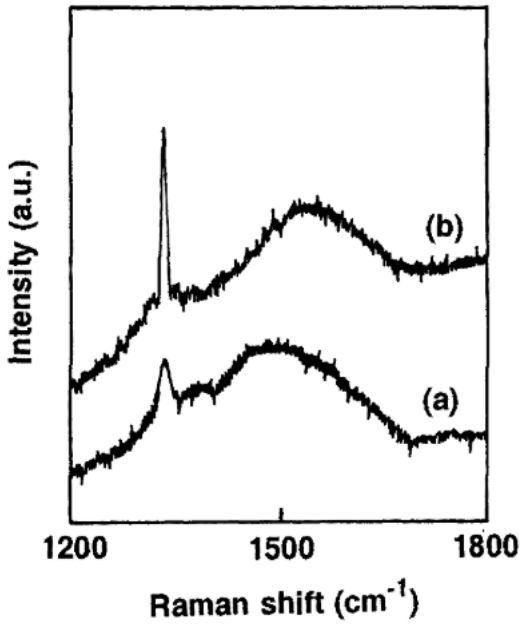

Figure 2.20 (a) Raman with bias applied (b) Without bias applied (Cui & Fang, 1996).

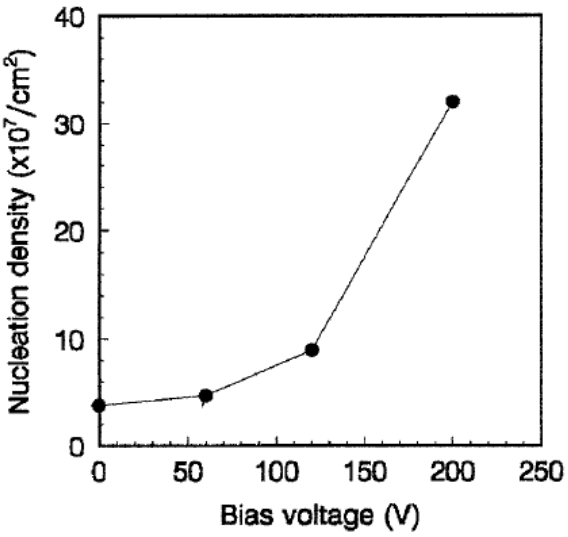

Figure 2.21 Nucleation density with bias (Cui & Fang, 1996).

One of the notable studies of the HFCVD system with applied negative bias has been that of Chattopadhyay et al. (2008). Figure 2.22 captures the surface morphology with pressure under 10 T. Increase in negative DC bias voltage to 1500V leads to increase in coating uniformity and gradual decrease in crystal size. Additionally, surface roughness of the diamond coating decreases following increase in the negative bias voltage, at the constant pressure of 10 T, as shown in Figure 2.23.

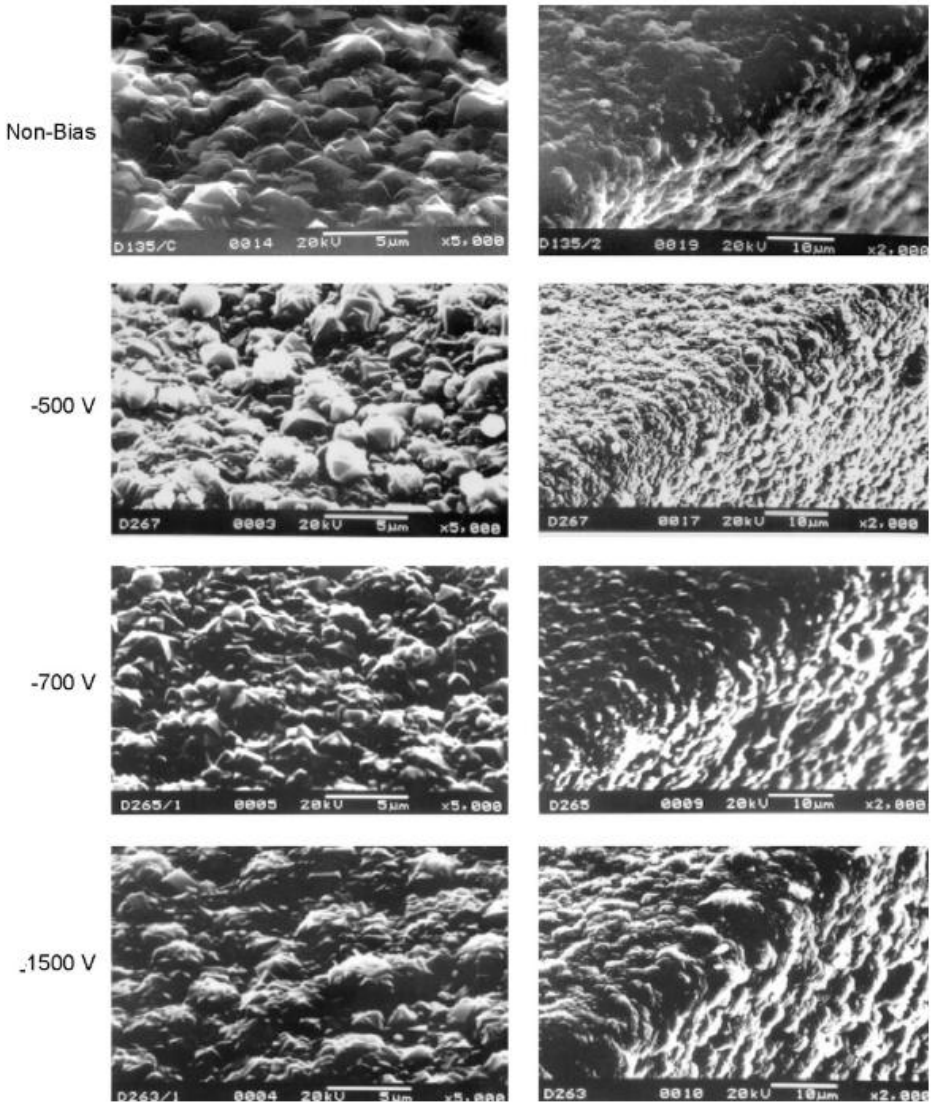

Figure 2.22 Surface morphology under 10 Torr with different bias (Chattopadhyay et al., 2008).

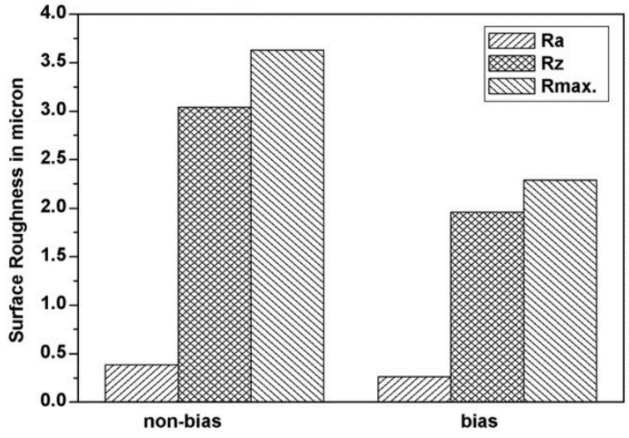

Figure 2.23 Roughness measurement. (Chattopadhyay et al., 2008).

2.4 Magnetic field assisted HFCVD

The integration of magnetic fields into Hot-Filament Chemical Vapor Deposition (HFCVD) systems has emerged as an essential method for enhancing diamond film deposition. The ability to manipulate magnetic fields within the deposition chamber allows for improved control over the growth rate, crystal nucleation and crystal morphology of deposited films (J. Li et al., 2017; Long et al., 2015; Wang et al., 2018). There are three primary magnetic field configurations commonly used in HFCVD: Static Magnetic Field (MF), Periodic Magnetic Field (PMF), and Magnetic and Electric Fields Coupling (MEFC). Each configuration offers unique advantages, allowing for tailored control of the deposition process, which in turn enhances the film properties and broadens potential applications.

Table 2.3 provides an overview of the parameters associated with each of these magnetic field systems.

Table 2.3 Comparative configurations of various magnetic field systems employed in the HFCVD process.

Magnetic Field Enhancement in HFCVD	Static Magnetic Field (MF)	Periodic Magnetic Field (PMF)	Magnetic and Electric Fields Coupling (MEFC)
Parameters adjusted for the novel system	1. Distance between magnets 2. Size and location of magnets	1. Field strength (B_0) 2. Angular frequency (ω)	1. Field strength (B_0) 2. Angular frequency (ω) 3. Electric field intensity

2.4.1 Static magnetic field

X. Liu et al., (2023) demonstrated that static magnetic fields contribute to the uniform confinement of plasma, improving film deposition consistency and growth rates. This phenomenon is attributed to the enhanced plasma confinement, which stabilizes the plasma environment and increases the interaction between the reactive species and the substrate.

Little et al. (2005) and Wen et al. (2003) highlighted that static magnetic fields lower the surface energy of diamond, facilitating enhanced nucleation and crystal growth, even under atmospheric pressure conditions. Wen et al. (2003) further showed that at field strengths ranging from 10–20 Tesla, static magnetic fields not only improve the yield of diamond nanoparticles but also enhance the overall film quality. Their study indicated that the presence of a static MF resulted in a 30% increase in diamond film yield (Figure 2.24).

The static magnetic field's primary role is to guide the motion of plasma species, aligning precursor molecules in ways that favour crystallographic alignment and film quality. This results in a more uniform particle distribution and accelerated growth compared to conventional methods. As observed by Wen et al. (2003), a stronger static magnetic field increases plasma density near the substrate, which boosts the nucleation rate, resulting in films with improved characteristics.

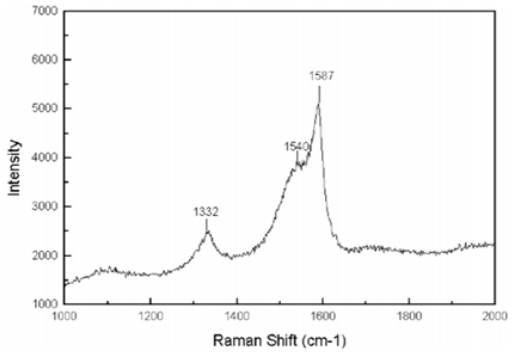

Figure 2.24 Static magnetic field (Wen et al., 2003).

2.4.2 Periodic magnetic field

PMF introduce a dynamic oscillation in the magnetic field, given by $B=B_0\sin(\omega t)$, which plays a critical role in enhancing energy transfer between the plasma species and the substrate, leading to improved deposition efficiency. According to Long et al. (2015) and You et al. (2009) the use of PMF in HFCVD significantly increases the growth rate of nanodiamond films, demonstrated that the implementation of HFCVD system with PMF increases the growth rate of diamond films compare to the conventional HFCVD system.

The primary advantage of PMF over static magnetic fields is its dynamic nature, which improves the interaction of reactive species, such as carbon ions and radicals, with the substrate. This leads to a higher deposition rate and better film morphology. You et al. (2009) also reported that films grown with PMF exhibited a much higher ID/IG ratio in Raman spectra, indicating a higher quality of diamond-like material compared to films grown without PMF. These findings demonstrate that PMF not only accelerates the growth rate but also improves the quality of the films by increasing the proportion of sp^3-bonded carbon, a key characteristic of diamond films.

In addition to these improvements, You et al. (2009) also noted that the application of PMF influenced the crystallographic orientation of the deposited films. Their study revealed that films grown under the influence of PMF showed a preference for the (111) orientation, which is typically associated with lower friction properties and is desirable for tribological applications. In comparison to films grown under conventional HFCVD conditions, where the orientation is less controlled, the films grown with PMF exhibited improved orientation towards specific crystallographic planes. This is particularly significant because the orientation of diamond films can dramatically impact their mechanical, thermal, and electronic properties. For example,

the (100) orientation of diamond films is known for its superior thermal conductivity, making it suitable for electronic applications, whereas the (111) orientation is more favourable for tribological applications due to its low friction characteristics.

The improved crystallographic orientation observed under PMF conditions is likely the result of the oscillatory magnetic field, which promotes a more directed alignment of the carbon species as they are deposited onto the substrate. This dynamic alignment helps to stabilize the formation of the diamond lattice in specific orientations, thereby improving both the structural and functional properties of the films. The ability to control orientation provides a significant advantage in applications requiring specific film characteristics, such as cutting tools, electronics, and coatings.

Long et al. (2015) investigated the effects of PMF with field strengths ranging from 32 to 106 Gauss and angular frequencies (ω) between 3,000 and 45,000 rpm. The study demonstrated that higher angular frequencies (ω) were particularly beneficial for promoting nanodiamond film growth and observed that increasing the angular frequency facilitated better motion and increased collision rates of charged particles within the plasma, improving energy transfer and making the deposition process more efficient. Consequently, films produced at higher angular frequencies exhibited better uniformity, surface morphology, and faster growth rates. Furthermore, films produced under PMF conditions exhibited superior field emission properties, with the turn-on electric field of 2.9 V/μm and current densities of 32.7 μA/cm² at an applied field of 6.5 V/μm, demonstrating that PMF significantly improves the electron field emission efficiency of diamond films.

The use of PMF for diamond film growth has proven to be particularly advantageous in enhancing the field emission properties of films. The enhanced plasma density and improved crystallinity contribute to better electrical conductivity and field

emission performance, which is essential for applications in field-emission displays (FEDs), vacuum electronics, and other devices that require high-performance diamond-based materials.

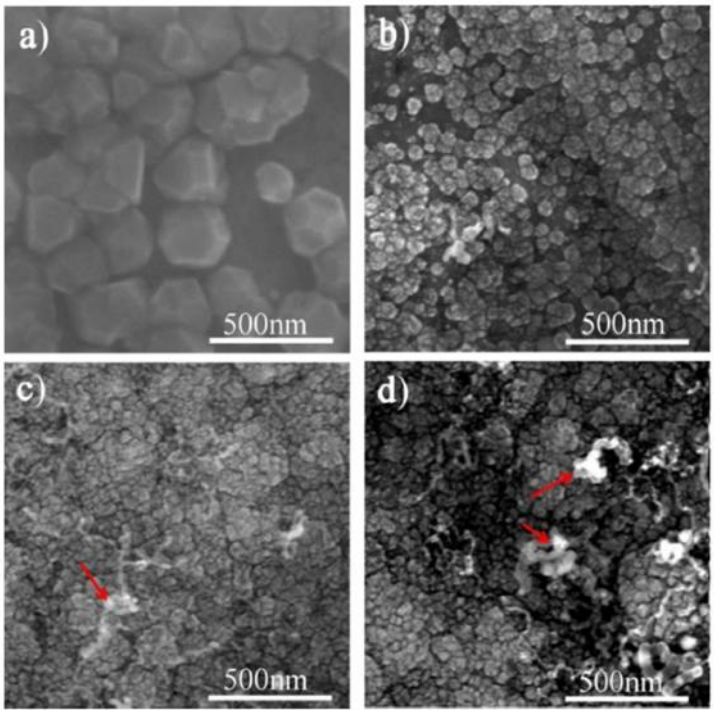

Figure 2.25 SEM images of diamond film produced by HFCVD with periodic magnetic field (a) no PMF, (b) 10,000 rpm, (c) 20,000 rpm and (d) 30,000 rpm (Long et al., 2015).

2.4.3 Magnetic and electric field coupling

The coupling of magnetic and electric fields (MEFC) represents a sophisticated approach in field-assisted HFCVD, offering enhanced control over plasma density, energy distribution, and film growth. By combining the advantages of both magnetic and electric fields, this method significantly optimizes the deposition process, improving both the efficiency and quality of carbon films. Li et al. (2017) the effects of this dual-field approach on the deposition of various carbon films in HFCVD systems. Their results suggest that the combined influence of both fields can

substantially optimize the deposition process, resulting in higher plasma densities and improved film characteristics (Figure 2.26 and Figure 2.27).

The magnetic field in MEFC serves to concentrate gas molecules near the substrate surface, thereby increasing the local plasma density. This concentration of reactive species accelerates the nucleation process, enhancing the uniformity and quality of the deposited film. Moreover, the increased plasma density helps to reduce grain size, which is a critical factor in producing films with fine, uniform structures. On the other hand, the electric field plays a crucial role in promoting the ionization of reactive gases, facilitating the conversion of carbon species from the sp^2 phase to the more stable sp^3 phase. This transformation significantly enhances the quality of the film, as sp^3-bonded carbon atoms are characteristic of the desired diamond-like structure.

The coupling of magnetic and electric fields has proven to be highly effective in reducing grain size and improving the uniformity of the films. Li et al. (2017) showed that the simultaneous application of both fields not only increased the deposition rate but also resulted in films with finer grain structures, enhanced morphology, and more consistent thickness. The electric field's ability to ionize reactive gases increases the reactivity of carbon species, accelerating film growth and ensuring more homogeneous deposition. This process helps to produce films with improved surface morphology and overall better quality.

Wang et al. (2018) further explored the role of MEFC in improving the thickness and morphology of carbon films. Their study compared films deposited with and without the assistance of magnetic fields under varying bias currents. The cross-sectional SEM images, shown in Figure 2.27, reveal that films produced with MEFC exhibited finer grain structures and more uniform thickness compared to those deposited without magnetic fields. These results highlight the superior control afforded

by the coupling of both fields, which stabilizes the plasma environment and results in films with improved consistency and quality. In addition to improving film morphology, MEFC systems also enhance field emission properties. The increased ionization of reactive gases and more uniform film deposition contribute to better electrical conductivity and enhanced performance of the resulting films in applications like field-emission displays (FEDs). The application of both magnetic and electric fields thus represents a powerful tool for tailoring the properties of carbon films, providing greater flexibility and efficiency in the fabrication of advanced materials.

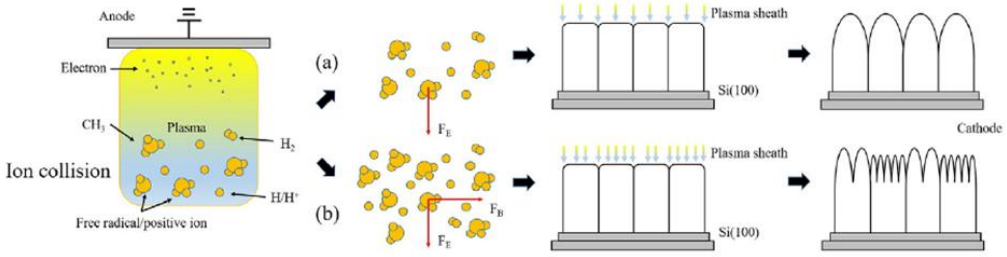

Figure 2.26 Schematic diagram of etching film with plasma.

(a) assisted by electric field (b) assisted by MEFs. (Li et al., 2017).

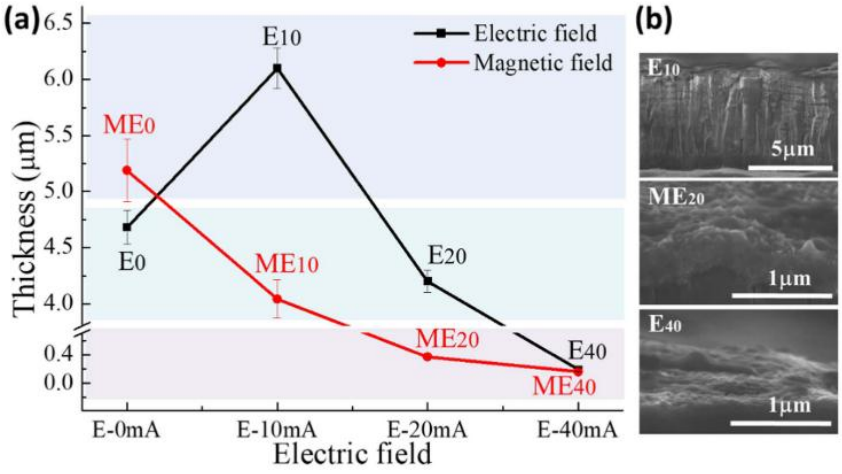

Figure 2.27 (a) The thickness of carbon films deposited without (sample E0-E40) and with magnetic field (sampleME0-ME40) at different bias current (b) The cross-sectional SEM images of sample E10, ME20 and E40 respectively (Wang et al., 2018).

2.5 Difficult-to-cut materials processed by diamond-coated tools

Diamond-coated cutting tools have been widely used for machining non-ferrous materials, such as aluminium-silicon alloys, copper alloys, fibre-coated polymers, green ceramics and graphite (Kanda et al., 1995). Materials with unique metallurgical properties require different types of diamond coating, such as MCD coating, NCD coating and multilayer diamond coating. Diamond coating film comes with the benefits of high strength and toughness, good tribological efficiency and chemical inertness, outstanding wear resistance. Difficult-to-cut workpieces include the following:

2.5.1 5G printed circuit board (PCB)

The adoption of the fifth-generation wireless communication system (5G) comes with the increasing demand for high-frequency and high-speed printed circuit boards (PCB). The 5G technology is applied in satellite communications, automotive radar and other wireless communication equipment to provide higher reliability and lower delay in signal connectivity (Shi et al., 2019).

Unlike previous wireless system generations, the PCB used in the 5G system has a very different layout design, with inclusion of epoxy resin, polyphenylene oxide resin and inorganic filler (Liu et al., 2020), posing new challenging problems of manufacturing the board, decreasing the manufacturing tool life. Printed circuit boards (PCBs) are generally classified into two main categories: high-frequency and high-speed PCBs. Examples of 5G PCB plated details are summarised and illustrated in Table 2.4.

Table 2.4 Characteristics of 5G High-Frequency and High-Speed PCBs.

	High-speed Multilayer PCB	High-frequency Microwave PCB
Number of Layers	Multi-layer structure, generally made by laminating a core board and a semi-cured multi-layer board.	2 layers
Board Thickness	Depending on the number of layers after lamination	0.8mm
Structure	Copper foil, epoxy resin, fiberglass cloth and hard filler (Al_2O_3)	Copper foil, PTFE and ceramics (SiO_2, TiO_2)
Application	High-end servers, autonomous driving and satellite communications	Automotive radar, GPS antenna, patch antenna and other communication equipment in wireless communication

There are several challenges when using the microdrill to process the high-frequency and high-speed 5G PCB. First, due to the increasing proportion of fillers in the 5G PCB, the board has increased wear resistance and is more difficult to be processed by the micro drill. Second, the wear of the micro drill closely affects the quality of the micro-hole and the accuracy of the hole registration. The issue the of microdrill's wear resistance therefore needs to be addressed imminently.

During a typical PCB drilling process, epoxy resin fibreglass cloth chips and glass fibre chips are formed in white powder wood (Chengyong et al., 2016). Under high-temperature drilling condition, the easily molten resin chips adhere with the glass fibre chips, and together they further form mixed chips, known as drilling dirt. The drilling dirt adhered to the spiral groove prevents chip removal, further causing more dirt to be adhered to the hole wall and the drill tip, affecting the next cutting operation

of the drill bit. This results in the tool being worn and fractured before its expected lifespan. It also causes the phenomena of delamination and microcrack on the workpiece PCB.

Zheng et al. (2016) discovered from SEM images that the two main types of microdrill wears were abrasion and adhesion. Figure 2.28 demonstrates that the abrasive wear mainly occurs on the chisel edge and the main cutting edge, affecting service life of the microdrill. Fiberglass and fillers in PCBs are the main causes of abrasive wear on microdrills. Figure 2.29 shows that adhesion wear is caused by adherence of resin mixed chips and wear on the surface of the microdrill's tip and spiral groove, affecting the cutting performance and chip removal of the microdrill. In turn, this increases then temperature in the drilling hole and worsens the microdrill wear.

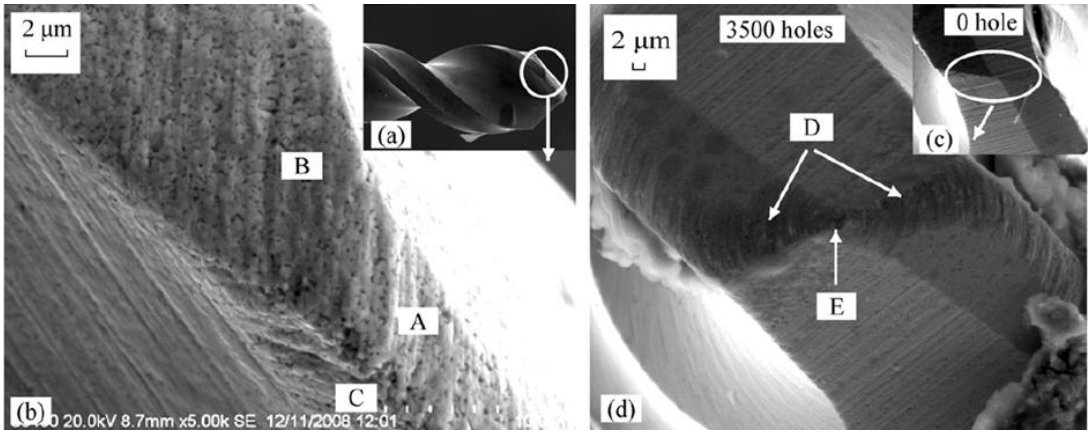

Figure 2.28 Abrasive wear after drilling holes on PCB board (Zheng et al., 2016).

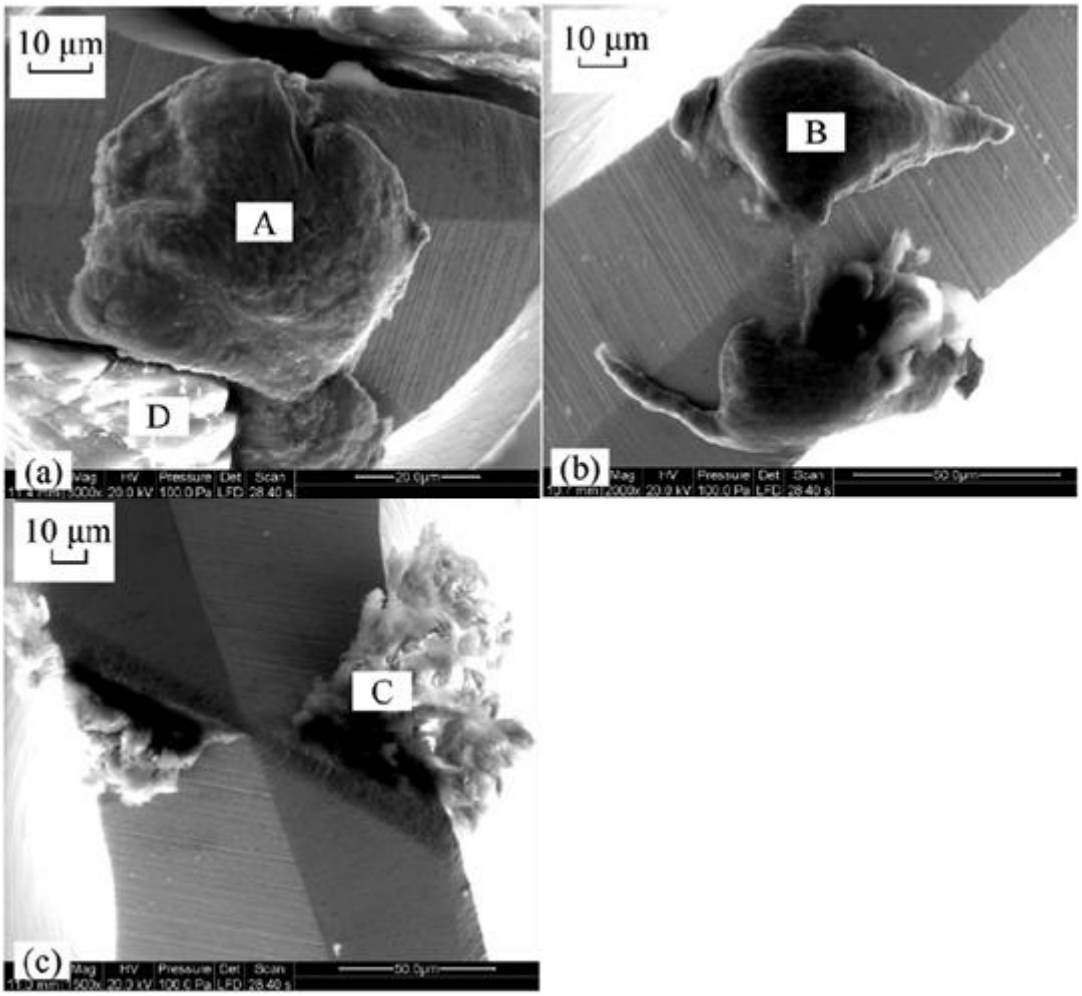

Figure 2.29 Adhesion wear after drilling holes on PCB board (Zheng et al., 2016).

According to Lei et al. (2014), one of the effective ways to machine 5G PCB workpieces is to apply thin diamond coating film onto PCB drilling tools. The NCD coating layer could reduce friction and surface roughness of the drill, making the tool extremely resistant to abrasive wear and thus expanding its operating life as compared to uncoated drills.

In general, the quality of the mechanically drilled holes of PCBs greatly influences subsequent manufacturing processes and properties of the board, such as electroplating factor, welding quality and electronic reliability. Currently, the global trend on developing high density PCBs have made it more difficult to control the

manufacturing and quality of the boards. This is due to high brittleness, anisotropy and poor heat conductance of the material's mechanical properties.

Figure 2.30 depicts quality index evaluation of the main drilled hole on the 5G PCB (Zheng et al., 2011). Quality of the drilled holes on PCB workpieces is an important issue as it influences interconnections, electrical properties and assembly of PCB components.

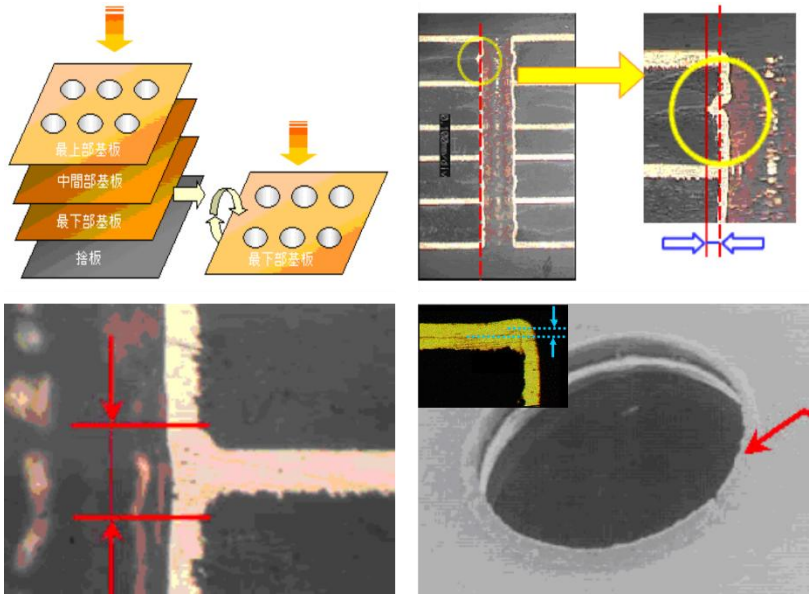

Figure 2.30 PCB quality index (Zheng et al., 2011).

Delamination can occur in composite materials due to insufficient adhesive strength between the copper layers and resin layer of PCB materials. Additionally, when directions of the radial and axial cutting forces are positioned inaccurately during the drilling process, the drilling tools can vibrate sideways away from the drilling axis, excessively removing the material volume.

Delamination can occur in composite materials due to insufficient adhesive strength between the copper layers and resin layer of PCB materials. Additionally, inaccuracies in the positioning of radial and axial cutting forces during the drilling process can cause the drilling tools to vibrate laterally away from the drilling axis,

leading to excessive removal of material. The roughness of the hole wall is influenced by the expansion and retraction of the workpiece material. Since the PCB contains various components with different materials and coefficients of linear expansion, the resin's relatively higher linear expansion compared to other parts can lead to a larger area of material being cut by the drill bit. Consequently, as the resin cools and retracts, the surface roughness may differ across various sections of the wall.

Another factor contributing to the variation in roughness is the effect of high centrifugal forces. Chips that are caught up in these large centrifugal forces, directed radially outward from the drilling axis, may undesirably cut into the softer resin material of the hole wall. When the cutting edge of the drill begins to wear, it can cause the tool to press against the workpiece wall rather than effectively remove material. This action generates excessive heat in the hole during the drilling process, leading to the melting of the resin and copper foil components of the workpiece. These molten materials may adhere to the drill flute, which further decreases the material removal rate. Zheng et al. (2012) suggested that, in order to reduce the probability of unintended connections between two adjacent circuits, the nail head thickness should be kept at a maximum of 1.5 times the copper foil layer thickness.

During the drilling process, the copper foil layer of the PCB heats up and softens, which reduces its ability to withstand the thrusting force from the drill. As a result, burrs are formed at the bottom of the workpiece hole. The hardness of the PCB workpiece can be adjusted to control the shape and size of these induced burrs, thereby improving the quality of the finished hole.

2.5.2 Zirconium dioxide

Zirconium dioxide (ZrO_2), a member of the oxide family of engineering ceramics, is widely recognized for its exceptional mechanical and thermal properties,

making it a material of choice in a range of demanding applications. Engineering ceramics include a diverse array of materials such as oxides, carbides, nitrides, borides, silicates, and glass ceramics, with the most commonly used being aluminium oxide (Al_2O_3), zirconium dioxide (ZrO_2), silicon nitride (Si_3N_4), and silicon carbide (SiC) (Y. Liang & Dutta, 2001). As detailed in Tables 2.5 and 2.6, zirconium dioxide stands out primarily for its remarkable strength, biocompatibility, and high resistance to thermal and chemical degradation (Ferraris et al., 2016).

Table 2.5 Properties of various ceramic materials. (Ferraris et al., 2016).

Material Properties	Al_2O_3	Si_3N_4	ZrO_2	SiC
Density (g/cm^3)	3.8-4.0	3.2	5.0-6.0	3.1
Vickers hardness (kg/mm^2)	1800-2000	1500-1600	1100-1300	2600
Fracture toughness ($MPa^{1/2}$)	3-4	4-8	4-12	3-5
Flexural strength (MPa)	300-500	700-850	500-1800	400-600
Weibull modulus	8-12	18	10	10-18
Young modulus (GPa)	300-400	310	200	400-450
Thermal expansion $10^{-6}K^{-1}$	7-8	3.2	10	4.5-8
Thermal conductivity (W/m K) @RT	25-35	30-40	1.5-2	80-120
Electrical conductivity (S/cm) @ 20° C	$<10^{-14}$	$<10^{-14}$	$<10^{-10}$	0.2-1

Table 2.6 Different types of ceramics applications (Ferraris et al., 2016).

Applications	Performance advantages	Ceramics
Wear parts, seals, bearings, valves, nozzles	High hardness, low friction	SiC, Al_2O_3
Cutting tools	High strength, hardness	Si_3N_4, Al_2O_3
Heat engines: diesel engine components, gas turbines	Thermal insulation, high temperature strength, fuel economy	ZrO_2, SiC, Si_3N_4
Medical implants: hip, shoulder, knee, dental, joints	Biocompatibility, surface bond to tissue, corrosion resistance	Hydroxyapatite, bioactive glass, Al_2O_3, ZrO_2

ZrO_2 is renowned for its high mechanical strength, making it suitable for applications requiring materials that can withstand both mechanical and environmental stresses. One of the most significant advantages of ZrO_2 is its biocompatibility, which minimizes the likelihood of adverse reactions such as allergies or inflammation when used in medical or dental applications. These characteristics have made ZrO_2 an excellent choice for dental restorations, where it is used as an alternative to traditional high-toughness core materials. Its excellent mechanical properties, coupled with its natural, aesthetic appearance, have made it particularly suitable for producing implant superstructures, root dental posts, crowns, and fixed partial dentures.

As a high-temperature oxide ceramic, ZrO_2 offers exceptional thermal stability, with a high melting point and superior thermal insulating properties (Piconi & Maccauro, 1999). Additionally, ZrO_2 exhibits excellent chemical inertness, which contributes to its durability and longevity in harsh environments. This makes it a versatile material for use not only in dental applications but also in industries that require materials capable of withstanding high temperatures and aggressive chemical environments.

While ZrO_2 offers impressive mechanical and chemical properties, its hardness also presents challenges during machining. Traditional tungsten carbide tools, commonly used in machining processes, often lack sufficient hardness and abrasion resistance when used to machine hardened ceramics like zirconium dioxide (Bian et al., 2018). The wear of cutting edges on tungsten carbide tools results in rapid deterioration of the tool shape, reducing efficiency and precision in the machining process. To overcome these limitations, it is necessary to apply coatings such as diamond films to the cutting tools. These coatings significantly enhance the durability and performance of machining tools, enabling them to better handle the hardness of zirconium dioxide.

The application of diamond coatings, particularly through chemical vapor deposition (CVD), has been shown to significantly improve the performance of dental burs used for machining zirconia dental materials. According to Sein et al., (2003), CVD diamond-coated dental burs exhibit a markedly longer lifetime and superior performance compared to their uncoated counterparts. The wear rates of these diamond-coated burs are reduced by a factor of three, significantly improving milling efficiency and reducing the need for frequent tool replacements. Moreover, the hardness and abrasion resistance of diamond coatings allow for more precise and effective machining of zirconia, contributing to better outcomes in dental restorations.

2.6 Quality measurement of diamond coating films

There are two ways to determine the diamond coating quality: by using non-destructive tests or destructive tests. Non-destructive tests mean the measurement would not damage the coating surface, allowing for further use after testing. Meanwhile, destructive tests would damage the coating surface.

2.6.1 Non-destructive tests

The non-destructive tests are used to observe surface morphology. A scanning electron microscope is employed to examine the grain orientation and structural uniformity of the coating film. 3D optical dimensional metrology can be used to evaluate surface roughness of the film. Raman spectroscopy serves as a non-destructive analytical technique for assessing the phase composition and crystalline purity of the diamond film.

Surface morphology of the diamond-coated tools was assessed using SEM. Under the SEM, it can be observed whether the diamond film is MCD or NCD. For MCD layers, the size for each grain is greater than 1 μm and for NCD layers, the size is smaller than 100 nm. It is important to select the appropriate coating films for

different applications as they have different mechanical properties, e.g., roughness and hardness (Dumpala, Chandran, Madhavan, et al., 2015). Stiffness and hardness of the diamond coatings decrease with the reduction in crystal size. MCD layer exhibits high hardness, high elastic modulus and superior adhesion characteristics and NCD coatings exhibit low hardness and high toughness due to the presence of non-diamond phases at the grain boundaries.

The 3D optical surface profiler can be used to determine the surface roughness of the tool after the diamond coating process. Moreover, after machining the workpiece, an 3D optical profiler can also be used to determine the surface roughness of the workpieces. Examples of different diamond coating films obtained from the 3D optical surface profiler are shown below in Figure 2.31 and Figure 2.32.

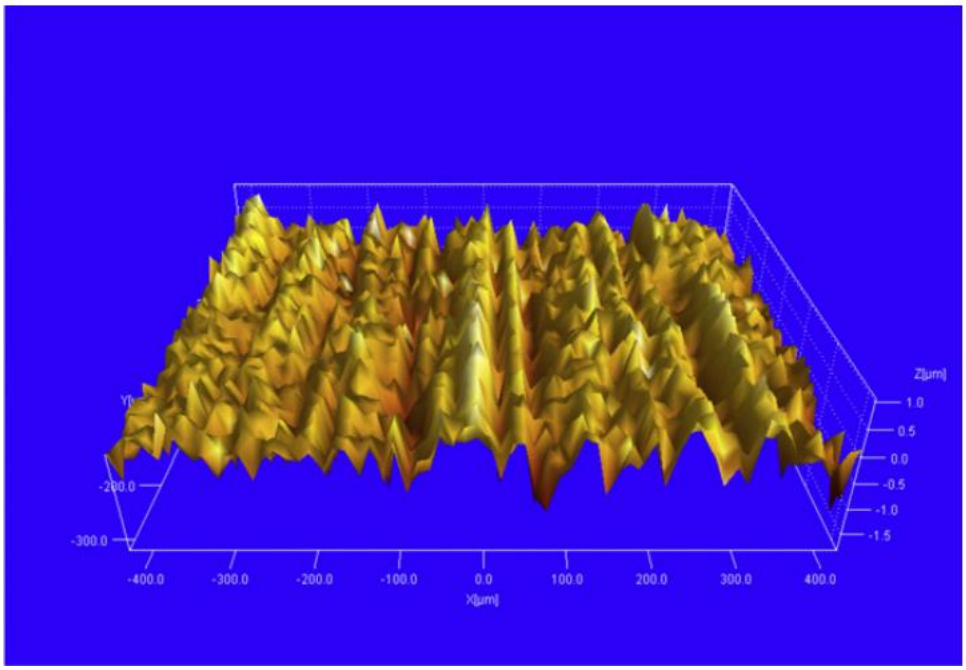

Figure 2.31 Microcrystalline diamond coating (Chen et al., 2013).

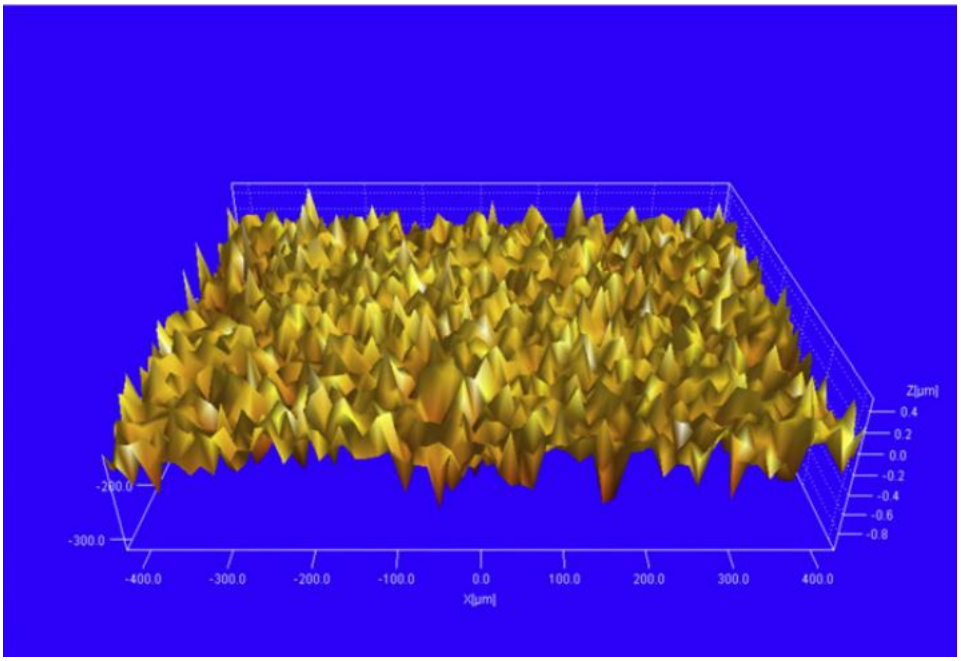

Figure 2.32 Submicrometric diamond coating (Chen et al., 2013).

For the Raman spectroscopy, the wavelength of the monochromatic laser reflecting from diamond coated surface and collected by the detector should be around 1330-1340 cm^{-1} (D-peak) and around 1540-1570 cm^{-1} (G-peak). As shown in Figure 2.33. the D/G ratio serves as a key parameter for evaluating the sp^3/sp^2 carbon bonding ratio, prov iding insight into the structural quality of the diamond film. If the D-peak is higher than the G-peak, it means that there are more sp^3 bonds than there are sp^2 bonds. In addition, Full Width at Half Maximum (FWHM) is another variable used to measure purity of diamond films deposited (Figure 2.34). The higher the D/G ratio, the lower the FWHM figure, and the purer the diamond film.

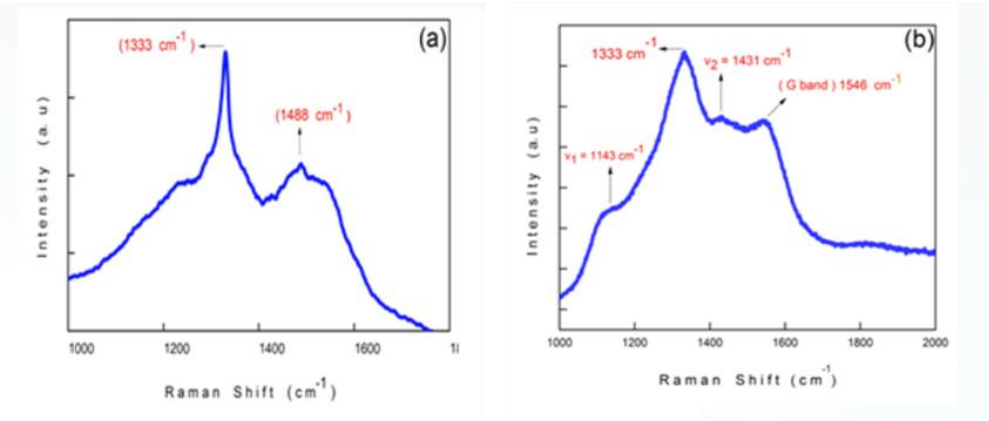

Figure 2.33 MCD and NCD (Najar et al., 2020).

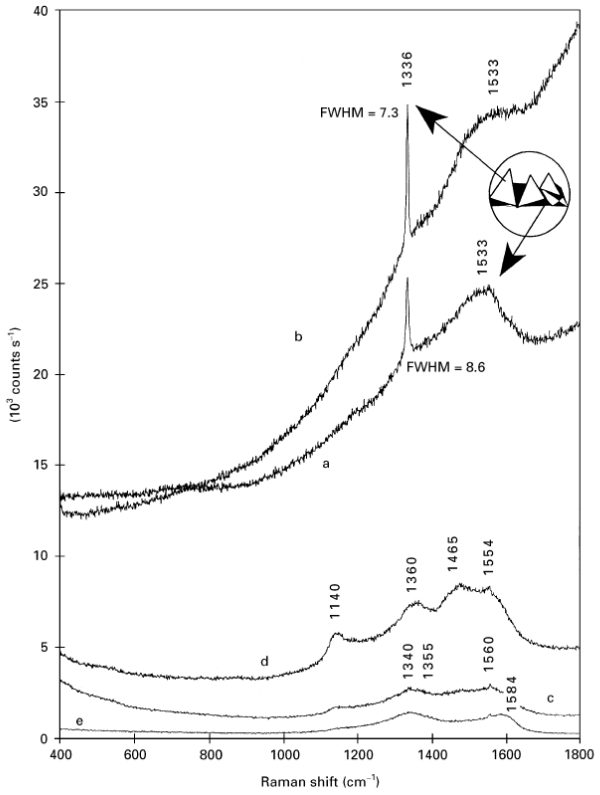

Figure 2.34 Full width at half maximum (FWHM) analysis indicating the crystalline quality of the diamond film. (Taher et al., 1996).

2.6.2 Destructive tests

There are two types of hardness testing: indentation testing and scratch testing. For indentation tests, geometrical aspects of the indentation is analysed after force is applied onto surface of the specimen. An example is the Rockwell test. For scratch tests,

it is observed whether surface of the workpiece can be scratched by a list of standard materials. In addition, Computer Numerical Control (CNC) machines can be used to simulate real usage of the coated cutting tools in the manufacturing industry.

Regarding indentation test, the Rockwell test determines adhesion and hardness of the coating by measuring the depth of penetration of an indenter under a load (Broitman, 2017), as shown in Figure 2.35. The level of adhesion is measured by comparing deformation profile of the coating and the substrate around the indented surface area.

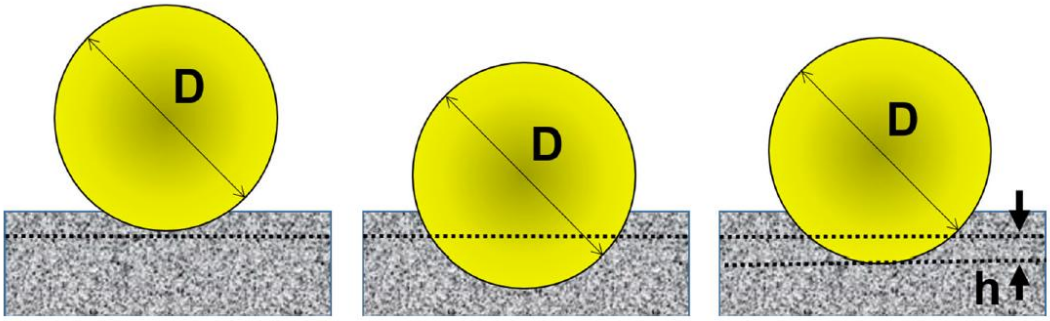

Figure 2.35 Indentation Principle of the indentation Rockwell measurement (Broitman, 2017).

Several authors used Rockwell indentation test to validate the diamond film quality (Chattopadhyay et al., 2008; Kao et al., 2010; Polini et al., 2000; Vidakis et al., 2003; Wang et al., 2016). Tang et al. (2016) classified acceptable and to-be-rejected coating film qualities based on the 6 levels of adhesion classes (HF1-HF6) which describe surface resistance of cracks, shown in Figure 2.35. They stated that indentation types of levels 1 to 4 (HF1-HF4) are acceptable, as only small cracks and regions of spallation appear around the indentation point. Levels 5 and 6 (HF5-HF6) are not acceptable, as large areas of spallation can be found around the indentation point. Figure 2.36 illustrates some samples of diamond coating films going through Rockwell indentation test (Xu et al., 2013).

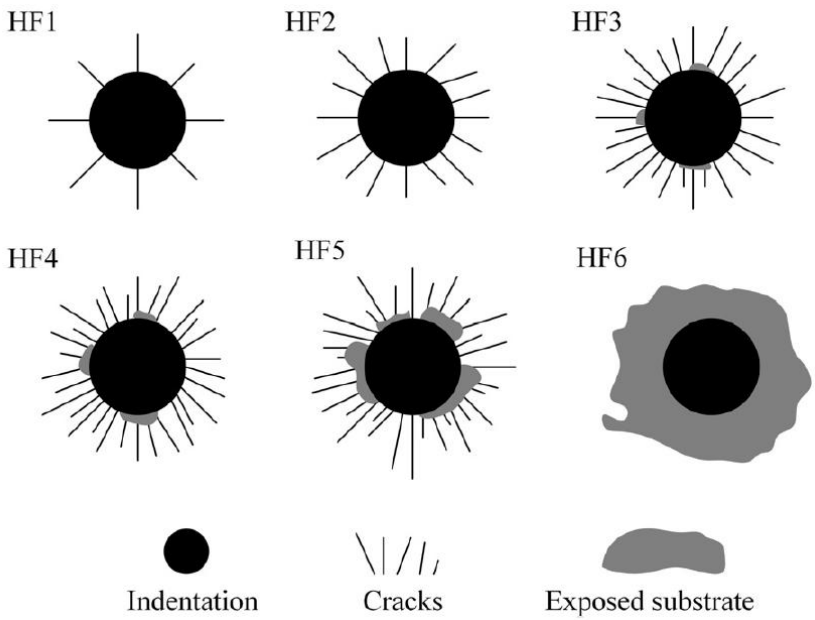

Figure 2.36 Level Adhesion level from HF1 to HF 6 by using Rockwell indentation (Tang et al., 2016).

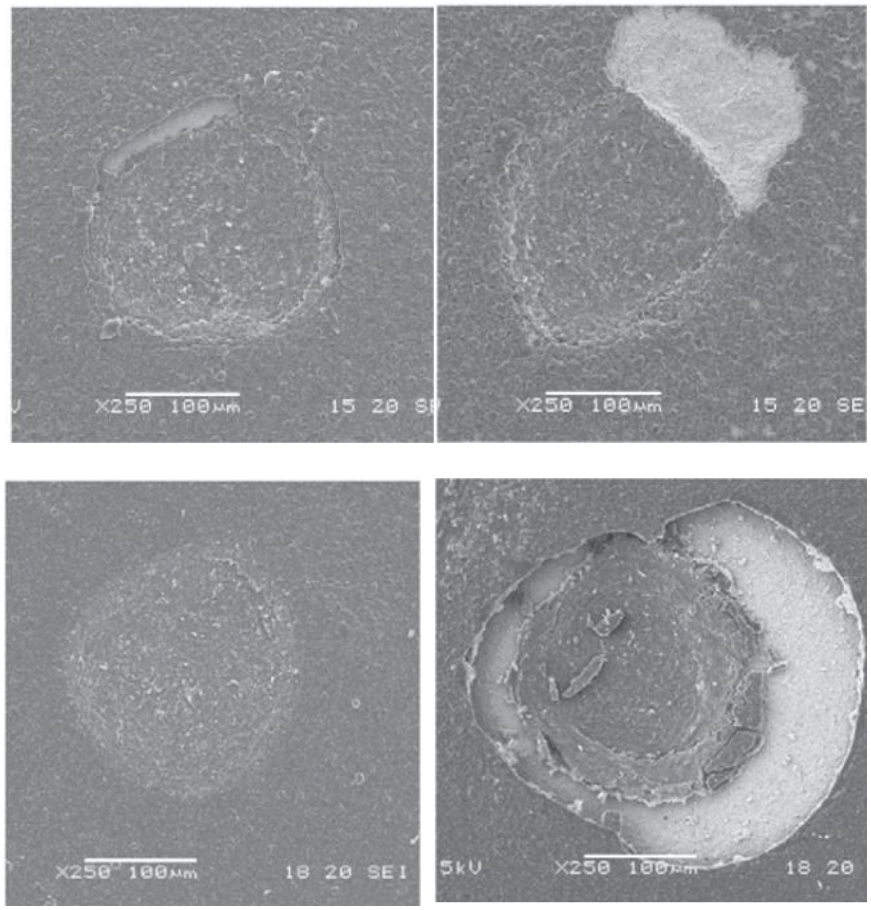

Figure 2.37 Diamond coating examples (Xu et al., 2013).

Regarding scratch test, it is one of the most practical approaches in evaluating adhesion of a hard thin coating film on a substrate surface (Barnes et al., 2012). For instance, scratch test can be used to examine film delamination, coating adhesion and surface resistance. It is a reliable and simple test that can be performed on any specimen regardless of its geometry.

Coating adhesion is measured as the number of times the amount of critical load can be applied before the coating fractures. A spherical indenter tip slides over the surface of the coating to generate a groove at an incremental or constant load mode. Applying a desired load (measured in nanometre depth) across distance (measured in millimetre length), the profile pass on the top surface is measured. Scratched tracks are characterised by coating film layer delamination from the substrate surface and coating film cracking.

Adhesion strength is a measure when a critical load is reached at which the substrate and the coating film interface delaminates (Lu et al., 2014). In addition, scratch testing may also be used to identify cracks on the coating film. While coating films with high hardness can withstand compressive stresses induced by the indenter to a certain extent, such films may fracture if a large amount of tensile stress or shear stress is applied. Coating film's cracking failure occurs when the mechanical work of the brittle failure in the coating is equal to the energy release rate from coating cracks. Ping Lu et al. (2013) states that for cemented carbide substrates like tungsten carbide, diamond delamination is due to insufficient adhesion between the coating and the substrate, partially as the result of the formation of non-diamond compounds at the substrate–diamond film interface due to the cobalt–carbon interdiffusion at CVD deposition temperatures.

According to Dumpala et al. (2014), scratch adhesion testing of NCD and MCD films on tungsten carbide substrates revealed that the predominant failure mode was spallation occurring in advance of the indenter. Parts of the scratch tracks of MCD and NCD coating layers captured by SEM are shown in Fig 2.37. It was observed that the failure mechanisms were different for the two coating films, and that this behaviour was attributed to their crystallinity. In particular, fractures in the MCD coating film are induced by compressive shear crack propagation, and they can be observed at the edge of the spalled region, due to the MCD film's high crystallinity and brittleness. While the MCD film failed due to delamination between the film and the substrate covering large area, edges of the spalled regions of the NCD film were almost normal to the substrate and only shear cracks appeared (Figure 2.37a). The MCD coating film was found to survive up until the critical load (Lc) of 42 N, whereas the NCD coating film was found to fail at the Lc of 20 N, as shown in Figure 2.37. The relatively poor scratch adhesion performance of the NCD film may result from both its lower intrinsic hardness and the possible occurrence of non-diamond carbon phases at the film–substrate boundary.

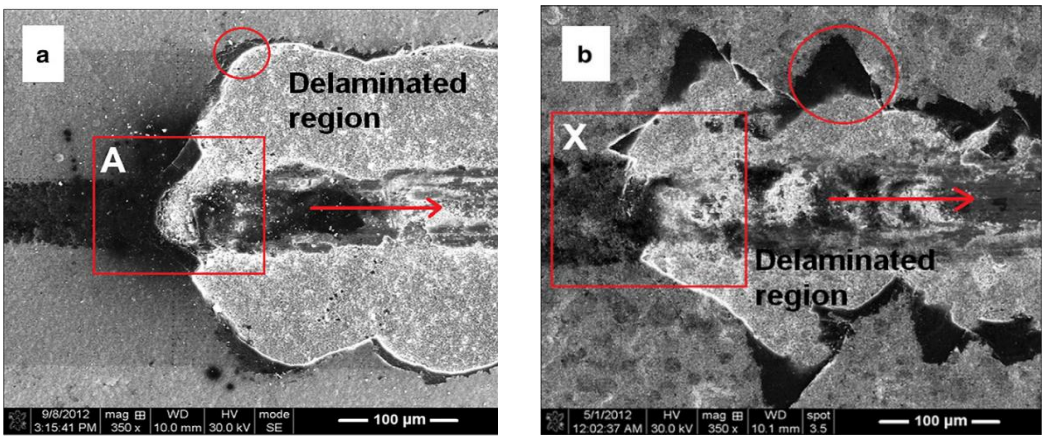

Figure 2.38 NCD and MCD scratch tests (Dumpala et al., 2014).

Dumpala et al. (2015) reported coating failure in CVD diamond films characterized by spallation in front of the scratch indenter, attributing it to compressive

shear stresses induced during the scratch test. Coating adhesion and the maximum sustainable stress prior to failure are the principal factors influencing the spalled area observed during spallation events., as shown in Fig 2.39.

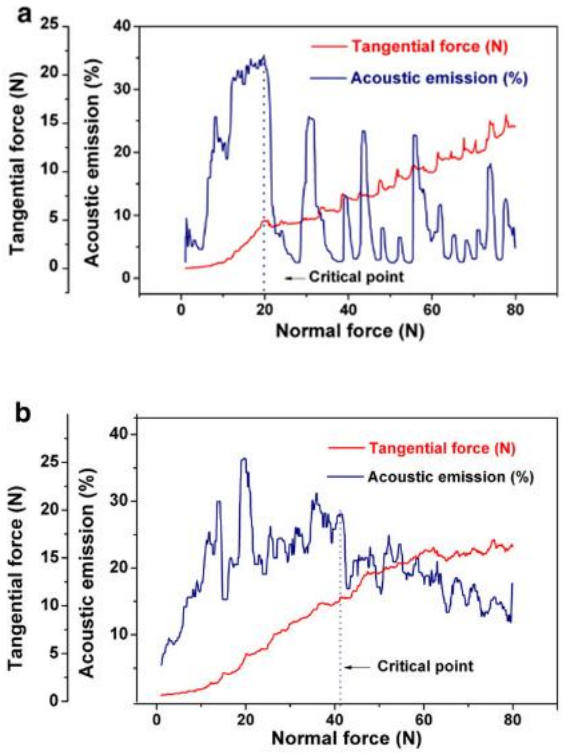

Figure 2.39 MCD and NCD films (Dumpala et al., 2014).

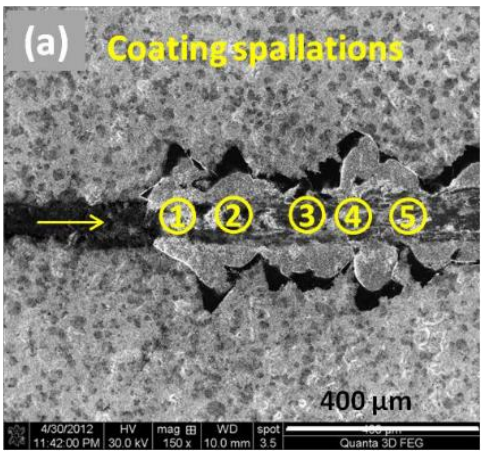

Figure 2.40 Coating spallation in the scratch track (Dumpala et al., 2015).

Chapter 3 Influence of HFCVD parameters on tool wear during high-frequency PCB machining

3.1 Introduction

In the rapidly evolving technological landscape, the move towards 5G communication systems has brought forth unprecedented demands on Printed Circuit Boards (PCBs). To meet the challenges of enhanced transmission speeds and thermal management, modern PCB designs have incorporated ceramic particles. While these ceramic components aid in improved heat dissipation, they simultaneously pose challenges concerning the machinability of the boards (Zhang et al., 2020).

Historical research efforts have delved deep into the intricacies of drill coating thickness and grain during the machining of third and fourth-generation PCBs, specifically the ones using copper-clad resin-based FR-4 (Lei et al., 2016; Wang et al., 2019; Zheng et al., 2015, 2016). However, as the industry is progressing towards the fifth generation, new challenges are emerging. These latest PCBs, vital for the robust 5G mobile communication infrastructure, boast of superior heat resistance and a notable reduction in transmission losses, setting them apart from their predecessors (Huang et al., 2020). Their unique composition, comprising copper-clad laminate, ceramic particles, anisotropic fibres, and epoxy resin, has intensified the machining challenges (Watanabe et al., 2008; Zheng et al., 2012).

Given the intricacies introduced by the new-gen PCBs, micro drills, known for their efficiency, have been widely adopted to create micro holes on these boards. But there's a caveat. The inherent properties of these drills, such as high anisotropy and limited thermal conductivity, lead to significant tool wear, compromising the quality of the drilled holes. These drills face the arduous task of enduring the abrasive wear

from ceramic components and the adhesive wear due to the molten resin at elevated temperatures (Zheng et al., 2012).

In response to these challenges, the HFCVD technique has gained traction. Employed to deposit protective diamond films on drills, this technique ensures the substrate remains shielded. This research endeavour is primarily anchored in identifying the ideal parameters namely, coating thickness and grain size suited for machining high-speed boards. Preliminary studies have underscored the promise of HFCVD-coated drills, which, intriguingly, showcase a lifespan extending beyond three times that of their non-coated counterparts (Gäbler et al., 2000).

Delving deeper, the HFCVD technique, with its assortment of pre-treatment methods and deposition parameters, induces variations in the characteristics of diamond films. The two main categories, MCD and NCD films, each have their set of advantages when it comes to tool protection. Their unique topographies and frictional coefficients translate to distinct machining outcomes (Wang et al., 2021). MCD films, for instance, exhibit commendable adhesion to substrates and provide enhanced wear resistance. In contrast, NCD films excel in delivering a smoother surface, resulting in refined finished products (Chen et al., 2013; Dawedeit et al., 2013).

3.2 Fabrication of drills with MCD and NCD by HFCVD

The HFCVD method is a prevalent technique for the deposition of diamond films on various substrates. In the realm of PCB drilling, understanding the influence of HFCVD processes on diamond-coated drill fabrication is imperative, especially when dealing with fifth-generation PCBs that incorporate ceramic particles. This chapter delves into the detailed processes and parameters of fabricating diamond-coated drills using HFCVD. Tungsten (W) and tantalum (Ta) are the most common filament materials used in HFCVD. As shown in Figure 3.1(a), methane (CH_4) and

hydrogen (H_2) flow through the hot filament region at the start of deposition. Under the combined effect of high filament temperature and reactive gas species, a tantalum filament can undergo carburisation, which increases brittleness over time. After passing through the filament region, the gas phase gains sufficient thermal energy for dissociation of H_2 and CH_4, producing atomic hydrogen (H) and hydrocarbon fragments. Atomic hydrogen plays a key role in diamond deposition by activating gas-phase chemistry and promoting surface reactions. In particular, hydrogen reacts with small hydrocarbon species to generate methyl radicals (CH_3), which are widely regarded as a main growth precursor for diamond in HFCVD.

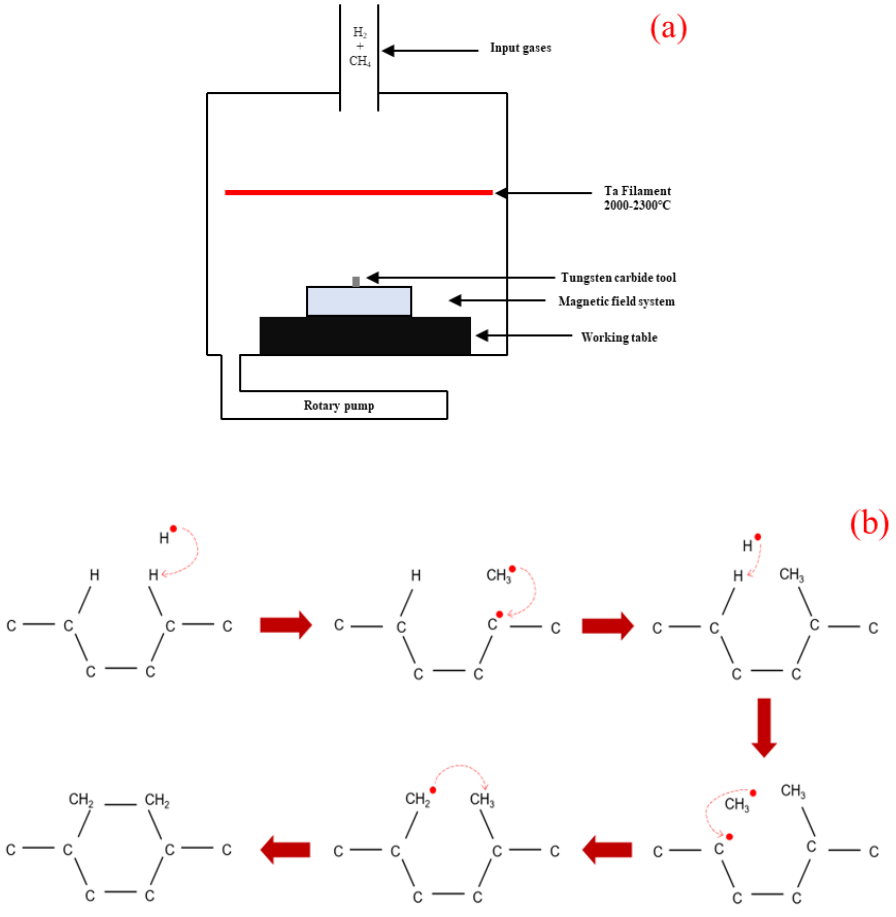

Figure 3.1 Schematic diagrams illustrating: (a) the layout of the HFCVD system and the endothermic bond-breaking process; (b) chemical gas reactions leading to the formation of a diamond layer on the substrate surface.

3.2.1 Pre-treatment of PCB drills

Before the deposition of diamond films, the PCB drill surface must undergo specific treatments to ensure optimal adherence and growth of diamond films. Initially, the drill surface is treated with Murakami's solution, comprising of a mixture of KOH, K3(Fe (CN)6), and water. This treatment facilitates the dissolution of WC into the chemical mixture, enhancing the substrate surface roughness. Following this, Caro's acid, a blend of H2O2 and H2SO4, is employed to eliminate cobalt from the surface, a crucial step that circumvents graphitization during the diamond film growth phase1.

3.2.2 HFCVD diamond coating process

The fundamental principle of the HFCVD technique lies in employing hydrocarbon gases as carbon precursors, while heated filaments supply the energy necessary for gas-phase dissociation and film growth. The thermal energy generated by the filaments initiates chemical reactions that facilitate the nucleation and growth of diamond films on the substrate surface. The primary carbon source is methane (CH_4), which reacts with the heat from commonly used filaments, such as tungsten (W) and tantalum (Ta). As the methane and hydrogen gas mixture passes through the heated filament, bond dissociation occurs, producing atomic hydrogen (H0). The presence of atomic hydrogen facilitates diamond growth by interacting with small hydrocarbon molecules, primarily methane (CH_4), resulting in the formation of methyl radicals (CH_3). The ensuing chemical reactions can be represented as:

$$H_2 \leftrightarrow H^0 + H^0 \quad (1)$$

$$CH_4 + H^0 \rightarrow CH_3 + H_2 \quad (2)$$

3.2.3 Diamond film growth on PCB drills

In the study, PCB drills (Ø1.1, 6% Co) made of tungsten carbide (WC) with a grain size between 0.5–0.8 μm were chosen. Both MCD and NCD films were

investigated, with coating thicknesses of 3 μm, 6 μm, and 9 μm as presented in Table 3.1. Specific deposition parameters were employed, including a tool temperature range of 800–900°C, methane flow rates between 20–80 sccm, and deposition durations spanning from 10–24 hours. The effects of substrate temperature, methane concentration, and deposition duration on the growth rate and grain size of the diamond films were investigated.

Table 3.1 Coating Types and Thicknesses of the Drill Samples.

Samples	Coating Type	Coating Thickness (μm)
M1	MCD	3
M2	MCD	6
M3	MCD	9
N1	NCD	3
N2	NCD	6
N3	NCD	9

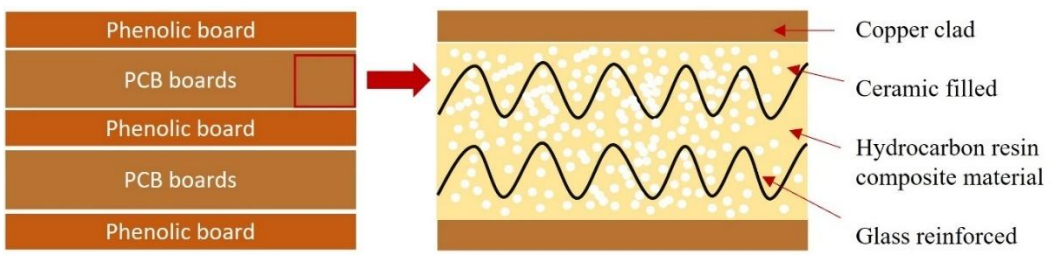

Figure 3.2 Schematic layout of board stacking configuration during machining and structural design of the PCB.

3.2.4 Observations and testing

Subsequent to the deposition process, scanning electron microscopy (SEM) was utilized to assess the coating thickness and grain size of the diamond films. The drilling performance of the coated tools was assessed on Rogers 4350B high-frequency PCBs using the VEGA-D2CMSL equipment. The condition of the drills was periodically assessed, specifically after every 1000 holes were drilled. Post-drilling, ultrasonic

washing with acetone was performed to cleanse the drills. Wear patterns and morphological changes were examined using a KEYENCE VHX-7000 digital microscope. Surface morphology assessments of the films were conducted using atomic force microscopy (AFM), and the adhesion characteristics of the films were analysed using the Rockwell indentation method.

3.3 Results and discussion

3.3.1 Effects of coating parameters on grain size and coating thickness

The process of HFCVD is a crucial step for achieving a controlled deposition of MCD and NCD films on PCB drills. The intricacies of this procedure revolve around a handful of parameters, including temperature, methane concentration, and deposition time. These parameters have profound effects on the outcome, especially in terms of grain size and coating thickness.

Figure 3.3 displays the surface microstructures and cross sectional views of the MCD and NCD coatings with thicknesses of 3 μm, 6 μm, and 9 μm.. The M1–M3 drills coated with microcrystalline diamond (MCD) films exhibit distinct columnar crystal growth, with well-defined grains ranging from 2 to 4 μm in size. In contrast, the N1–N3 drills coated with nanocrystalline diamond (NCD) films display clustered growth of nanoscale diamond grains, characterized by a cauliflower-like surface morphology. The observed differences in grain size and growth rates are attributed to variations in methane concentration, deposition time, and substrate temperature during the HFCVD process. Examining the cross-sectional profiles of the diamond-coated drills reveals noticeable differences between the MCD and NCD films. As demonstrated in Figure 3.4, the MCD coated drills (M1–M3) showcase a pronounced columnar crystal growth with grains ranging between 2–4 μm in size. In contrast, the NCD coated drills (N1–

N3) present a growth structure composed of nanosized diamond grains resembling a cauliflower-like arrangement.

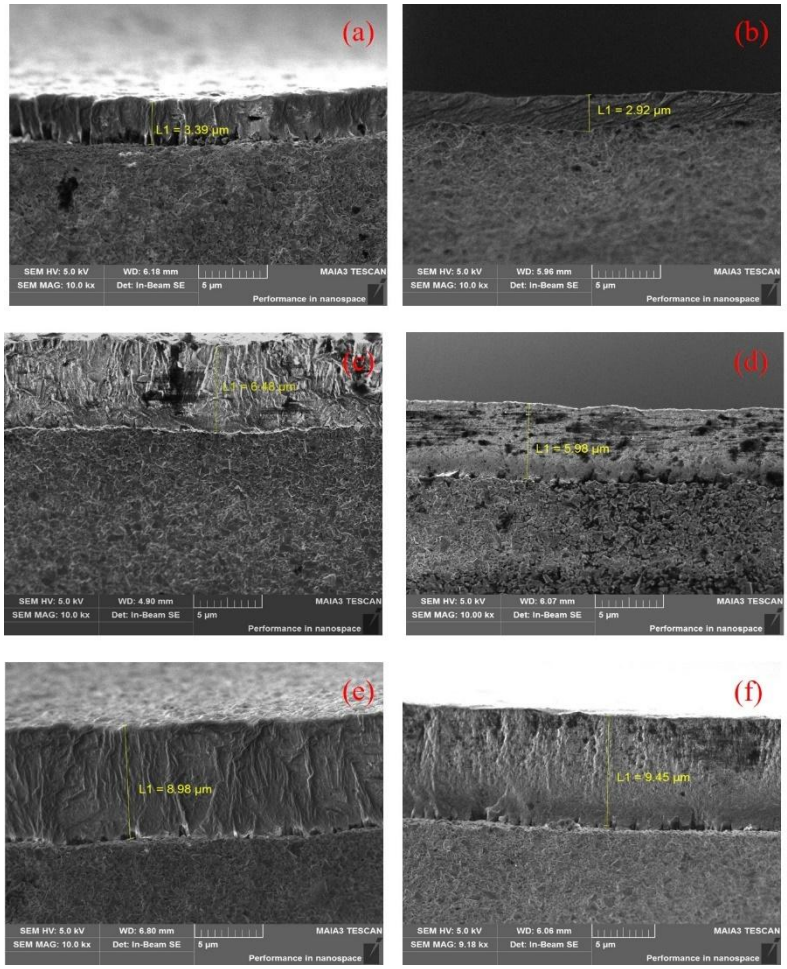

Figure 3.3 Cross-sectional SEM images of diamond-coated drills: (a) M1; (b) N1; (c) M2; (d) N2; (e) M3; (f) N3.

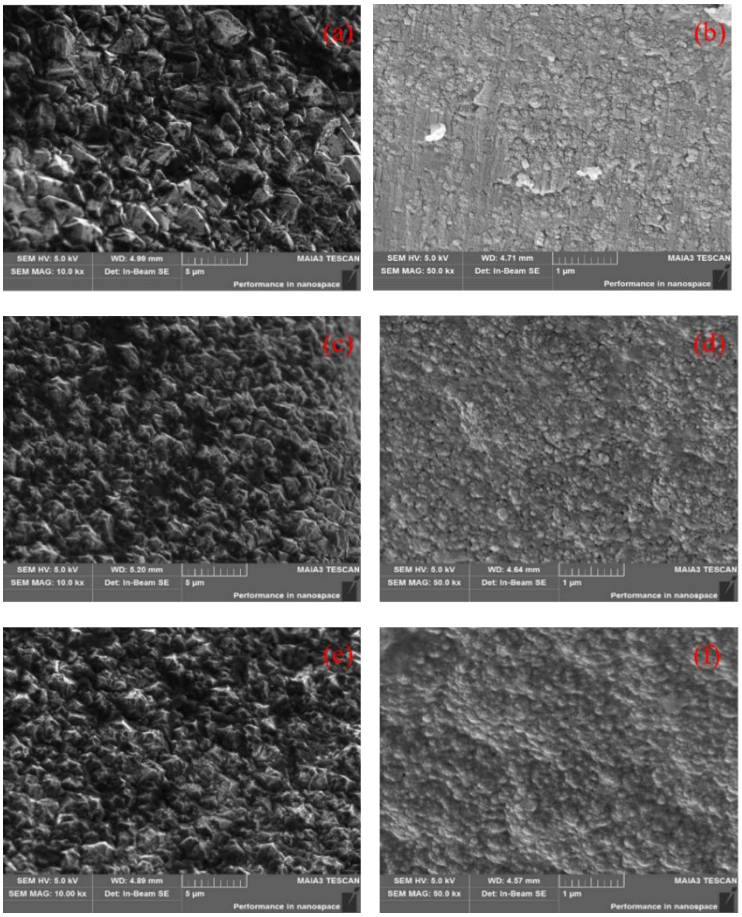

Figure 3.4 Surface morphology characterization of diamond-coated drill tools: (a) M1; (b) N1; (c) M2; (d) N2; (e) M3; (f) N3.

3.3.2 Surface morphology and roughness analysis

Surface roughness is a telltale indicator of the quality of the diamond film As shown in Figure 3.4, SEM imaging captures the surface morphology of the MCD and NCD films, which is further corroborated by AFM images in Figure 3.5 display similar structures of the MCD and NCD films. The AFM images, with dimensions of 10 μm × 10 μm, are presented in Figure 3.5. The average surface roughness (Ra) measured for drills M1, M2, and M3 was 91.4 nm, 107.6 nm, and 123.0 nm, respectively, while drills N1, N2, and N3 exhibited significantly lower roughness values of 22.3 nm, 25.7 nm, and 27.8 nm, respectively. The MCD films exhibited higher surface roughness due to

the uneven grain sizes, whereas the NCD films showed lower surface roughness owing to their smaller grains and lower coefficient of friction. The findings indicate that coating thickness has a limited influence on surface roughness, as evidenced by only a 32 nm increase from M1 to M3 and a 5 nm increase from N1 to N3. The findings demonstrate that surface roughness is primarily influence by film grain size, with coating thickness contributing minimally relative to other examined factors.

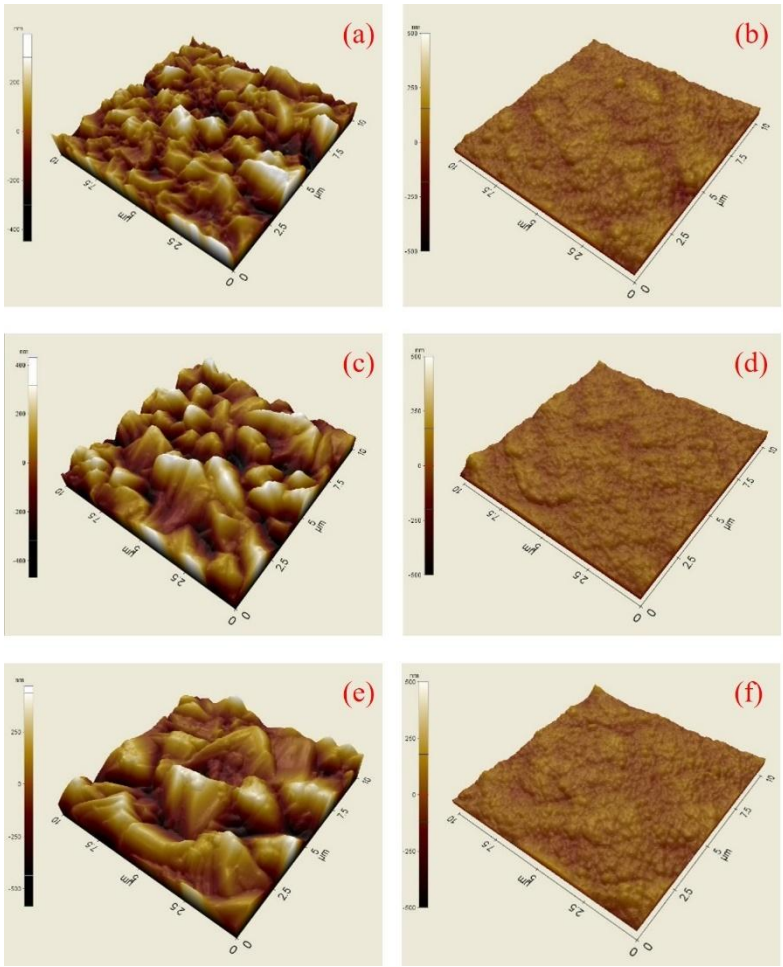

Figure 3.5 AFM Images of the surface morphology of diamond-coated drills: (a) M1; (b) N1; (c) M2; (d) N2; (e) M3; (f) N3.

3.3.3 Effect of coating thickness and grain size on adhesion strength

The adhesion strength of diamond coatings applied to WC-Co substrates was evaluated using the Rockwell A indentation test under a load of 588 N. The Rockwell

indentations on the tool surfaces, featuring 3 μm, 6 μm, and 9 μm MCD and NCD diamond coating layers, are depicted in Figure 3.6 using SEM images. Significantly, two primary defective outcomes were identified: crack propagation and coating delamination. The crack diameters upon delamination were measured on six samples, M1-M3 and N1-N3, with values of 120 μm, 110 μm, 101 μm, 158 μm, 135 μm, and 130 μm, respectively. The ranking of the deformation area can be established as follows: M3, M2, M1, N3, N2, and N1. Notably, cracks were visible on both the MCD and NCD films with thicknesses of 3 μm and 6 μm. It is noteworthy that samples M3 and N3, each with a 9 μm diamond coating, exhibited no evidence of crack initiation on their surfaces. Nonetheless, delamination occurred in both MCD and NCD films with thicknesses of 3 μm and 6 μm films with 3 μm and 6 μm thicknesses. It is worth noting that greater coating delamination was noted in samples with 3 μm coating layers compared to those with 6 μm coating layers, suggesting that the adhesion of the coating is more robust in thicker films. Overall, coating thickness emerged as the key factor affecting the adhesive strength of the diamond films, as demonstrated by the lack of crack propagation after indentation in the M3 and N3 samples.

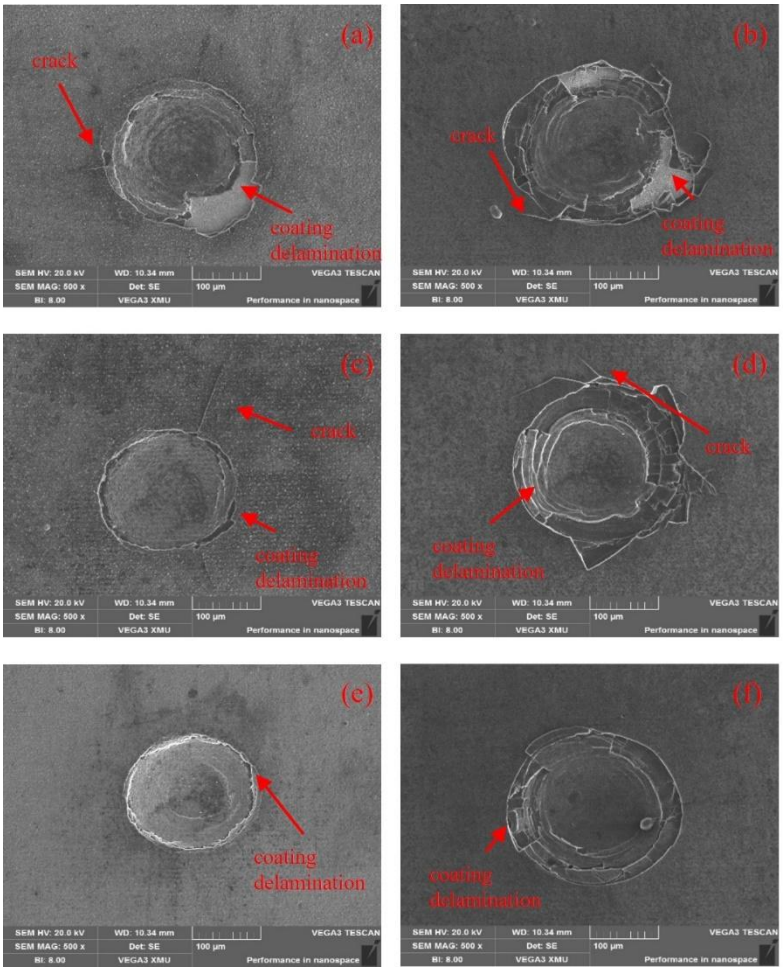

Figure 3.6 Rockwell A indentation results for diamond-coated drills: (a) M1; (b) N1; (c) M2; (d) N2; (e) M3; (f) N3.

3.3.4 Investigation on tool wear

To assess tool wear behaviour, six drills with varying grain sizes and film thicknesses were employed in the fabrication of micro-holes on high-frequency PCB substrates. It can be observed from Figure 3.7 that a notable amount of abrasive wear was detected on the flank face of both the MCD and NCD drills coated with a 3 µm thickness, following the completion of 1000 holes, leading to coating delamination. At 3 µm thickness, early edge delamination and local substrate exposure were observed, which increased damage for N1 under the tested drilling conditions. At higher thickness, improved coating coverage and load support reduced cutting-edge exposure,

supporting better durability and hole quality for thicker NCD coatings. This suggests that in contrast to MCD drills, NCD drills exhibit a prolonged tool lifespan owing to the reduced adhesion of the diamond film on the WC-Co substrate.

In the investigation of NCD drill wear, a comparison was made between coating thicknesses of 6 μm and 9 μm (N2, N3) after the completion of drilling 3000 holes. Despite noticeable abrasive tool wear evident in the NCD drills coated with 6 μm thickness (N2), the tool wear of N3 exhibited a consistent increase throughout the experimental process. The maximum lengths of flank wear for N3 ranged from 9.54 μm to 12.17 μm as the drilling progressed from 1000 to 5000 holes, respectively. Conversely, no apparent tool wear or coating delamination was observed in the case of 9 μm coating thickness (N3) after the drilling of 5000 holes. This can be attributed to the adequate thickness of the NCD film layer, which enables it to withstand both abrasive and adhesive wear when processing 5000 holes owing to its adhesive properties and smooth surface.

When drilling high-frequency PCBs, it is essential for drills to endure abrasive wear from the ceramic layer and adhesive wear resulting from molten resin adhering to the drill post-friction and heat generation during the process. The maximum length of flank wear for MCD and NCD drills with various coating thicknesses is depicted in Figure 3.8, indicating the superior performance of NCD-coated drills over MCD-coated ones. Moreover, a thicker coating layer leads to a reduced distribution of drilling force onto the drill substrate layer, thereby lowering the likelihood of localized delamination while enhancing elasticity and resistance to abrasive wear. Figure 3.7 does not showcase the tool wear of M1 and N1 since the maximum length of flank wear for these drills could not be measured due to tool cutting edge delamination after drilling 1000 holes. The ranking of tools in terms of lifespan is as follows: N3, M3, M2, N2,

M1, and N1. Notably, the maximum length of flank wear for NCD drills is approximately 90% less than that of MCD drills.

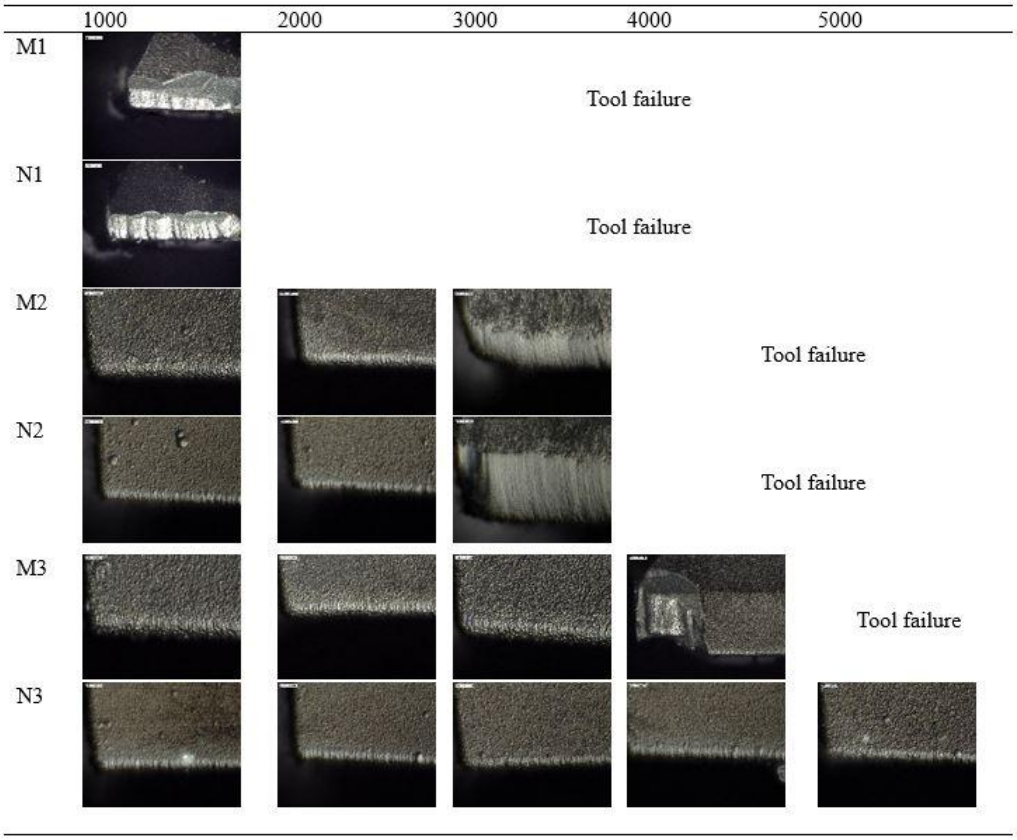

Figure 3.7 Flank wear states of diamond-coated drills after drilling 1000 to 5000 holes.: (a) M1; (b) N1; (c) M2; (d) N2; (e) M3; (f) N3.

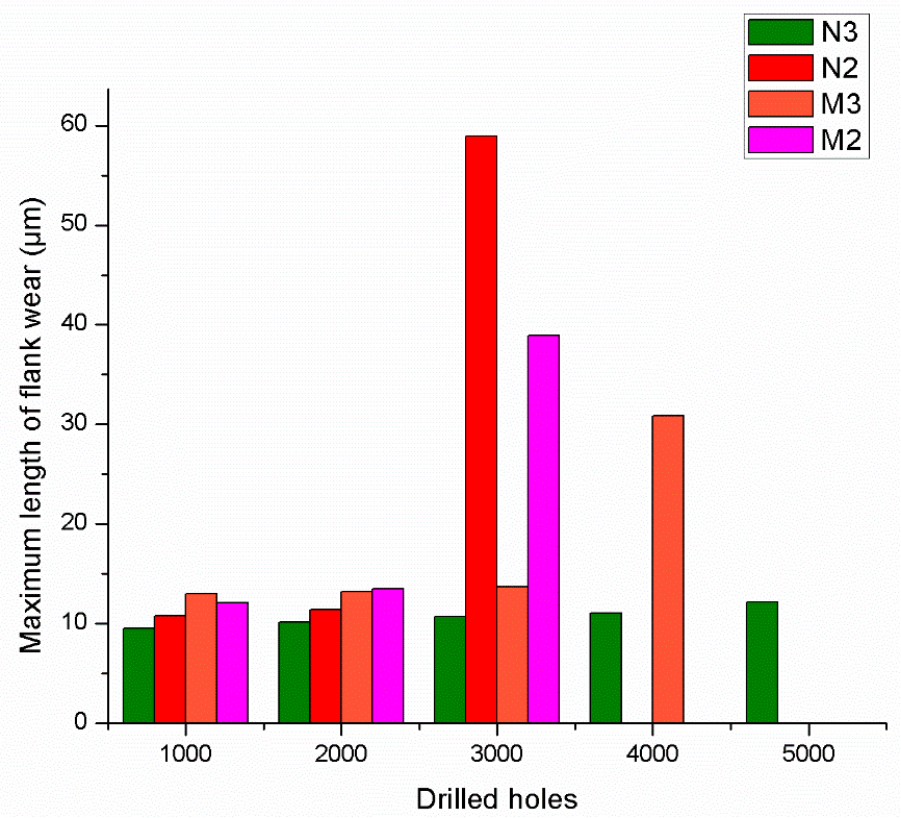

Figure 3.8 Maximum flank wear length of NCD and MCD coated samples with respect to the number of holes drilled.

3.3.5 PCB hole quality and wall roughness

Figure 3.9 illustrates the wall roughness of PCB hole walls after machining, a key quality indicator for finished PCBs. Along with wall roughness, dimensional accuracy, burr presence, resin smearing, and delamination are critical characteristics for evaluation. The grain size and thickness of the drill coating significantly influence the quality of the drilled holes. The data in Figure 3.9 show that as coating thickness increases, the surface roughness of PCB holes decreases.

When comparing 3 μm MCD-coated drills (M1) to 3 μm NCD-coated drills (N1), and 6 μm MCD-coated drills (M2) to 6 μm NCD-coated drills (N2), the MCD-coated drills consistently produce better hole quality than their NCD-coated counterparts. However, 9 μm NCD-coated drills (N3) can successfully drill over 5000

holes with a smooth surface, outperforming 9 µm MCD-coated drills (M3), which degrade after 3000 holes. Figure 3.9 demonstrates that NCD-coated drills yield PCB hole walls with surface roughness values approximately 30% lower than those produced by MCD-coated drills.

The condition of the drill significantly affects the quality of PCB holes, with wall roughness increasing as the tool deteriorates. The surface roughness of the drill coating directly impacts the roughness of the processed PCB hole walls. AFM results from Figure 3.5 reveal that NCD films have significantly lower surface roughness compared to MCD films. This lower roughness facilitates the chip removal process, allowing molten resin to be easily expelled from the flute. As a result, maintaining tool geometry helps to minimize the risk of delamination and microcracks within the PCBs.

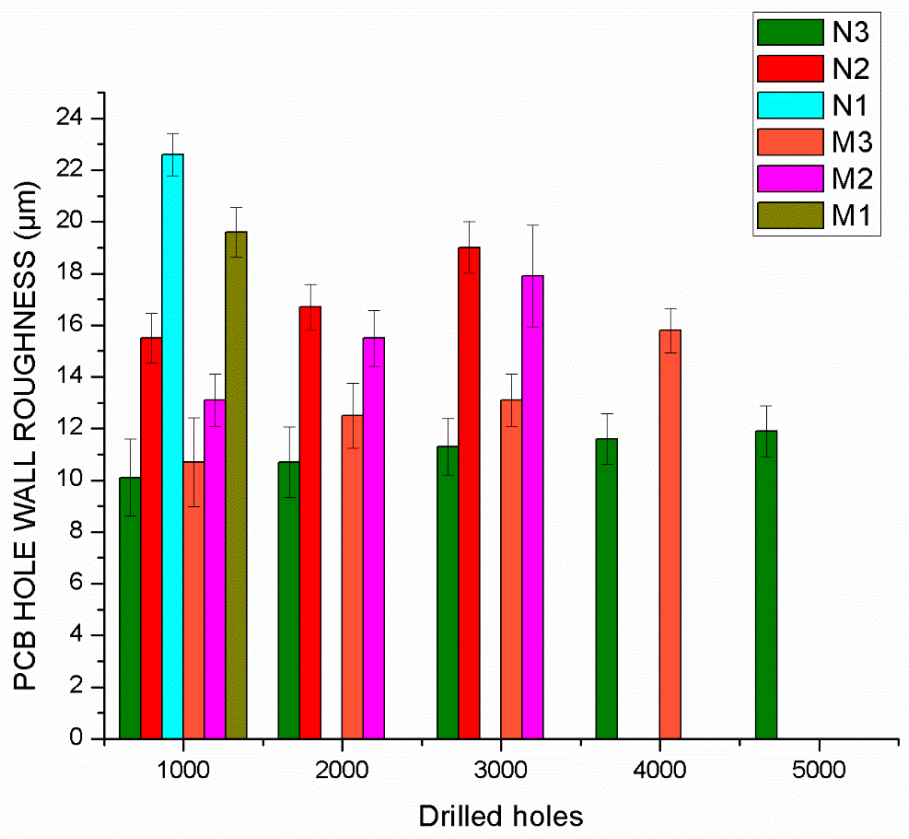

Figure 3.9 Variation in PCB hole wall surface roughness with the number of holes drilled using NCD and MCD coated tools.

3.4 Summary

This chapter detailed the comprehensive evaluation of diamond-coated drills with varied grain sizes and coating thicknesses, emphasizing their performance in drilling high-frequency and high-speed PCBs. The overarching objective was to bridge the gap in knowledge in this domain, ultimately benefiting both industrial applications and academic research. The major conclusions derived from the research are as follows:

The grain size of the diamond film undergoes a significant transformation based on the methane concentration. Specifically, as methane concentration surges, the film transitions from a microcrystalline to a nanocrystalline structure. This variation in grain size exhibits an inverse relationship with both substrate temperature and deposition time. A paramount advantage of thicker diamond coatings is the protection they offer to the underlying drill substrate. Under applied drilling forces, thicker coatings more effectively distribute the mechanical stresses throughout the entire coating layer. This ensures that the substrate remains largely shielded, reducing the risk of damage. Notably, Rockwell indentation tests indicated that when the coating thickness reached 9 μm, there was an absence of both crack propagation and coating delamination, highlighting the superior bond between the diamond film and the substrate.

Thicker diamond coatings impart enhanced wear resistance and durability to the drills. The force distribution mechanism in these drills ensures that localized delamination is minimized, as the coating thickness bolsters adhesion. In contrast, drills with thinner coatings bear the brunt of the drilling force both at the substrate and the coating level, leading to quicker wear and potential delamination. The tool's surface condition plays a pivotal role in determining the quality of the drilled holes. With their inherently smoother surfaces, NCD-coated drills promise superior hole quality, reducing defects such as burrs or resin smearing.

Chapter 4 Diamond film fabrication under low methane concentration via HFCVD with magnetic field assisted

4.1 Introduction

Diamond films, recognized for their remarkable set of properties such as superior thermal conductivity (Auciello & Sumant, 2010), high hardness (Montes-Gutiérrez et al., 2018), elevated electrical resistivity (Auciello & Aslam, 2021), and consistent chemical stability (Shen & Sun, 2009), have been integrated into various technological applications, ranging from electronic devices to cutting tools and thermal regulation systems. Their inherent resistance to wear and chemical impacts makes them a preferred choice in challenging operational environments.

The increasing demand for diamond films has led to the development of efficient methods to accelerate their growth rate. One such method, HFCVD involves the decomposition of hydrocarbon gases, predominantly methane, in the vicinity of a heated filament. This results in the deposition of carbon atoms on a substrate, forming diamond structures. The process is significantly influenced by radicals and ions, specifically those derived from the breakdown of methane (CH_4) and hydrogen (H_2) molecules, such as [H], [CH], [CH_2], and [CH_3]. These components critically affect both the growth rate and the grain size of the resultant diamond(Roy et al., 2002; Yu et al., 1997). However, cultivating top-tier diamond films with excellent crystalline quality and smooth surfaces is a nuanced task, especially when working with reduced methane concentrations. The limited availability of methane curtails the supply of carbon atoms, which may affect the density of nucleation sites essential for achieving optimal crystalline quality.

Various strategies have been devised for producing diamond films via HFCVD. These include the selection of diverse carbon-source precursor gases like methane

(Wang et al., 2021), methanol (Wang et al., 2015), and acetone (May et al., 1993), choice of filament materials such as tungsten and tantalum(Kwok et al., 2022; Moustakas, 1989), optimization of filament temperatures, substrate pre-treatment methods, and nucleation techniques. An emerging trend in this domain is the incorporation of magnetic fields into the HFCVD process. While there have been several studies exploring the potential of magnetic fields in HFCVD (Long et al., 2015; Wang et al., 2018; You et al., 2009), a comprehensive understanding, especially of the permanent magnetic field setup within HFCVD, is still in its infancy. Most studies have traditionally positioned the magnetic system externally due to the high temperatures within the chamber, leading to a relatively diluted magnetic flux density within the reaction chamber (Li et al., 2017; Liu et al., 2023; Wang et al., 2017; Wu et al., 2012). Introducing Samarium–Cobalt (SmCo) magnets internally, in proximity to the tungsten carbide tool, suggests the potential for a more intensified and localized magnetic field. Such an arrangement could offer refined control over the magnetic field in specific chamber regions, enabling the optimization of film characteristics and growth rates.

This chapter delves into the influence of magnetic fields on diamond film growth under limited methane conditions during HFCVD and elucidates the underlying coating mechanisms. By comparing diamond films grown with and without magnetic field assistance, it seeks to understand the magnetic field's role in influencing growth rates, film quality, and other related properties. Using both experimental and simulation-based approaches, the chapter aims to gain insights into how magnetic fields affect reactive gas species within the HFCVD process and their subsequent effects on diamond deposition.

4.2 Experimental procedures and set up

4.2.1 Design of magnetic field system in the HFCVD machine

In the design of the magnetic field system for the HFCVD machine, precision and attention to materials' properties are paramount. Figure 4.1(a) displays the practical arrangement of the system components. Central to this setup are the filaments, typically composed of tungsten, which play a crucial role in initiating the chemical reactions for film deposition by thermally decomposing the precursor gases. These filaments are suspended parallel over the working table, the location for substrate placement. Below these elements, a thermocouple is strategically placed to monitor and maintain the requisite temperature conditions necessary for the deposition process.

Adjacent to this thermal assembly is the magnetic field assistance setup. Although not explicitly showcased in the provided image, its implied function is to introduce a magnetic field to the deposition zone. This integration is designed to create a magnetic environment that is consistent over the area where the substrate is located, based on the strategic placement of the field-generating components.

Complementing the experimental setup, Figure 4.1(b) offers a schematic illustration that expounds on the configuration of the magnetic field within the HFCVD system. It presents a cross-sectional view, showing the direction of the magnetic flux, indicated by uniform horizontal arrows. This suggests an even distribution of the magnetic field in the region where the substrate is positioned. The depiction implies that the field is generated by components such as permanent magnets or electromagnetic coils, which are not visible in the figure.

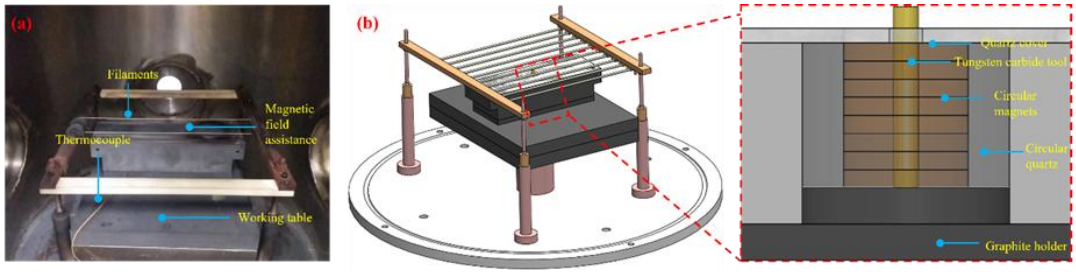

Figure 4.1 Configuration of the HFCVD system incorporating magnetic field system: (a) Overview of the experimental setup; (b) Schematic illustration of the magnetic field system.

The schematic denotes the use of SmCo magnets, chosen for their capability to endure the high-temperature environment of HFCVD. These magnets are ensconced in a graphite holder and positioned centrally beneath the filament and around the tungsten carbide workpiece. Quartz insulation is utilized to encompass the workpiece, magnets, and the graphite holder's top surface, serving to mitigate heat transfer and protect the magnetic properties of the SmCo magnets at elevated operational temperatures. This system's design aims to facilitate the examination of magnetic field interactions with the charged particles in the deposition chamber, hypothesizing that such interactions may influence particle behaviour and energy profiles. These effects could, in turn, impact the growth and structural characteristics of the deposited films. The field strength is set at 400mT, providing a quantifiable parameter for the investigation of these potential influences.

Overall, the design of a magnetic field system within an HFCVD apparatus is aimed at enhancing the control over the deposition environment. The objective is to utilize magnetic fields to potentially influence the kinetics of the film formation process, which, in theory, could lead to variations in the microstructural properties of the deposited films. However, the efficacy and benefits of such a system would necessitate

rigorous experimental validation to confirm the theoretical advantages in practical applications. The design thus provides a foundation for further investigation into the interplay between magnetic fields and material deposition.

4.2.2 Deposition of diamond films

The study employed square rod (D4, 6% Co) tungsten carbide (WC) specimens with a grain size ranging between 0.5-0.8μm. Before diamond film deposition, the surface of the square rod underwent chemical pretreatment using Murakami's reagent *(KOH: $K_3(Fe(CN)_6$: H_2O= 1:1:10)* followed by Caro's acid *(H_2O_2 + H_2SO_4)*. The present work investigates the effect of magnetic fields on diamond film growth, where M1 and N1 refer to diamond film growth with and without magnetic field assisted, respectively, as shown in Table 4.1. Table 4.2 summarizes the experimental parameters selected for the diamond film deposition process. These included scanning electron microscopy (SEM: Tescan MIRA), a micro-Raman spectrometer (Renishaw) with 532nm wavelength, and an X-ray Diffractometer (Rigaku SmartLab). The study employed several techniques to examine the structure and quality of the diamond films. SEM was used to observe the surface morphology and grain structure of the diamond films, while the growth rate of the films was quantified. Raman spectroscopy was utilised to determine the purity of the diamonds and identify any defects present in the diamond films. The orientation of the diamond crystals was determined using XRD. These results provide a comprehensive view of the properties of the grown diamond films.

Table 4.1 Magnetic field intensities applied for different sample growths in HFCVD.

Samples	Magnetic field strength
M1	400mT
N1	-

Table 4.2 Experimental parameters for diamond film used in HFCVD.

Parameters	Deposition conditions
Power (W)	3000
Number of filaments	2
Hydrogen content (sccm)	2000
Methane content (sccm)	10
Tool temperature (℃)	800
Filaments temperature (℃)	2300
Pressure (Pa)	1500
Deposition Duration (h)	6

4.3 Multi-physics simulation of magnetic field-assisted HFCVD

The simulation of the HFCVD process under the influence of a magnetic field has been carried out using the COMSOL Multiphysics software. The virtual model is constructed as a cylindrical chamber with a diameter of 400 mm and height of 500 mm, segmented into four primary zones: the inlet, the gas reaction chamber, the deposition space, and the outlet. Each zone serves a unique function in the deposition process, from the entry and reaction of gases to the deposition of thin films and the exit of exhaust gases.

Utilizing the heat transfer module in COMSOL, temperature distribution throughout the chamber is mapped. This involves a comprehensive analysis of heat conduction, convection, and radiation effects that are pertinent to the deposition process. The gas flow dynamics are encapsulated by employing the laminar flow

module, reflecting the typical flow conditions within HFCVD reactors. Incorporating the magnetic forces in the simulation requires solving the continuity equation and the Navier-Stokes equations for fluid flow, with an added term representing the magnetic force interaction. This additional force is crucial for understanding how the charged particles in the gas phase respond to the magnetic field presence.

The simulation allows for adjustment of variables such as gas inlet velocity, reactor pressure, and magnetic field intensity. By altering these parameters, their impact on the thermal and fluid distribution can be studied, providing a detailed prediction of the process behaviour under different conditions. The results from the COMSOL simulations are intended to offer a deeper comprehension of the magnetic field-assisted HFCVD process, potentially leading to refined control over deposition quality. This simulation-based approach aids in the identification of optimal operational conditions, which can then be tested and verified through experimental examination.

4.3.1 Simulation setup

Figure 4.2 depicts the layout of the HFCVD system, showing the coaxial arrangement of the workpiece and its fixture relative to the filament. The entry of gases such as hydrogen and methane into the system leads to their thermal decomposition into carbon and hydrogen radicals and ions, a critical process in deposition outlined in (Hu et al., 2019). A ring magnet, integrated within the fixture, allows for adjustment of magnetic field strength, which influences the trajectory and behaviour of ions and paramagnetic radicals (Kanaya & Kawakatsu, 1972). Analysis of the magnetic field's influence encompasses the examination of density distributions and deposition rates of ions and radicals on the surface of the workpiece. Secondary emissions are considered to have negligible energy and, thus, minimal impact on the deposition process. The

investigation here is confined to the elastic scattering between ions and radicals, highlighting the interactions of charged particles in the HFCVD environment. Neutral species, although participating in collisions, are not subjected to the Lorentz force, and their role is not considered central to the current study. This research primarily focuses on elastic scattering from ion-ion and radical-radical collisions. However, the hot tantalum filament is also significant in the decomposition of hydrogen and methane gases into reactive species. The high-temperature environment above the filament converts precursor molecules into carbon and hydrogen radicals and ions, reducing the number of undecomposed molecules on the substrate surface. Thus, collisions involving molecules, including those that remain undecomposed, have a significantly lower potential impact under our experimental conditions. Our analysis is guided by the efficient decomposition process that underpins the simulation setup and experimental focus, allowing us to focus on the interactions most relevant to the observed growth of the diamond film.

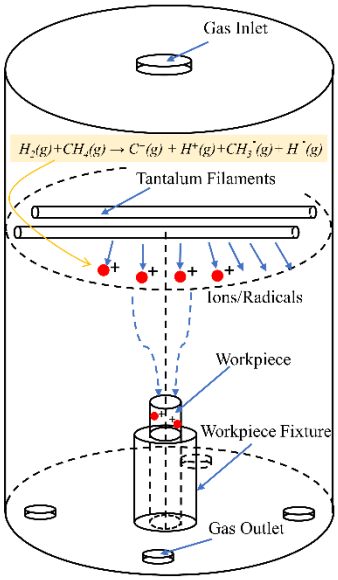

Figure 4.2 Schematic diagram of deposition on the workpiece surface.

4.3.2 Magnetic field configuration

The magnetic field distribution produced by the ring magnet within the workpiece fixture is determined using Maxwell's equations (Equations 1, 2, and 3). These equations describe the magnetic field intensity vector ($\vec{H}$), magnetic flux density vector ($\vec{B}$), total current vector ($\vec{J}$), and magnetic potential vector ($\vec{A}$). A relative permeability model informs the external magnetic field of the workpiece (Equation 4), involving vacuum permeability (μ_0) and relative permeability (μ_r).

$$\nabla \times \vec{H} = \vec{J} \tag{1}$$

$$\vec{B} = \nabla \times \vec{A} \tag{2}$$

$$\vec{J} = \sigma \vec{E} + \vec{J}_e \tag{3}$$

$$\vec{B} = \mu_0 \mu_r \vec{H} \tag{4}$$

The magnetic field's behaviours aligns with the conductivity conduction model (Equation 5) and the dielectric model (Equation 6), involving current density ($\vec{J}_c$), electrical conductivity (σ), electric field intensity ($\vec{E}$), electric flux density (D), ε_0 is the vacuum dielectric constant and the relative dielectric constant (ε_r). The workpiece fixture's B-H curve adheres to a magnetization model considering residual magnetic flux density (Equation 7).

$$\vec{J}_c = \sigma \vec{E} \tag{5}$$

$$D = \varepsilon_0 \varepsilon_r \vec{E} \tag{6}$$

$$\vec{B} = \mu_0 \mu_{rec} \vec{H} + \vec{B}_r, \quad \vec{B}_r = \left\| \vec{B}_r \right\| \frac{\vec{e}}{\left\| \vec{e} \right\|} \tag{7}$$

Adjustments to the magnetic induction intensities via the ring magnet within the fixture result in variable magnetic fields, characterized by auxiliary functions

(Equations 8 and 9). $\vec{A}$ is referred to as the dynamic vector magnetic potential, or magnetic vector potential; $\vec{U}$ is referred to as the dynamic potential.

$$\vec{B} = \nabla \times \vec{A} \tag{8}$$

$$\vec{E} = -\nabla \vec{U} - \frac{\partial \vec{A}}{\partial t} \tag{9}$$

By incorporating specific vector identities and laws from Maxwell's equations (Equations 10 to 13), the electromagnetic field parameters are defined for both dynamic and steady-state conditions. The computational solutions for the electric field intensity (E) and magnetic induction intensity (B) are facilitated through the COMSOL Multiphysics software (version 6.1), within the Lorentz framework.

$$\nabla \times (\vec{B} / \mu) = \vec{J} + \frac{\partial (\varepsilon \vec{E})}{\partial t} \tag{10}$$

To deduce

$$\nabla \times (\frac{1}{\mu} \nabla \times \vec{A}) = \vec{J} + \frac{\partial}{\partial t} [\varepsilon (-\nabla \vec{U} - \frac{\partial \vec{A}}{\partial t})] \tag{11}$$

Use vector identities $\nabla \times \nabla \times \vec{A} = \nabla (\nabla \times \vec{A}) - \nabla^2 \vec{A}$, the above equation becomes,

$$\nabla^2 \vec{A} - \mu\varepsilon \frac{\partial^2 \vec{A}}{\partial t^2} = -\mu \vec{J} + \nabla (\nabla \times \vec{A} + \mu\varepsilon \frac{\partial \vec{U}}{\partial t}) \tag{12}$$

Equation (12) is substituted into Coulomb's law of Maxwell equation $\nabla \cdot \vec{E} = \rho / \varepsilon$ to deduce:

$$\nabla^2 \vec{U} + \frac{\partial}{\partial t} (\nabla \times \vec{A}) = -\frac{\rho}{\varepsilon} \tag{13}$$

In the special case where the electromagnetic field is time-independent, the synthesis of equations (1) - (13) yields Equation (11).

$$\nabla^2 \vec{A} = -\mu \vec{J} \tag{14}$$

Since ∇^2 is the second partial derivative with respect to the space coordinate system, the above equation is a nonhomogeneous second order partial differential

vector equation. The COMSOL Multiphysics software (version 6.1) can be used for its solution. Under the Lorentz condition, solving for the magnetic vector potential A provides the electric field intensity E and magnetic induction intensity B.

4.3.3 Particle flow state specification

The velocity and pressure fields of a single-phase fluid in the laminar flow state are calculated using the laminar flow model. The flow remains laminar if the Reynolds number is below a certain critical value. If the Reynolds number exceeds this value, perturbations grow and cause a transition to turbulence. It is important to note that the critical Reynolds number is dependent on the model used. The particle emission flow in the designed model resembles the central axis of the reactor flow, which has a critical Reynolds number of approximately 2000. To ensure the validity of the laminar flow assumption in the simulation, the experimental setup closely matched the reactor size and gas flow rates to the simulation parameters. This correspondence ensures that the laminar flow conditions used in our simulations accurately reflect the experimental conditions, addressing concerns about the possibility of a diffusion-dominated process.

Particles are introduced at the axis and directed towards the workpiece surface via the ion source. The particle movement is simulated using both Reynolds-Averaged Navier-Stokes (RANS) and k−ϵ turbulence models, with a wall function addressing the interaction with surfaces. Turbulence parameters such as the velocity scale (U_{scale}) and length scale (L_{fact}) are set to predefined values, 1m/s and 0.035m, respectively. The governing equations for particle motion in a steady-state scenario (Equations 15 to 21) allow for the comprehensive calculation of the velocity field, accounting for fluid density, particle velocity, pressure, dynamic viscosity, and turbulent kinetic energy. These calculations facilitate the subsequent particle tracking analyses to assess deposition conditions on the workpiece surface under various magnetic field influences.

$$\rho(u\cdot\nabla)u = \nabla\cdot[-p2I + K] + F \tag{15}$$

$$\rho\nabla\cdot u = 0 \tag{16}$$

$$K = (\mu + \mu_T)(\nabla u + (\nabla u)^T) \tag{17}$$

$$\rho(u\cdot\nabla)k = \nabla\cdot[(\mu + \mu_T\sigma_k^*)\nabla k] + p_k - \beta_0^*\rho\omega k \tag{18}$$

$$\rho(u\cdot\nabla)\omega = \nabla\cdot[(\mu + \mu_T\sigma_\omega)\nabla\omega] + \alpha\frac{\omega}{k}p_k - \rho\beta_0\omega^2 \tag{19}$$

$$\mu_T = \rho\frac{k}{\omega} \tag{20}$$

$$p_k = \mu_T[\nabla u : (\nabla u + (\nabla u)^T) \tag{21}$$

ρ is the density of fluid particles; u is the particle velocity, where the initial velocity of the particle at the source is set o10m/s in a downward direction (0,0,-1); p is the pressure with an initial value of 1atm; I is the mixing length limit; μ is the dynamic viscosity of the fluid, where the fluid's constitutive relation is Newtonian. T is the time scale; β_0^* is the slip length; k is turbulent kinetic energy.

Through COMSOL software (version 6.1), the velocity u, velocity component u_{1x}, u_{1y}, u_{1z}, outlet pressure p_2 and turbulent kinetic energy ω of the velocity field in the fluid domain of particles can be calculated. Consequently, particle tracking can be employed to determine the deposition conditions on the workpiece surface, both with and without a magnetic field.

4.3.4 Mathematical framework for particle tracking

The assessment of particle deposition, with and without the influence of a magnetic field, is integral to the understanding of the coating process dynamics. The particle tracking module is engaged to simulate the particle trajectories once the magnetic configurations and initial conditions for particle release have been defined. Particles emitted from the ion source are subjected to the Lorentz force, resulting from the combined effects of the magnetic field and particle inertia. The equation governing

the motion of particles under these forces is given by Equation (22), which is pivotal for predicting the final deposition patterns on the workpiece.

$$\frac{d(m_p\vec{v})}{dt} = \vec{F}_t \tag{22}$$

In this equation, m_p represents the particle mass, $\vec{v}$ is the particle velocity, and $\vec{F}$ denotes the net force experienced by the particle.

Upon entering the flow field from the source, the particles adhere to Newton's second law of motion, detailed in Equations (23) through (26).

$$\vec{q} = \vec{q}_0 \tag{23}$$

$$v = v_0 \tag{24}$$

$$f(\theta,\varphi) = \frac{1}{2\pi}(1-\cos\alpha)\sin\theta \tag{25}$$

$$\theta \in [0,\alpha] \tag{26}$$

These equations encompass the kinetic energy of the particles $\vec{q}$, velocity of the particle v and release angle α . The simulation initiates with a batch of 1000 particles for a statistically significant analysis.

As particles make contact with the workpiece surface, they transition to a stationary state upon deposition. The wall boundary condition is adjusted to a 'frozen' state, allowing particles to adhere to the boundary grid. An accumulator is employed to quantify the deposition, represented in Equation (27), which is essential for comparing the deposition rates in the presence and absence of a magnetic field.

$$\frac{\partial Nd}{\partial t} = \frac{1}{meshvol}\sum_{i=1}^{N} R_i \tag{27}$$

Within this equation, Nd denotes the cumulative variable, $meshvol$ is the surface mesh area on the workpiece, and R_i is the initial number of released particles.

The totality of particles within the fluid domain and the quantity adhering to the workpiece allows for the determination of particle deposition density and rate under varying magnetic conditions.

4.3.5 Simulation setup for solid heat transfer

Solid heat transfer modelling incorporates the fundamental mechanisms of conduction, convection, and radiation within solid materials. The governing temperature distribution is derived from Fourier's law, expressed in its differential form within the solid matrix. Quadratic Lagrange polynomials serve as the standard shape function for temperature distribution within the domain. Solid heat transfer is simulated using the steady-state conditions of the magnetic field and ion movements as captured in Equations (28) and (29):

$$\rho C_p \vec{u} \cdot \nabla T + \nabla \cdot \vec{q} = Q + Q_{ted} \tag{28}$$

$$\vec{q} = -k \nabla T \tag{29}$$

Here, ρ is the density of the solid, C_p its specific heat at constant pressure, k the thermal conductivity (scalar or tensorial to account for anisotropy), $\vec{u}$ the velocity field associated with any material movement, Q represents heat sources within the domain, q is the heat flux vector, and ∇T the temperature gradient.

4.3.6 Boundary conditions and mesh generation

The computational simulation employs the COMSOL laminar flow model. An incompressible flow physical model defines the boundary conditions with a standard atmospheric pressure level and a reference temperature of T_{ref}= 293.15K. The simulation assumes the fluid's density and viscosity as constants, employing a steady-state solver with a relative tolerance of 0.001 for precision. The solver's design, a segregated solver, enhances ease of operation and robustness, especially pertinent for small-scale simulations. No-slip boundary conditions are imposed on the walls of the

domain, and to counteract any non-ideal flow conditions at the inlet, the inflow is modelled as fully developed, with the mean velocity tailored to specific test requirements. The outlet is defined with a pressure boundary condition, complemented by a backflow prevention mechanism to maintain a unidirectional flow field.

4.3.7 Strategy for grid partitioning

The mesh comprises free tetrahedral elements, with Figure 4.3 showcasing the grid partitioning for the gas inlet, reactor's central axis, workpiece, and fixture. The meshing strategy prioritizes quality and computational accuracy, with a minimum cell size of 0.08 mm along the reactor's central axis, a maximum cell growth rate of 1.05, and a curvature factor of 0.2. Table 4.3 catalogues the grid information across different cell regions, noting the spatial arrangement from the workpiece to the gas inlet is set at 450 mm.

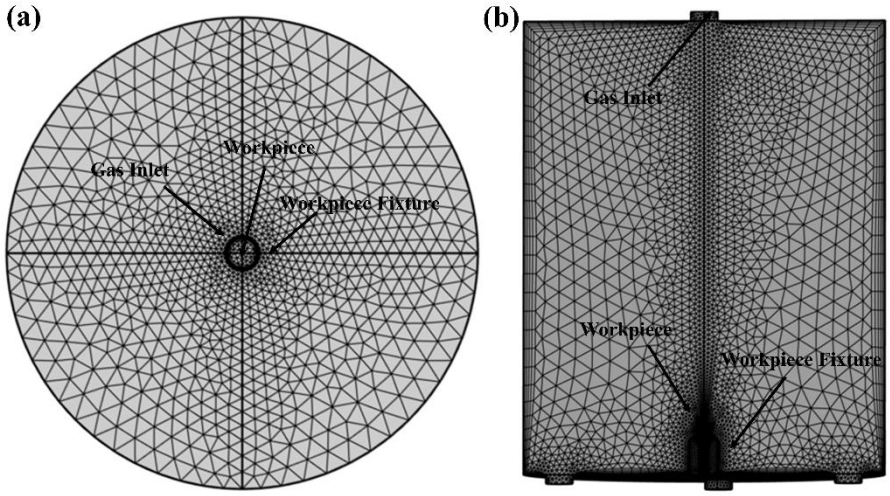

Figure 4.3 Mesh configuration for simulation: (a) Overall mesh layout and (b) Close-up around gas inlet, workpiece, and fixture.

Table 4.3 Geometric parameters of the simulation model.

	Size(mm)	Maximum element size(mm)	Minimum element size(mm)	Maximum element growth rate	Curvature factor
Ion Source	15x10	5.2	0.08	1.05	0.2
Workpiece	3x50	0.6		1.05	0.2
Fixture	15x40	3		1.05	0.2

4.4 Simulation results and analysis

4.4.1 Simulation of magnetic field distribution

The magnetic flux density distribution, as generated by the workpiece fixture with a flux of 400mT, is presented in Figure 4.4. This figure shows the direction of the magnetic vector and reveals a symmetrical distribution about the reactor's z-axis. The magnetic field created by the workpiece fixture forms a parabolic shape along the central axis, with the magnetic vector intersecting at this central point. This configuration influences the behaviour of reactive species within the reactor, significantly impacting the deposition process. The study explores various magnetic field intensities, including 0mT, 200mT, and 400mT, in 200mT intervals, providing a comprehensive view of the field's impact on deposition.

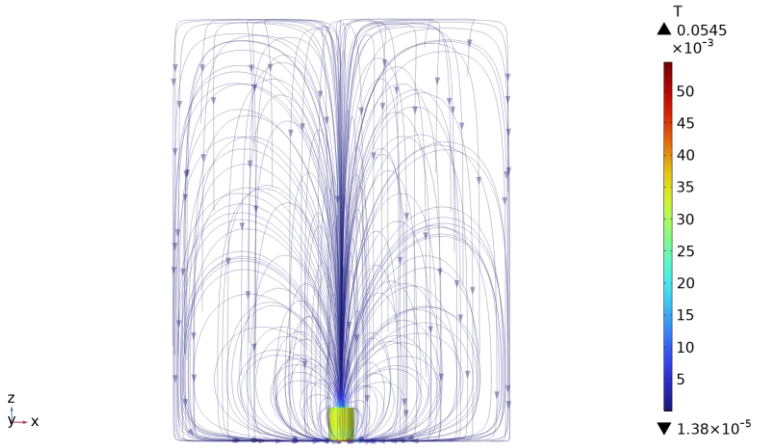

Figure 4.4 Simulation Results for Magnetic Flux Density at 400mT.

4.4.2 Investigation of ion movement under magnetic influence

Figure 4.5 shows the simulation of ion movements within a magnetic field. The ions follow trajectories along the magnetic vector due to the Lorentz force. According to the COMSOL software simulation (version 6.1), ion velocities can reach up to 200m/s. The Lorentz force generated by the magnetic field concentrates particle movements towards the central axis of the reactor. Introducing a magnetic field during electrochemical deposition has been shown to enhance the velocity of ion motion, thereby improving the HFCVD deposition rate on the workpiece surface. The Lorentz force of the magnetic field also plays a crucial role in directing ions towards the centre of the workpiece.

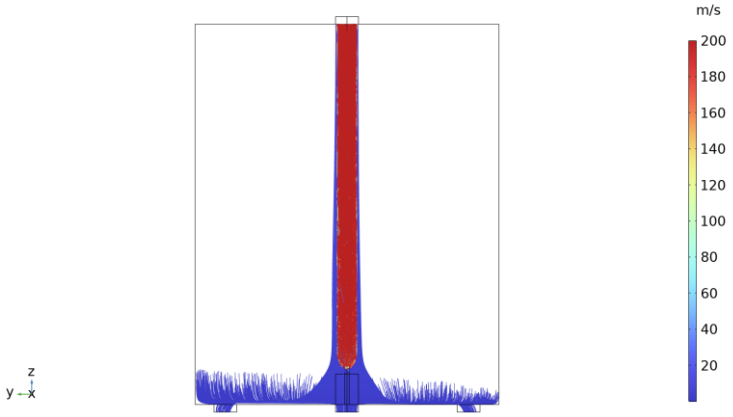

Figure 4.5 Simulation of ion motion in a magnetic field generated by the ring magnet inside workpiece fixture.

4.4.3 Evaluation of magnetic field impacts on deposition efficiency

This section discusses the impact of magnetic fields on ion motion and deposition during the HFCVD process. Specifically, it examines how varying magnetic field intensities affect ion behaviour, deposition efficiency, and quality.

The analysis commences with a simulation that illustrates the distribution of ion number density within a 400mT magnetic field, as shown in Figure 4.6(a). The simulation demonstrates that the magnetic field confines ions to the central axis of the workpiece, resulting in a more directed and effective deposition process. Additionally, the study compares ion deposition number density distributions under different magnetic field intensities, as depicted in Figure 4.6(b). The deposition patterns differ significantly between the absence and presence of a magnetic field. Without a magnetic field, the deposition is uniform but occurs at a lower rate. The simulation in Figure 4.6(c) illustrates the ion deposition density on the workpiece surface in the absence of a magnetic field. However, under magnetic influence, the ion deposition density increases, with a concentration at the bottom of the workpiece, as shown in Figure 4.6(d). In Figure 4.6(e), the trend intensifies at 400mT, where the deposition rate is higher and more uniform.

The HFCVD process involves the thermal decomposition of methane and hydrogen gases, which leads to the formation of reactive species such as radicals and ions. These species are crucial for depositing diamond films on the workpiece. The simulations show that the magnetic field, generated by SmCo permanent magnets placed beneath the tungsten filament, has a significant impact on reactive species. At a magnetic field strength of 400mT, the behaviour and distribution of these species, particularly methyl radicals and atomic hydrogen ions, are altered. This alteration may result in a higher concentration of reactive species in the vicinity of the cutting tool, potentially affecting the growth rate and quality of the diamond films.

The simulations confirm the hypothesis that the magnetic field modifies the distribution of reactive species around the workpiece. A magnetic field in operation produces a more uniform and concentrated distribution of the gas mixture, promoting

consistent and controlled diamond growth. The magnetic field's effect is crucial in restricting the dispersion of reactive species from the workpiece, reducing the possibility of growth defects in the diamond film. The magnetic field facilitates the concentration of methane and hydrogen radicals and ions, resulting in increased interaction between these radicals and the substrate. This interaction is crucial for an efficient diamond growth process since it affects the formation and quality of the diamond films.

The analysis reveals the complex relationship between magnetic field strength, ion behaviour, and deposition efficiency in diamond film growth using HFCVD. It highlights the potential of magnetic fields in optimising this process.

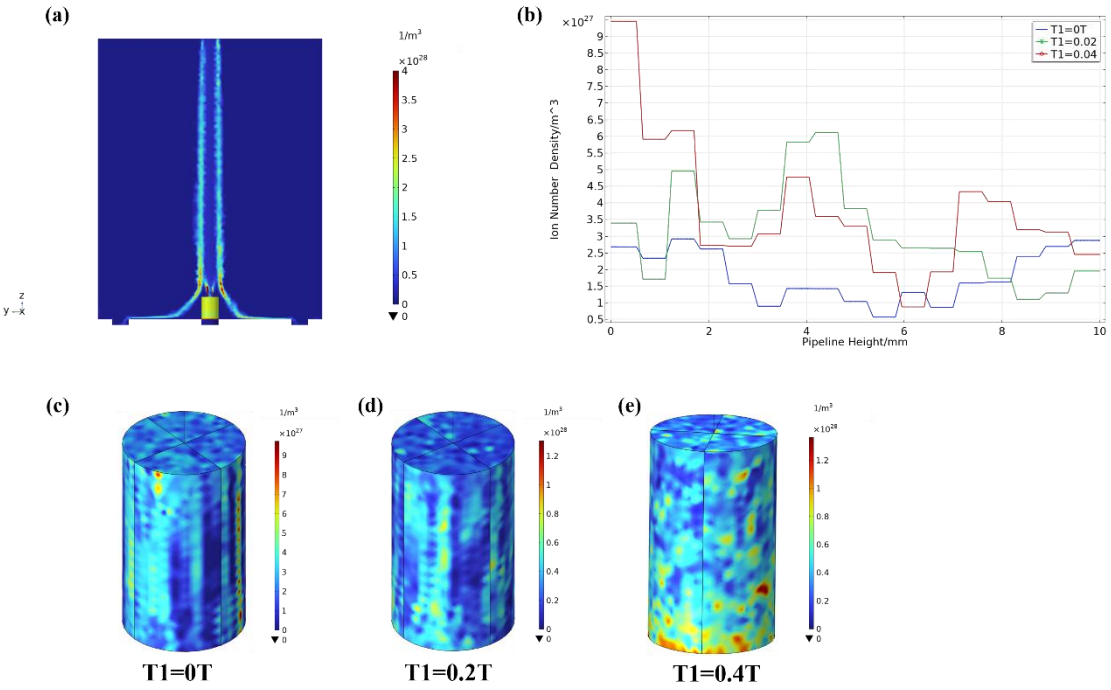

Figure 4.6 Ion motion and deposition simulations: (a) number density distribution of ions in the field for a 400mT magnetic flux; (b) ion deposition number density under different magnetic field intensities; (c) number density distribution of free ion deposition.

4.4.4 Analysis of the impact of temperature distribution on the process of deposition.

During the process of HFCVD, the movement of ions on the surface of the workpiece within a magnetic field generates Joule heat, which in turn elevates the temperature of the workpiece surface. To simulate the field and workpiece temperature under various magnetic flux intensities, COMSOL's solid heat transfer and multi-physical field coupling modules were used. Figure 4.7 illustrates the field temperature under different magnetic flux intensities. Figure 4.7(a) shows the field temperature at a magnetic flux of 400mT, indicating a noticeable temperature increase on the workpiece due to the magnetic field. Figure 4.7(b) illustrates temperature changes on the workpiece surface under various magnetic flux conditions. As per the simulation in Figure 4.7(b), in the absence of a magnetic field, the workpiece temperature is 828°C, with ions depositing freely in the field and generating less heat. Based on the ion deposition rate and workpiece surface temperature, it was determined that the optimal temperature for the workpiece surface is 858°C when the magnetic flux is 400mT. This temperature minimizes Joule heat generation on the workpiece surface, resulting in reduced thermal stress, a good ion deposition rate, and uniform ion deposition on the workpiece surface.

Regarding material characteristics, the quality of the diamond film is affected by the temperature of the workpiece surface. This, in turn, affects the structural properties of the film, including the diamond phase content and grain size. To ensure high-quality diamond film, it is crucial to maintain a balance between the ion deposition rate and the workpiece surface temperature. This balance can be achieved by finely adjusting the magnetic field intensity. The simulation results show that temperatures of 830°C and 858°C were observed at magnetic flux densities of 0T and 0.04T,

respectively. Although the temperature of 858°C is slightly higher than the ideal production range of 800-850°C for MCD, the use of a 0.04T magnetic field improves ion behaviour. The magnetic field directs ions to spread evenly across the workpiece surface, reducing the possibility of localized overheating, which is a common cause of thermal stress. This condition results in an optimal ion deposition rate and a more uniform ion distribution on the workpiece surface, contributing to a better quality diamond film. The study deliberately selected 0.04T to investigate the potential use of magnetic fields in influencing the growth of MCD film.

In simulations of HFCVD, the magnetic field system produced by permanent SmCo magnets plays a crucial role in raising the temperature of the workpiece. The magnetic field, which exerts a strength of 400mT at the surface, originates from SmCo circular magnets housed within a graphite holder, with the tungsten carbide tool centrally situated. The temperature elevation in the workpiece results from enhanced heat transfer processes between the filament and the tool, facilitated by the magnetic field. The magnetic field induces a magnetic force that causes charged particles and molecules in the surrounding gas mixture to move. This movement leads to increased collisions with the workpiece, enhancing heat transfer from the filament. Additionally, the magnetic field affects the temperature of electrons in the gas mixture, further amplifying the heat transfer process. The magnetic force causes the electrons to move in circular orbits, increasing their kinetic energy and temperature. This rise in electron temperature results in increased heat transfer from the electrons to the workpiece. To verify the simulation results, we compared them with experimental data obtained from a thermocouple and a pyrometer, which showed satisfactory agreement between the simulated and measured temperature values. The magnetic field system exerts a dual influence on the deposition process, affecting both the film growth dynamics and

microstructural evolution. Firstly, it increases the temperature of the workpiece surface. Secondly, it exerts a Lorentz force on charged and polarized species, such as ions and radicals, directing their movement towards the workpiece surface. This movement is intended to improve the efficiency of the deposition process by promoting effective interactions with the substrate. The uniformity and quality of the diamond film are improved by the magnetic field's influence on the trajectories of the species, minimizing their random motion and leading to a more streamlined and focused deposition. The dynamics show that, in addition to thermal effects, the magnetic field significantly improves the performance of HFCVD.

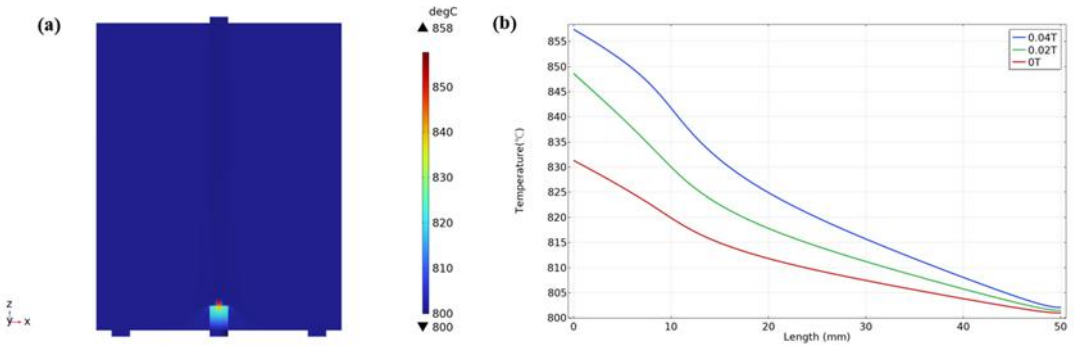

Figure 4.7 Temperature distribution simulation for different magnetic flux Intensities: (a) temperature distribution in the field for a 400mT magnetic flux; (b) temperature distribution curves for the field under different magnetic flux intensities.

4.4.5 Summary of the simulation test

The simulation of magnetic field-assisted HFCVD analysed the effects of different magnetic field intensities on-ion motion. The model used magnetic field intensities of 0mT, 200mT, and 400mT to investigate corresponding ion behaviour. The magnetic field guides ion motion through the Lorentz force, directing their paths towards the central axis of the workpiece. Increasing the probability of ion contact with the workpiece surface enhances the deposition rate. However, introducing a magnetic

field leads to additional complications, such as the generation of Joule heat on the workpiece in the field. This, in turn, produces thermal stress during ion deposition, which could potentially degrade the coating's performance. As the temperature rises, the thermal stress increases, causing a reduction in coating performance. However, an optimal balance was observed under different magnetic flux conditions. When the magnetic flux was set to 400mT, the temperature increase was moderate, and the ion deposition rate was reasonably high, resulting in a more uniform deposition. In summary, the simulation shows that the introduction of a magnetic field during HFCVD can enhance the ion deposition rate by directing ion paths. However, it is important to manage the thermal stress generated during this process to prevent degradation of coating performance. Based on the results, it is suggested that a magnetic flux of 400mT provides an optimal balance between these factors.

4.5 Experimental result and analysis

4.5.1 Initial stages of diamond film growth under magnetic field assistance

The initial stages of diamond film growth are pivotal in determining the quality and uniformity of the final coating. This phase is characterized by the nucleation of diamond crystals on the substrate, and the influence of magnetic field assistance during HFCVD on this process is profound. An examination of diamond coatings fabricated with a deposition time of 30 minutes reveals a significant difference in nucleation rates between magnetic field-assisted and traditional HFCVD methods.

As evidenced in Figure 4.8, the nucleation density in the magnetic field-assisted HFCVD process reaches 1.3×10^9 cm^{-2}, markedly higher than the 4.5×10^8 cm^{-2} observed in the standard HFCVD process. This substantial increase in nucleation rate underlines the effectiveness of magnetic field assistance in fostering diamond nuclei formation.

The enhanced nucleation rate can be attributed to several factors influenced by the magnetic field. Firstly, the presence of a magnetic field during the HFCVD process impacts the dissociation of hydrogen and methane into various hydrocarbon species, which are essential for diamond film formation. The magnetic field's influence on these reactant gases leads to a more homogeneous distribution of reactants, thereby increasing the number of active sites for diamond nucleation.

Additionally, the magnetic field enhances the dissociation of carbon species within the reaction zone, resulting in a higher concentration of reactive carbon-containing species. This increase is crucial for promoting diamond nucleation, as it provides a larger pool of necessary species for the formation of diamond crystals. Furthermore, the magnetic field also affects the thermodynamics of the reaction process. This impact is seen in the reduced activation energy required for the reaction, leading to an accelerated rate of diamond nuclei formation. The magnetic field effectively lowers the energy barrier for nucleation, thus facilitating a more efficient and robust diamond growth process.

The investigation into the nucleation stage of diamond film growth under magnetic field assistance in HFCVD demonstrates that this method significantly boosts the nucleation rate, thereby enhancing the overall quality and uniformity of diamond films. By promoting a higher density of diamond nuclei, magnetic field assistance creates a more favourable environment for the growth of high-quality diamond films. The resultant diamond films exhibit improved substrate surface coverage, characterized by uniformity and density, which are crucial attributes for high-performance diamond-coated tools and devices.

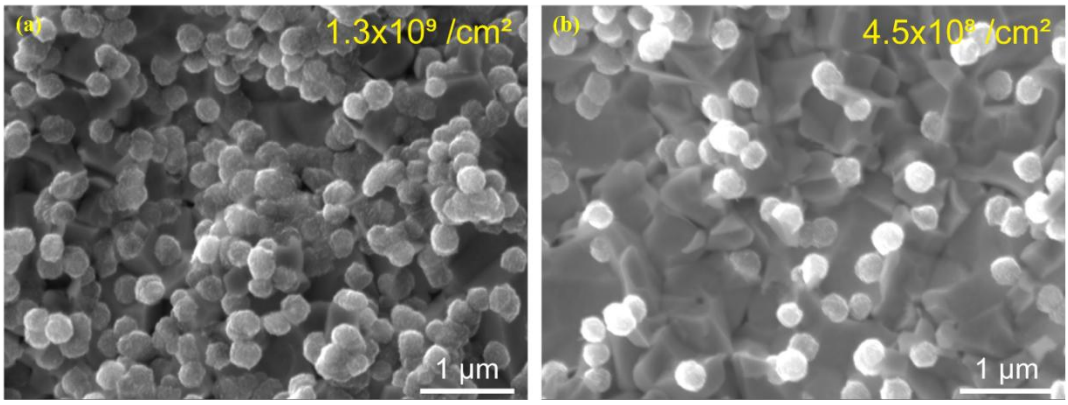

Figure 4.8 SEM micrographs of the diamond film after 30 minutes of deposition (a) M1 and (b) N1.

4.5.2 Coating thickness, surface morphology, and growth rate of the diamond film

Figure 4.9 displays cross-sectional profiles of diamond films produced by HFCVD of N1 and M1 with a deposition time of 6 hours. In the absence of an applied magnetic field, the coating thickness measured on the N1 tool was 15.14 μm. A coating thickness of 23.70 μm was achieved on the M1 tool under a 400 mT magnetic field, indicating a significant increase compared to the 15.14 μm thickness of the N1 tool. The results demonstrate that the diamond film on the M1 tool exhibited a higher growth rate compared to the N1 tool, given that both samples underwent deposition for an identical duration of 6 hours. This suggests that the addition of 400mT magnetic flux density enhances the coating growth rate. Additionally, the SEM results show that both films on the M1 and N1 tools exhibit columnar growth of multiple crystal grains. The diameter of the columnar grains on the M1 tool is noticeably larger than that of the N1 tool. This is due to a higher growth rate, which is caused by magnetic field assistance. As illustrated in Figure 4.9, the microstructural features suggest that the diamond film on the M1 tool possesses a larger grain size. Figure 4.10 displays the surface morphology of the diamond films on tools N1 and M1, along with a statistical analysis

of their grain sizes. SEM images of the films after 6 hours of deposition on N1 and M1 are presented in Figure 4.10(a) and Figure 4.10(b), respectively. The accompanying histograms in Figure 4.10(c) and Figure 4.10(d) show the distribution of grain sizes for M1 and N1, respectively. M1 has a mean grain size of 18.0 μm, ranging from 5.5 μm to a maximum of 25.8 μm, while N1 has a smaller mean grain size of 8.1 μm, ranging from 3.35 μm to 14.95 μm. The analysis indicates that the use of a magnetic field during the deposition process is associated with an increase in diamond grain size. This is supported by the larger grains observed on sample M1 compared to N1, as shown in Figure 4.10. The larger grains in M1 are due to the differential growth rates of crystals with different orientations, rather than low nucleation density, as opposed to the presence of intergranular gaps. The finding is in line with Van der Drift's evolutionary selection model (Van der Drift, 1967). The model explains that crystals with sharp corners protruding into the growth direction (110 oriented crystals) grow faster and eventually outgrow crystals with faces parallel to the substrate surface (100 oriented crystals). This growth rate difference causes gaps on the film surface because 110 oriented crystals grow faster than 100 oriented crystals (Wild et al., 1990). The magnetic field is significant because it promotes nucleation and influences crystal growth. Its use accelerates the growth of crystals with pointed corners more than flat ones, intensifying the evolutionary selection process. The microstructure is characterised by larger grains separated by gaps, which demonstrates the interaction between nucleation enhancement, crystal orientation, and the influence of the magnetic field on the formation of the diamond film microstructure. Figure 4.11 illustrates the trend in coating thickness and duration for tools M1 and N1. Tool M1 has a steeper gradient than tool N1, meaning it has a higher growth rate with nearly 45% more than that of tool N1 throughout the entire deposition of the diamond film. The use of a

magnetic field improves various aspects of the deposition process, potentially explaining the observed increase in growth rate. This improvement is due to increased gas transport, higher nucleation density, and better utilization of reactant gases, as demonstrated by COMSOL simulation.

Polydispersity index (PDI) was used to quantify dispersion of grain size distributions measured from SEM images. Grain sizes were obtained by image analysis of representative SEM micrographs, and the mean grain size (μ) and standard deviation (σ) were calculated from the measured grain size population. PDI was calculated using:

$$PDI = (\sigma / \mu)^2$$

Lower PDI values represent narrower grain size distributions and higher grain size uniformity. Higher PDI values represent broader grain size distributions and reduced grain size uniformity. PDI definition and calculation procedure are used in Chapter 5 for quantitative comparison across magnetic configurations and rotation speeds.

PDI values for the static magnetic field comparison remained similar between conditions, with M1 = 0.15 and N1 = 0.14, as shown in Table 4.4. The small difference indicates comparable dispersion of grain size distribution under both conditions. The static magnetic field therefore correlates more strongly with changes in growth kinetics, such as enhanced nucleation and increased growth rate, rather than changes in grain size uniformity.

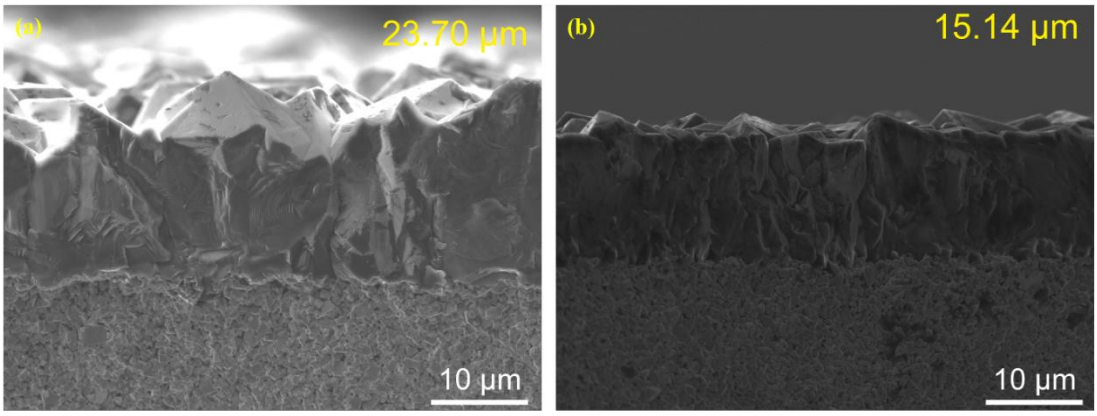

Figure 4.9 SEM of cross-sectional profiles of the diamond film coating with 6 hours deposition time (a) M1 and (b) N1.

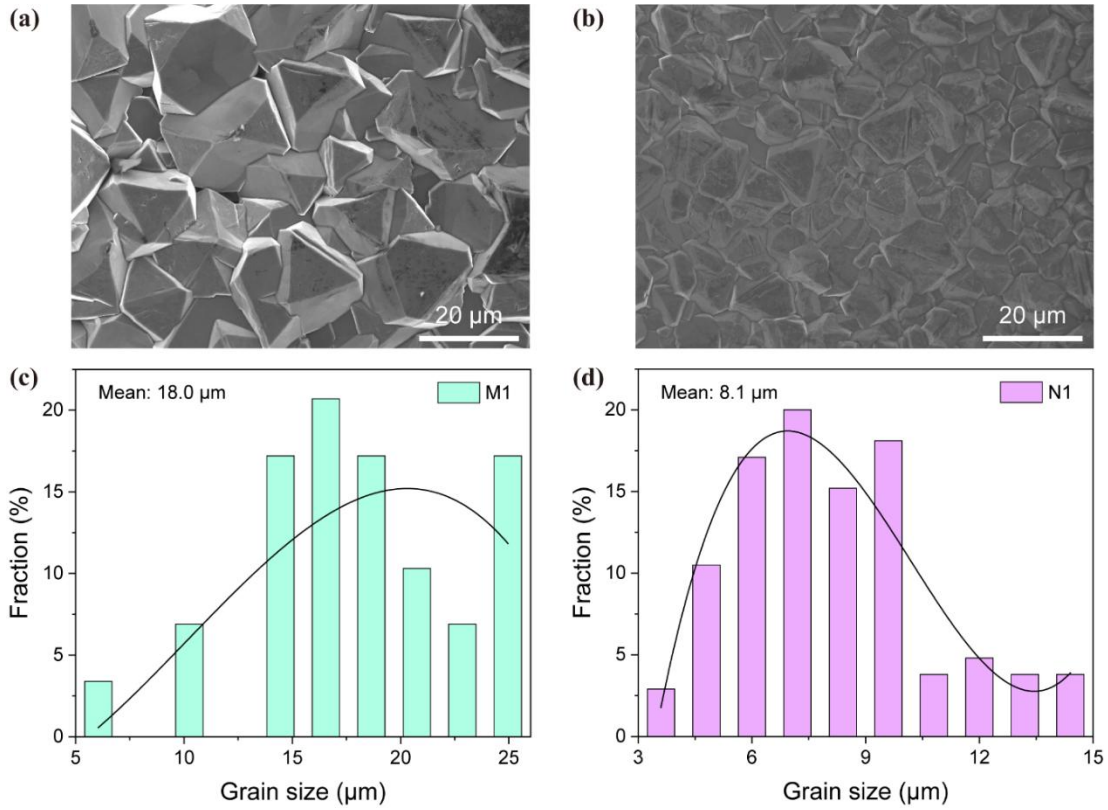

Figure 4.10 (a) Surface morphology of sample M1, (b) Surface morphology of sample N1, (c) Grain size distribution histogram for sample M1 and (d) Grain size distribution histogram for sample N1.

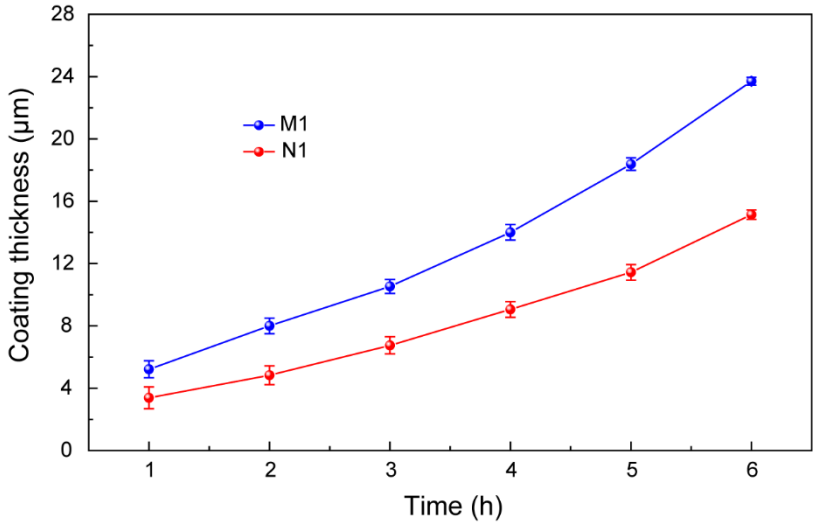

Figure 4.11 Diamond film coating thickness corresponding to the deposition duration.

Table 4.4 PDI for grain size distribution of M1 and N1.

Samples	PDI
M1	0.15
N1	0.14

4.5.3 Raman analysis of diamond films

The Raman spectrum with a wavelength of 532nm characterises the phases of the diamond films fabricated with deposition times of 30 minutes and 6 hours, as shown in Figure 4.12. During the 30-minute nucleation stage, M1 exhibited more intense diamond and G peaks than N1. A higher intensity of the Diamond peak indicates an increase in crystalline diamond content in M1, implying effective nucleation with magnetic field assistance. The M1 sample exhibits a pronounced G peak, indicating the presence of sp2-bonded carbon at grain boundaries. This peak is associated with a higher nucleation density, as observed by SEM analysis. The higher relative intensity observed in the G peak during the nucleation phase reflects the microstructural characteristics of initial growth, which includes a denser population of nucleation sites

near grain boundaries. During the 6-hour deposition, M1 exhibited a peak position of 1333.42 cm-1 and a full width at half maximum (FWHM) of 12.64 cm-1, while N1 exhibited a peak position of 1334.69 cm-1 and an FWHM of 17.21 cm. These findings indicate that the M1 sample had a narrower diamond peak, suggesting a more evenly distributed diamond phase and less structural disorder. As the deposition progresses to 6 hours, both M1 and N1 samples show a dominant peak indicating the sp3 bonded diamond phase. This suggests that the films evolve towards a similar crystalline structure with less difference in sp2 content. The shift in Raman peak positions from 1333.42 cm-1 in M1 to 1334.69 cm-1 in N1, as well as the corresponding FWHM values, can be attributed to changes in the films' internal stress and crystallinity. A peak position closer to the standard 1332 cm-1 and a smaller full width at half maximum (FWHM) in M1 suggest a reduction in internal stress and an improvement in crystalline order due to the magnetic field. The slight deviation in N1 suggests higher internal stress and a lower degree of crystalline order, possibly due to less controlled growth conditions in the absence of magnetic field assistance. The structural properties and quality of the resulting diamond films are significantly influenced by magnetic fields, and it is important to note the objective role of magnetic fields in this process.

In addition, Raman spectroscopy analysis offers a comprehensive view of the internal stress variations in diamond films. The M1 sample's peak position is closer to the ideal 1332 cm-1 than the N1 sample, indicating lower internal stress. The peak shift and FWHM directly reflect the stress state within the diamond lattice. The reduced FWHM in the M1 sample is consistent with a more uniform crystal structure and minimized stress-induced distortions. The magnetic field plays a crucial role in influencing the concentration and distribution of reactive gases on the substrate surface, resulting in enhanced gas transport, more efficient nucleation, and ultimately a

diamond film with improved crystallinity over time. By modifying the concentration and distribution of reactive gases on the substrate surface, the magnetic field can impact the deposition process. The Lorentz forces induced on charged particles by the magnetic field cause them to move in a circular motion, enhancing gas transport to the substrate. This can lead to more efficient deposition and nucleation, resulting in a diamond film with improved crystallinity.

After the initial nucleation stage, the M1 sample shows increased intensity in the diamond and G peaks, indicating a higher initial nucleation density. The films undergo a significant transformation during the extended 6-hour deposition period. The Raman spectra in Figure 12b show the transition to a predominantly sp3-bonded diamond phase after 6 hours. This phase is characterized by a sharper and more intense diamond peak, which is a hallmark of high-quality diamond films. The M1 sample demonstrates the beneficial effects of magnetic field assistance, not only in increasing nucleation density but also in promoting the growth of well-ordered diamond crystals with minimal internal stress. The transition to a narrower FWHM and peak orientation closer to the ideal 1332 cm-1 is evidence of this.

This transformation exemplifies the primary goal of our low-methane deposition process: to maximize the sp3 bonded carbon content, which is characteristic of pure diamond. The quality of diamond films is determined by the crystallinity and order within the sp3 diamond lattice, rather than the sp2 content observed during the initial nucleation phase. Therefore, while the G-peak intensity is an early indicator of nucleation density, the final assessment of diamond film quality is based on the characterization of the sp3 content, as revealed by Raman spectral features throughout the entire deposition process. The results suggest that magnetic field-assisted HFCVD is a feasible method for producing high-quality MCD films. The magnetic field plays

a crucial role in optimizing the distribution of reactive gases and enhancing the overall crystallization process.

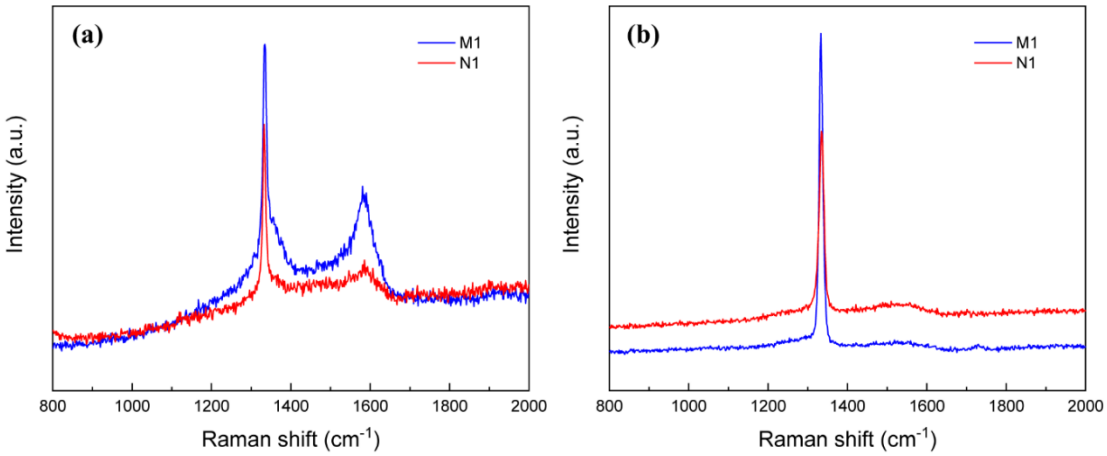

Figure 4.12 Raman intensity images of N1 and M1, (a) Raman spectra of diamond films after 30 minutes deposition and (b) Standard Raman spectra of diamond films after 6 hours deposition.

4.5.4 X-ray diffraction analysis of diamond films

The structural properties of the diamond films produced via HFCVD, with (M1) and without (N1) the assistance of a magnetic field, have been characterised analysed through X-ray diffraction (XRD), as depicted in Figure 4.13. The XRD patterns elucidate the crystalline nature of the films, with diffraction peaks corresponding to the diamond planes at (111), (220), and (311) being evident in both samples, as presented in **Error! Reference source not found.**. M1 exhibited diffraction peaks at 2-theta angles of 43.9919°, 75.4425°, and 91.612° for these respective planes, accompanied by Full Width at Half Maximum (FWHM) values of 0.4505°, 0.4886°, and 0.6731°, which signify well-defined crystallinity. In a similar manner, N1 displayed analogous peak positions; however, it demonstrated slightly altered FWHM values, implying slight variations in crystallite size and strain between the samples.

Notably, while the relative intensities of the (111) plane are normalized to 100% for both samples, the relative intensities for the (220) plane reveal a discernible variation: 20.98% for M1 in contrast to 24.23% for N1. This approximately 15% disparity underscores subtle distinctions in crystal texture, potentially reflecting the differential impact of magnetic field assistance on the growth dynamics. Such variations, although not significantly pronounced, offer insights into the role of the magnetic field in modulating the crystalline structures of the diamond films. The elevated peak heights observed for M1 in comparison to N1 further substantiate the superior crystallinity of the film subjected to magnetic field assistance. This finding is corroborated by Raman spectroscopy results, which demonstrate a narrower D-peak and a higher Raman signal efficiency factor for M1 relative to N1, indicating that the magnetic field not only augments crystallinity but also fosters more ordered crystal growth, culminating in a denser and more crystalline diamond film. The evidence posits that magnetic field assistance during the deposition process potentially enhances film crystallinity, a conclusion that is substantiated by both XRD and Raman analyses.

In summary, the synergistic application of XRD and Raman analysis underscores the successful deposition of high-quality crystalline diamond films, with the magnetic field playing a crucial role in enhancing crystalline quality, as evidenced by elevated peak heights and corroborated by Raman spectroscopy. Although the comparative XRD data does not reveal a significant alteration in grain orientation preference between the two samples, the comprehensive analysis accentuates the advantageous effects of magnetic field assistance on diamond film deposition.

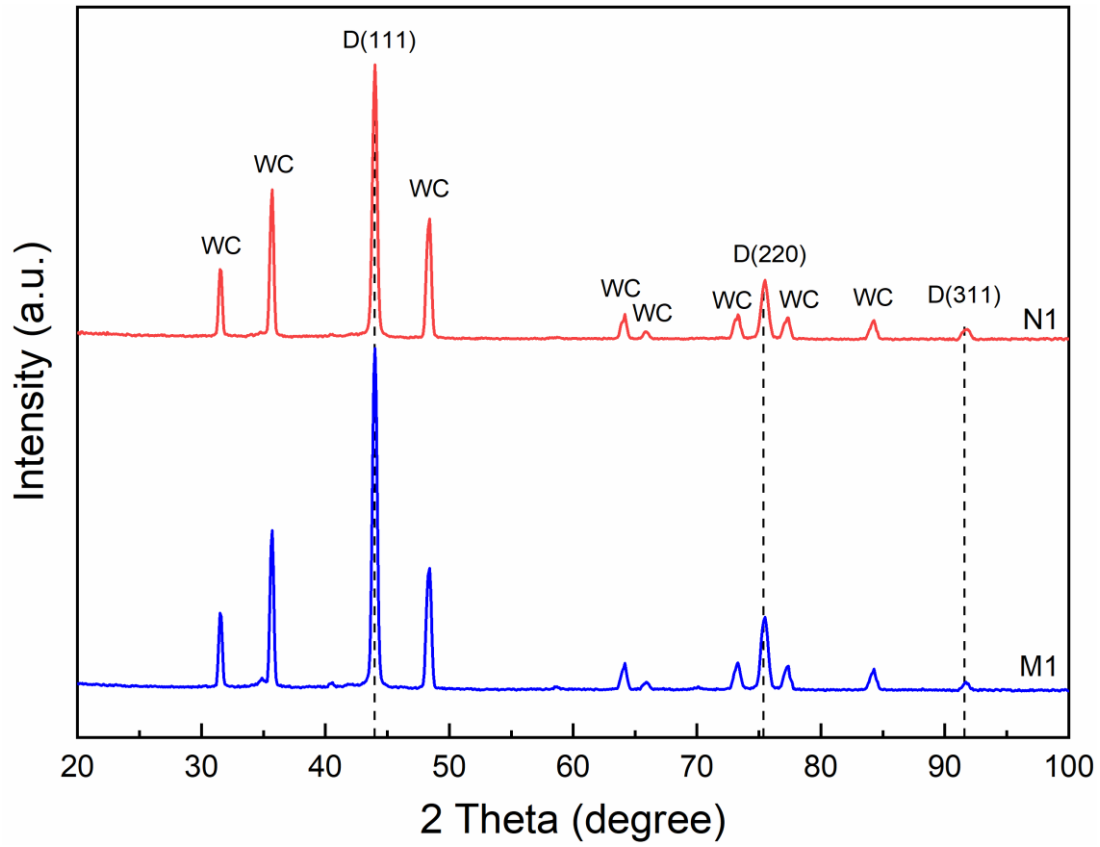

Figure 4.13 Comparison of X-ray diffraction patterns for M1 and N1 samples.

Table 4.5 X-ray diffraction patterns results of M1 and N1 samples.

Samples	2-theta(deg)	FWHM (deg)	Int.I(cps deg)	Rel. int. I
M1	43.9919	0.4505	2330.87	100
	75.4425	0.4886	489.06	20.98
	91.612	0.6731	272.18	11.68
N1	44.0415	0.4369	1904.68	100
	75.4169	0.5586	461.59	24.23
	91.6793	0.6595	242.46	12.73

4.6 Theoretical explanation of magnetic field effects on diamond film growth

The use of a magnetic field during HFCVD has been shown to significantly improve the quality and properties of diamond films when using low methane

concentrations. This section will explain how the magnetic field affects both grain size and coating thickness, with a focus on distinguishing between the two.

4.6.1 Influence on grain size

The size of diamond grains in films fabricated via HFCVD largely depends on the methane concentration in the gas mixture. Typically, a lower methane concentration results in a reduced nucleation density, which in turn leads to the formation of larger diamond grains. Conversely, a higher methane concentration increases nucleation density, resulting in finer grains. During the HFCVD process, gas molecules are exposed to temperatures exceeding 1800°C near the hot filament, where they gain sufficient energy to dissociate into radicals and ions.

When considering the impact of a magnetic field on grain size, particularly under low methane concentration conditions, it is important to integrate both experimental observations and theoretical principles. Lower methane concentrations are traditionally associated with slower growth rates and smaller grain sizes due to the limited supply of carbon-containing species necessary for deposition. The introduction of a magnetic field into the HFCVD chamber, especially under low methane concentration conditions, helps to mitigate these limitations. The magnetic field effectively guides and controls the trajectory of ion and radical particles, reducing the loss of kinetic energy typically observed due to frequent collisions. In a standard HFCVD setup, ions and radicals move erratically in various directions, losing kinetic energy through frequent collisions. However, with the application of a magnetic field, the movements of these particles are influenced by the magnetic forces, leading to more controlled trajectories and minimized energy loss.

The kinetic energy of ions and radicals is transformed into thermal energy upon impacting the tool surface, resulting in an increase in the tool's temperature. This

elevated temperature enhances the diffusion rate, as described by the Einstein-Smoluchowski equation ($D = \mu q k_B T/q$), where D is the diffusion rate, μ is the mobility, q is the charge, k_B is Boltzmann's constant, and T is the temperature. A higher substrate temperature, therefore, leads to an accelerated diamond film growth rate, even under low methane concentration conditions. This is further corroborated by the Arrhenius equation, which emphasizes the exponential relationship between reaction rate and temperature. Under these optimized conditions, larger diamond grains are more likely to form, despite the low methane availability. The increased diffusion rate allows adatoms on the substrate surface to move more dynamically and coalesce more effectively, facilitating the growth of larger grains.

In summary, the integration of a magnetic field into the HFCVD process substantially enhances diamond film growth. This advancement is achieved through improved deposition efficiency and elevated substrate temperatures, fostering the development of larger diamond grains in spite of the inherent challenges posed by low methane concentrations.

4.6.2 Impact on coating thickness

The influence of a magnetic field on the coating thickness of diamond films during HFCVD can be explored by integrating both experimental data and theoretical principles. In conventional HFCVD, ions and radicals exhibit rapid, multidirectional movements, leading to frequent collisions and consequential loss of kinetic energy. However, the introduction of a magnetic field inside the chamber significantly alters this dynamic. With the magnetic field in place, the trajectories of ions and radicals are steered by the magnetic forces, resulting in more controlled movements and reduced kinetic energy loss. When these particles collide with the tool surface, their kinetic energy is converted into thermal energy. This conversion causes an increase in the tool's

temperature, which in turn enhances the diffusion rate. The relationship between the diffusion rate and temperature is quantified by the Einstein-Smoluchowski equation ($D = \mu q k_B T/q$), indicating that the diffusion rate is directly proportional to the temperature. As the substrate temperature rises, so does the diamond film growth rate, despite potentially low methane concentrations. This effect is also emphasized by the Arrhenius equation, which illustrates the exponential dependency of reaction rates on temperature, reinforcing the significance of higher substrate temperatures in facilitating diamond growth.

Additionally, Fick's first law of diffusion ($J = -D\nabla C$) plays a crucial role in this process. This law states that the diffusion flux J is directly proportional to the concentration gradient ∇C and the diffusion coefficient D. Since the diffusion coefficient is temperature-dependent, variations in temperature will influence the diffusion flux. An increase in diffusion flux corresponds to a heightened diamond film growth rate, leading to a thicker coating. The temperature increase under magnetic field assistance is corroborated by both the thermocouple inside the tool top tip and the Pyrometer outside the chamber observation window, aligning with the observed trends in simulation results.

To summarize, the incorporation of a magnetic field in HFCVD significantly influences diamond film growth and coating thickness. Enhanced deposition efficiency combined with raised substrate temperatures leads to a more robust growth rate. This, in turn, results in the formation of thicker diamond film coatings, overcoming the limitations imposed by low methane concentrations.

4.7 Summary

This section of the thesis has delved into the multifaceted impacts of incorporating a magnetic field in the HFCVD process for diamond film growth. The

exploration encompassed various aspects, from the initial stages of diamond film nucleation to the final characteristics of the diamond film, including grain size, coating thickness, and crystal structure.

Key findings from this investigation are summarized as follows:

The application of a magnetic field during HFCVD significantly increases the nucleation rate of diamond films. This enhancement is attributed to the magnetic field's influence on reactant gas distribution and dissociation dynamics, leading to a more homogeneous distribution of active sites for diamond nucleation. The magnetic field influence extends to the growth rate and morphology of diamond films. Films grown under magnetic field conditions exhibit increased thickness and a change in grain size, indicating that the magnetic field assists in accelerating the deposition process and influencing crystal growth patterns. Raman and X-ray diffraction analyses reveal that diamond films grown with magnetic field assistance have improved crystallinity and phase purity. A more dominant (111) crystal orientation, indicative of high-quality diamond films, is observed in films grown under magnetic field conditions.

The benefits observed in the diamond film characteristics under magnetic field conditions are supported by theoretical explanations. These include the influence of the magnetic field on-ion and radical particle behaviour, enhancing thermal energy transfer and improving reaction kinetics, which are critical for high-quality diamond film growth. The introduction of a magnetic field in HFCVD alters the thermal dynamics of the process. Enhanced substrate temperatures, resulting from controlled particle movements and improved heat transfer, contribute to the observed improvements in diamond film growth.

In conclusion, the research underscores the significant potential of magnetic field assistance in the HFCVD process. This technique not only enhances the nucleation

rate and growth of diamond films but also contributes to the improved structural and morphological qualities of the films. These findings cover the way for further optimization of diamond film deposition processes, with potential applications in various industrial and technological fields.

Chapter 5 Static and rotational magnetic assistance in HFCVD

5.1 Introduction

Diamond films have garnered significant research interest due to their exceptional properties, including high thermal conductivity, extreme hardness, and excellent electrical insulation. These unique characteristics offer a wide range of potential applications across various fields, such as electronics, optics, wear-resistant coatings, and the biomedical sector. The potential of diamond films to drive advancements in these industries is considerable (Handschuh-Wang et al., 2021; May, 2000).

One of the most notable properties of diamond films is their remarkably high thermal conductivity, exceeding 2000 W/mK, which makes them highly efficient in dissipating heat (Umezawa et al., 2012; Yang et al., 2019). Effective heat dissipation is crucial for the optimal functioning of high-power electronic devices, as it prevents overheating and ensures reliable performance. Diamond film synthesis can be achieved through several techniques, including HFCVD, microwave plasma chemical vapor deposition (MPCVD), and radio-frequency chemical vapor deposition (RFCVD) (Schwander & Partes, 2011). Among these methods, HFCVD stands out for its cost-effectiveness, scalability, and ability to deposit diamond films on large substrates. However, achieving uniform growth remains a significant challenge. The uniformity of diamond film growth is related to the performance and reliability of devices that utilize these films. Variations in uniformity can lead to inconsistent properties, which may adversely affect device performance.

The quality and uniformity of diamond films are also critical for semiconductor manufacturing, particularly in Chemical Mechanical Polishing (CMP). CMP is a key process for planarizing wafer surfaces in semiconductor fabrication. Due to their

hardness and thermal properties, diamond films are promising materials for CMP, either as the material being polished or as a component of the polishing pad (Kim & Kang, 2011; Thomas et al., 2014). However, the effectiveness of diamond in CMP applications is heavily dependent on the uniformity and quality of the films. Non-uniform films can result in inconsistent polishing rates and suboptimal outcomes, underscoring the importance of achieving uniform growth, particularly for CMP applications (Kumar Mallik et al., 2016).

To address the challenges associated with uniform growth, researchers have explored the use of magnetic fields during the deposition process. Magnetic fields can significantly influence the chemical species within the deposition chamber, thereby affecting both the growth rate and the quality of diamond films. Previous studies have demonstrated that magnetic fields can enhance the quality of diamond films, improving attributes such as crystallinity, uniformity, and surface morphology (Kwok et al., 2024; Li et al., 2017; Little et al., 2005; Long et al., 2015; Wang et al., 2016). For example, the introduction of a periodic magnetic field (PMF) in the HFCVD process has been shown to increase the growth rate and improve the crystal quality of diamond films. This enhancement is achieved by increasing the collision probability of reactive gas molecules with electrons and polarized hydrocarbon species, facilitating more efficient ionization and film growth. Furthermore, using a static periodic magnetic field has revealed that optimizing the magnetic flux density within the deposition chamber can lead to improved film uniformity and quality.

However, most studies have focused on periodically varying magnetic fields rather than permanent magnets. Due to the high temperatures within the deposition chamber, magnetic field systems are typically positioned outside the chamber, resulting in a weaker magnetic flux density, ranging from 1 mT to 11 mT, in the reaction zone

inside the chamber. This limitation highlights the need to investigate both static magnetic field orientations and the rotation of the magnetic field system. Despite this, a comprehensive study on the distinct effects of various static magnetic field orientations on the growth of diamond films in HFCVD has yet to be conducted. In addition to static magnetic fields, researchers have also explored the effects of magnetic field rotation on diamond film growth, aiming to enhance uniformity during the deposition process. Rotating the magnetic field may alter the exposure of the substrate to reactive species, potentially improving the uniformity of film growth, which is crucial for the functionality of diamond-based devices. However, the combined influence of static magnetic field orientations and the rotation of the magnetic field system on diamond film growth in HFCVD has not been extensively explored.

This study seeks to address this research gap by examining the impact of different static magnetic field orientations and the rotation of the magnetic field system on the growth of diamond films in HFCVD. The research combines experimental work with FEM simulations to analyse these effects. The goal is to enhance the fundamental understanding of how magnetic fields influence the growth dynamics of diamond films. The findings from this study have the potential to significantly improve the HFCVD process, leading to more efficient methods for producing high-quality diamond films with enhanced growth uniformity. These advancements are crucial for expanding the use of diamond films in various industries, particularly in thermal management systems, and will contribute to the development of advanced techniques for creating diamond films and broadening the potential applications of HFCVD.

5.2 Materials & methods

5.2.1 The design and functionality of the magnetic field assistance

The magnetic field assistance system is integrated within the HFCVD machine, and when used in conjunction with a magnetic field, the process is referred to as the Magnetic-Assisted Hot Filament Chemical Vapor Deposition (MA-HFCVD) process, as illustrated in Figure 5.1. The implementation of the magnetic field assistance system utilizes Sm2Co17 permanent magnets, characterized by a magnetic flux density of 400 mT. An essential aspect of this system is its capacity to alter the magnetic flux density and orientation, which can be achieved by either substituting the magnets or adjusting their placement. These modifications play a crucial role in investigating the impact of magnetic fields on the deposition process. Furthermore, the system integrates a rotational mechanism to explore how the orientation of a magnetic field impacts the properties of chemical species. This specific attribute is crucial for comprehending the effect of magnetic field orientation on the growth rate and characteristics of diamond films. The magnets are securely positioned within the system and have the ability to rotate on their axis to attain the desired magnetic field orientation.

The system also includes a rotational mechanism designed to explore how the orientation of the magnetic field influences the properties of the chemical species involved in the deposition process. This capability is essential for understanding how different magnetic field orientations impact the growth rate and characteristics of diamond films. The magnets are securely mounted within the system and are capable of rotating on their axis to achieve the desired magnetic field orientation. The alignment of the magnetic field is maintained using clamps and a casing that allows for rotational motion. Adjustable screws facilitate the initial placement of the magnets, and once the

desired positioning is set, the rotational mechanism can be engaged to adjust the magnetic field alignment during the deposition process.

Managing the thermal challenges inherent in the HFCVD process is critical due to the high temperatures involved. The filament can reach temperatures of up to 2,300℃, while the working table may approach 800℃. These extreme conditions pose a risk of overheating the magnets beyond their Curie point, which could lead to significant changes in their magnetic properties and potential demagnetization. To mitigate this risk, the system includes a protective insulating layer that shields the magnets from excessive heat. Additionally, the magnets are encased in quartz, a material known for its high thermal resistance.

Beyond static magnetic fields, the system is designed to investigate a range of rotational speeds, from 0 RPM to 2 RPM. This feature allows for an in-depth study of the interaction between magnetic fields and the diamond film deposition process under various dynamic conditions. Furthermore, the system supports multiple magnetic alignments, such as North-North (NN), South-South (SS), and South-North (SN), enabling a comprehensive analysis of how these configurations affect the deposition process.

In summary, the MA-HFCVD setup provides a robust platform for investigating the impact of magnetic fields on the deposition of diamond films. It allows for precise control over the magnetic field strength and positioning, effectively addressing the thermal management challenges of the HFCVD process. The system's capability to operate at different rotational speeds and magnetic alignments offers a unique opportunity to conduct an extensive study on the influence of magnetic field dynamics on diamond film deposition.

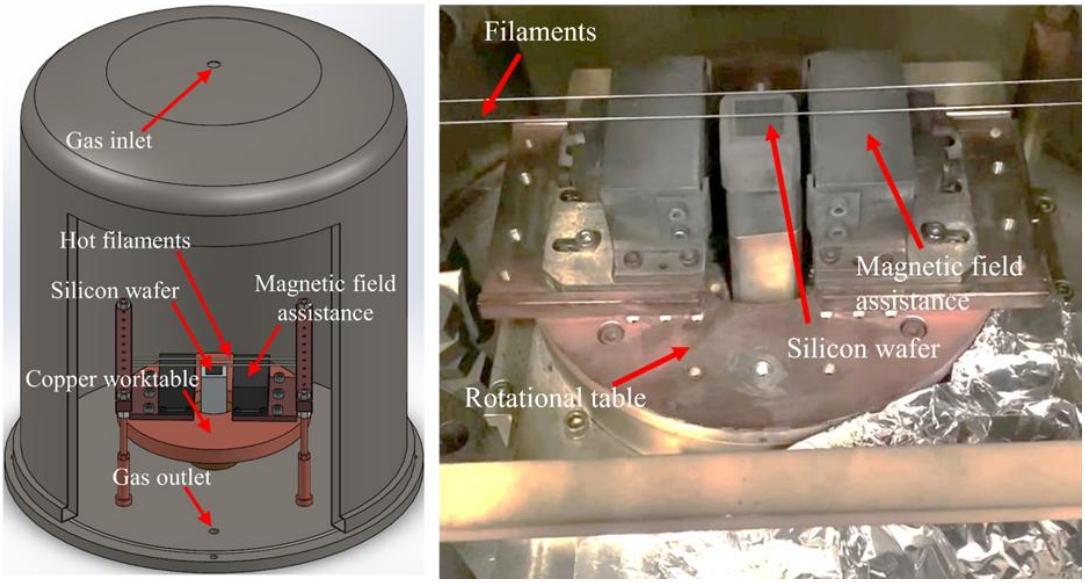

Figure 5.1 Schematic diagram of MA-HFCVD setup.

Table 5.1 Deposition parameters for diamond film used in MA-HFCVD.

Parameters	Deposition conditions
Power	3000
Number of filaments	2
Hydrogen content (sccm)	2000
Methane content (sccm)	40
Tool temperature (◦ C)	830
Filaments temperature (◦ C)	2300
Pressure (Pa)	1500
Deposition duration (h)	3

Table 5.2 Magnetic field system for different sample growths in MA-HFCVD.

Samples	Size (mm)	Magnetic field strength (mT)	Magnetic field direction	Rotational speed (rpm)
SS	20x20x0.5	400	South-South	0-2
SN	20x20x0.5	400	South-North	0-2
NMF	20x20x0.5	-	-	0-2

5.2.2 Diamond film deposition

Diamond films were deposited on silicon substrates following a 30-minute diamond seeding process to prepare the substrate surface for optimal diamond growth. The deposition process (Table 5.1) involved introducing a gaseous mixture of methane (CH_4) at a flow rate of 40 standard cubic centimeters per minute (sccm) and hydrogen (H_2) at a flow rate of 2000 sccm into the chamber. The experiments were conducted using the MA-HFCVD system, equipped with a magnetic system measuring 420x400 mm. The deposition setup featured a functional table with dimensions of 400x600 mm, designed to securely hold the silicon wafer substrates (20x20x0.5 mm) in a graphite holder, ensuring stability and minimizing disruptions during the deposition process. Two tantalum (Ta) filaments, each with a diameter of 0.6 mm, were positioned 5 mm above the substrate. Throughout the three-hour deposition process, a stable gas balance and an atmospheric pressure of 3000 Pa were consistently maintained.

5.2.3 Comprehensive characterization

Several characterization methods were employed in order to investigate the deposited diamond films. The utilization of Scanning Electron Microscopy (SEM) facilitated the examination of the surface topology of the diamond films, thereby offering detailed information regarding the sizes of the grains, their distribution, and the overall uniformity of the films. Raman Spectroscopy was employed to explore the vibrational states of the crystalline structure, thus aiding in the differentiation between the diamond's quality and other forms of carbon. In addition to these techniques, the thermal response time measurement method was introduced to analyse the thermal properties of the films by examining the temperature changes of the silicon wafer under controlled heating conditions. The combination of these tools provided a

comprehensive understanding of both the physical and thermal properties of the diamond films, thereby establishing a solid foundation for subsequent discussions.

The comprehension of the thermal properties of diamond films subsequent to their deposition is of utmost significance. These measurements provide valuable insights into the impact of magnetic assistance and rotational dynamics on the uniformity and quality of the film, which are linked to its heat distribution capabilities. This understanding is not solely of academic interest, but also carries significant implications for the practical application of these films, particularly in industries where effective dissipation of heat is imperative.

To carry out this investigation, a high-precision hot plate capable of adjusting to specific temperatures of 200°C was utilized. The selection of these particular temperature values was purposeful, with the aim of simulating various operational conditions and observing the corresponding thermal behaviour of the diamond films. For the purpose of the experiment, silicon wafers with diamond films, produced with different magnetic orientations and rotation speeds, were meticulously cleaned to ensure direct and uniform contact with the hot plate. On the uncoated side of each silicon wafer, five K-type thermocouples with high sensitivity were affixed. The central thermocouple was positioned at the geometrical centre of the wafer, while the remaining thermocouples were evenly distributed along the edges.

Subsequently, the side of the wafer coated with diamond was placed in direct contact with the hot plate, establishing a physical connection between the two entities as shown in Figure 5.2. As the temperature gradually increased to a maximum of 200°C, the thermocouples diligently recorded and analysed the resulting measurements. Adequate time was allocated for the hot plate to reach a state of thermal equilibrium, thus ensuring consistent and reliable data acquisition. Each and every wafer that has

undergone the rigorous process of HFCVD, involving a wide range of magnetic orientations (NMF, SS, SN) and rotation speeds (0 rpm, 1 rpm, and 2 rpm), has been subjected to this testing procedure. This thorough and comprehensive approach played a paramount role in identifying any potential variations in thermal conductivity that may arise from different deposition parameters. The data collected and organized from these extensive tests serves as the foundational element, shedding light on the intricate interaction between deposition parameters and the resulting thermal characteristics of the diamond film.

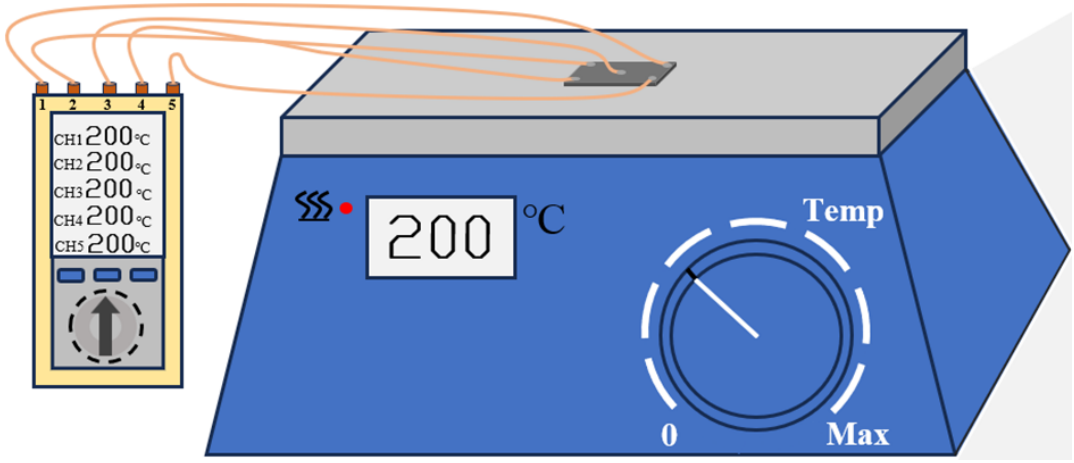

Figure 5.2 Schematic diagram of the thermal response time measurement setup using a hot plate.

5.2.3 Simulation setup

COMSOL Multiphysics 6.1 software was employed to simulate the temperature and gas flow dynamics within the context of magnetic field-assisted HFCVD. An analytical model was established for a cylindrical reactor characterized by specific dimensions: a diameter of 400 mm and a length of 500 mm. The segmentation of the model encompassed distinct zones, namely the inlet, gas reaction area, deposition region, and outlet segment. The temperature profile within the reactor was computed through the utilization of the heat transfer module, while the analysis of fluid dynamics

was conducted using the laminar flow module. Through the resolution of the continuity equation and the Navier-Stokes equation, the investigation successfully elucidated the behaviour of chemical species under the influence of a magnetic field. This scrutiny also encompassed an evaluation of the magnetic phenomena resulting from the external field. Furthermore, an examination was carried out to assess the impact of magnetic field strength and rotational velocity on temperature variations, chemical species distribution, and flow characteristics. In essence, the COMSOL simulation framework facilitates a comprehensive comprehension of the operational principles underlying field-assisted HFCVD. This framework presents avenues for enhancing the deposition process across diverse operational scenarios. The schematic depiction of the HFCVD reactor, as shown in Figure 5.3, delineates the various parameters such as the filament diameter (d), filament separation distance (D), and substrate velocity (n). Each element of the model aligns with the established physical framework. A silicon wafer with dimensions of 20 mm × 20 mm × 0.5 mm served as the substrate, positioned on a graphite sheet forming a cuboid measuring 20 mm × 20 mm × 10 mm, which was further situated on a water-cooled worktable also in the shape of a cuboid measuring 20 mm × 20 mm × 30 mm. This configuration ensured uniform bottom temperature within the HFCVD reactor enclosure. Two tungsten wires, each 200 mm long, were employed as heating components, positioned in parallel at a distance of 5 mm above the substrate.

The introduction of the reactant gas into the reactor occurs via the gas inlet and its expulsion through the gas outlet. Methane functions as the primary carbon source, with hydrogen playing the role of the reacting gas. Under elevated temperatures, hydrogen and methane gases undergo thermal decomposition due to the hot filament, leading to the creation of carbon, hydrogen free radicals, and ions. A magnetic field,

created by a magnet, is responsible for directing the particles it generates to move in an orderly fashion within its confines. This magnetic field configuration rotates around a stationary silicon wafer at a specific velocity. Through the manipulation of the alignment of two magnets, factoring in the repulsion and attraction between different poles, and controlling the strength of magnetic induction, it becomes feasible to concentrate the particles onto the surface of the silicon wafer. An assessment was carried out to analyse the impact of the magnetic field on the deposition process. This assessment involved the computation of the spatial distribution and velocity at which ions and free radicals were deposited onto the substrate surface. In order to streamline the process, specific assumptions were made, for example, excluding chemical reactions like hydrogen atom recombination that occur during deposition. Within the computational framework, variables related to deposition, such as filament temperature and chamber pressure, were regarded as constant values.

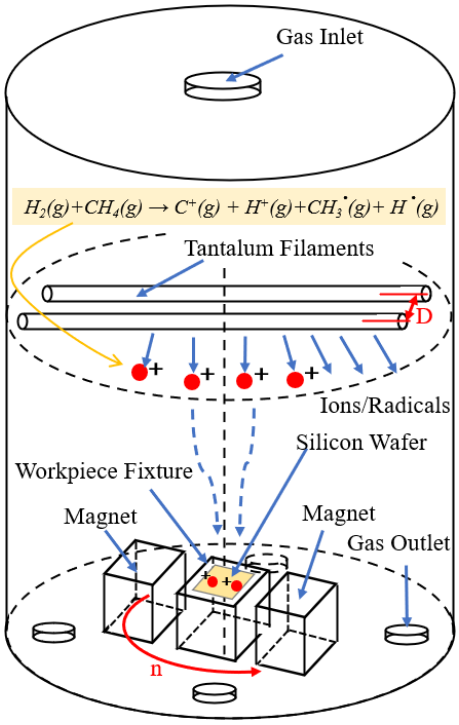

Figure 5.3 Schematic diagram of deposition on the workpiece surface.

5.2.3.1 Configuration of the magnetic field and particle flow state

The stability and distribution of the magnetic field produced by the magnet in the reactor chamber are observed in the absence of any conducting current. As stipulated by the Ampere loop theorem, every closed path within the specified domain fulfils the following condition:

$$\oint_{\partial S} \vec{H} \cdot d\vec{l} = \iint_S \overrightarrow{J_0} \cdot dS = 0 \quad (1)$$

where $\vec{H}$ represents the magnetic field intensity at each point in the region, and dS represents the area element. The magnetic field in this domain becomes a conservative field. Therefore, the magnetic scalar potential V_m can be introduced similarly to the potential in an electrostatic field:

$$\vec{H} = -\nabla \cdot V_m \quad (2)$$

$$\nabla \cdot \vec{B} = 0 \quad (3)$$

Here, $\vec{B}$ is the magnetic flux density vector. According to the conservation of magnetic flux, the constitutive relation of B-H is:

$$\vec{B} = \mu_0 \mu_r \vec{H} \quad (4)$$

where μ_0 is the vacuum permeability and μ_r is the relative permeability. COMSOL Multiphysics software (version 6.1) was utilized for solving these equations under the Lorentz condition to determine the magnetic induction intensity B.

The Reynolds number serves as the key parameter for differentiating between laminar and turbulent flow. $Re = \rho v L/u$ is the ratio of inertial force to viscous force. Based on the calculated Reynolds number being less than 2300, the reaction gas flow and the cooling water flow are defined as laminar flow (Codina et al., 2010; Lee et al., 2012). Hydrogen is defined as an incompressible ideal gas with a flux (standard) of 500

cm³/min, and the mass fraction of methane in the gas mixture is 2%. The cooling water flow rate is set at 25 ml/s according to actual conditions.

The particles generated by the surface reaction of the hot filament enter the magnetic field and are deposited on the silicon wafer surface under the action of Lorentz force. To model particle movement, both the Reynolds-Averaged Navier-Stokes (RANS) turbulence model and the K-W turbulence model are employed. The wall function is utilized for wall processing. The turbulence variable velocity scale U is set at 1 m/s, and the length scaling factor L is 0.035. The governing equations for steady-state particle motion are expressed as follows:

$$\rho(u \cdot \nabla)u = \nabla \cdot [-pI + K] + F \quad (5)$$

$$\nabla \cdot (\rho u) = 0 \quad (6)$$

$$K = \mu(\nabla u + (\nabla u)^T) - \frac{2}{3}\mu(\nabla \cdot u)I \quad (7)$$

Here, ρ is the density of fluid particles, u is the particle velocity with the initial velocity of the particle at the source set at 0.2 m/s in a downward direction (0,0, -1), p is the pressure with an initial value of 1 atm, I is the mixing length limit, and μ μ is the dynamic viscosity of the fluid, assuming a Newtonian fluid. The time scale is represented by T. Using COMSOL software (version 6.1), the velocity u and its components u_x, u_y, and u_z can be calculated.

5.2.3.2 Simulation setup for solid heat transfer

The temperature distribution of the HFCVD diamond film substrate is influenced by thermal radiation, heat conduction between fluid and solid components, and heat convection between gas and water. Therefore, three heat transfer mechanisms radiation, conduction, and convection are used to calculate the temperature distribution inside the reactor. The conservation equations used to simulate heat transfer in HFCVD systems are as follows:

Mass conservation:

$$\nabla \times (\rho \vec{v}) = 0 \quad (8)$$

Conservation of momentum:

$$\nabla \times (\rho \vec{v}\vec{v}) = -\nabla p + \nabla \times \mu(\nabla \vec{v} + \nabla \vec{v}^T) + \rho \vec{g} \quad (9)$$

Conservation of energy:

$$\nabla \times \rho c_p \vec{v} T = \nabla \times (k \nabla T) + S_h \quad (10)$$

where ρ is the density of the fluid, v is the velocity vector, p is the pressure, μ μ is the viscosity coefficient, T T is the temperature, k k is the thermal conductivity, and S_h is the heat source. In this model, the heat transfer equation is:

$$\rho C_p \frac{\partial T}{\partial t} + \rho C_p u \cdot \nabla T + \nabla \cdot q = Q \quad (11)$$

$$q = -k \nabla T \quad (12)$$

Here, ρ is the solid density, C_p is the solid heat capacity at constant pressure, k is the solid thermal conductivity (expressed as a scalar or tensor if the thermal conductivity is anisotropic), u is the velocity field defined by the Translational Motion sub-node when portions of the model are moving in the material frame, Q is the heat source, and q is the heat flux vector. The temperature gradient (∇T) is the temperature gradient.

In the numerical simulation, several details are assumed for simplicity. The boundary treatment of the cooling chamber wall and the bottom of the table is handled using an isothermal boundary condition of 293.15 K. Heat dissipation is considered through four layers of temperature gradients in the tables and brackets made of graphite and copper substrates. All materials are assumed to be grey bodies. Given the oxidation of materials in the HFCVD system, an emissivity value slightly higher than that of general metals is used (Kanaya & Kawakatsu, 1972; Song et al., 2017).

5.2.3.3 Mesh generation and boundary conditions

Based on the actual temperature measured by the infrared thermometer during deposition, the hot filament temperature is defined as 2350 K. The initial ambient temperature is set to 293.15 K, and the pressure in the reactor is maintained at 3 kPa. The boundary condition for the filament is defined as a constant temperature boundary with an emissivity of 0.28 on the filament surface (Allen et al., 1960). The substrate boundary is a coupled boundary condition, so the substrate temperature is determined by calculation. The defined material properties (all at room temperature except for the tungsten wire at 230°C) are listed in Table 5.3, where ρ is the density, K is the thermal conductivity and c_p is the specified heat capacity.

Table 5.3 Material properties assigned for the simulation model.

Material	$\rho/\ (kg \cdot m^{-3})$	$K/\ (W \cdot m^{-2} \cdot K^{-1})$	$c_p/(J \cdot kg^{-1} \cdot K^{-1})$
Hydrogen	0.01	0.1769	14439.68
Methane	0.7174	0.109	2200
water	998.24	0.5941	4186
Copper	8939.81	386.7	383.02
Graphite	1800	130	710
Silicon	2300	140	700

The HFCVD system is described using the 3D geometric structure shown in Figure 5.3. The system is divided into multiple control bodies according to Cartesian coordinates (X, Y, Z). Most control bodies are described using a free tetrahedral mesh, and the physical boundary is represented by corner refinement mesh. The complete grid contains 760,957 domain units, 24,572 boundary units, and 3,246 edge units. The simulation employs the CFD code COMSOL Multiphysics 6.1 to solve the coupling problem of magnetic field, flow field, and heat transfer using the FEM algorithm.

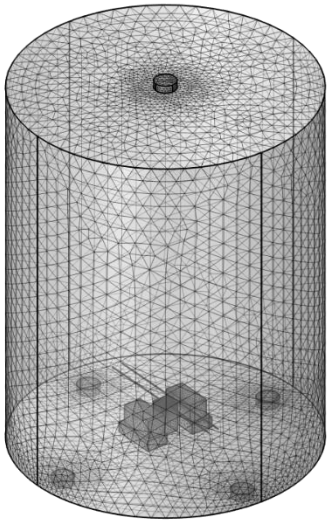

Figure 5.4 Complete mesh grid generated for MA-HFCVD simulation.

5.3 Simulation results

5.3.1 Simulation of magnetic field distribution

Figure 5.5 depicts the distribution of the magnetic field resulting from the symmetrical arrangement of two 400 mT magnets within the field domain. The magnets illustrated in Figure 5.5(a) and Figure 5.5(b) exemplify the concepts of attraction and repulsion. The alignment of magnetic vectors, as denoted by arrows, is symmetrical along the z-axis. Simulation outcomes reveal a symmetrically distributed parabolic magnetic field enveloping the workpiece. The magnetic attraction between the two magnets in Figure 5.5(a) establishes a left-to-right magnetic field, guiding particles along the magnetic field lines through the Lorentz force for deposition on the substrate surface. In Figure 5.5(b), the magnetic repulsion between the magnets generates four distinct parabolic magnetic fields symmetrically positioned between them. Despite the magnetic field lines converging towards the substrate centre, particles in the magnetic susceptibility field also tend to move towards the substrate. This specific configuration of magnetic fields facilitates the precise positioning of particles on the substrate surface.

To enhance the consistency of diamond deposition, the magnetic field system rotates around the stationary substrate at a speed of 2rpm. Further simulations are carried out to assess the system's performance at magnetic field strengths of 0 mT and 400 mT.

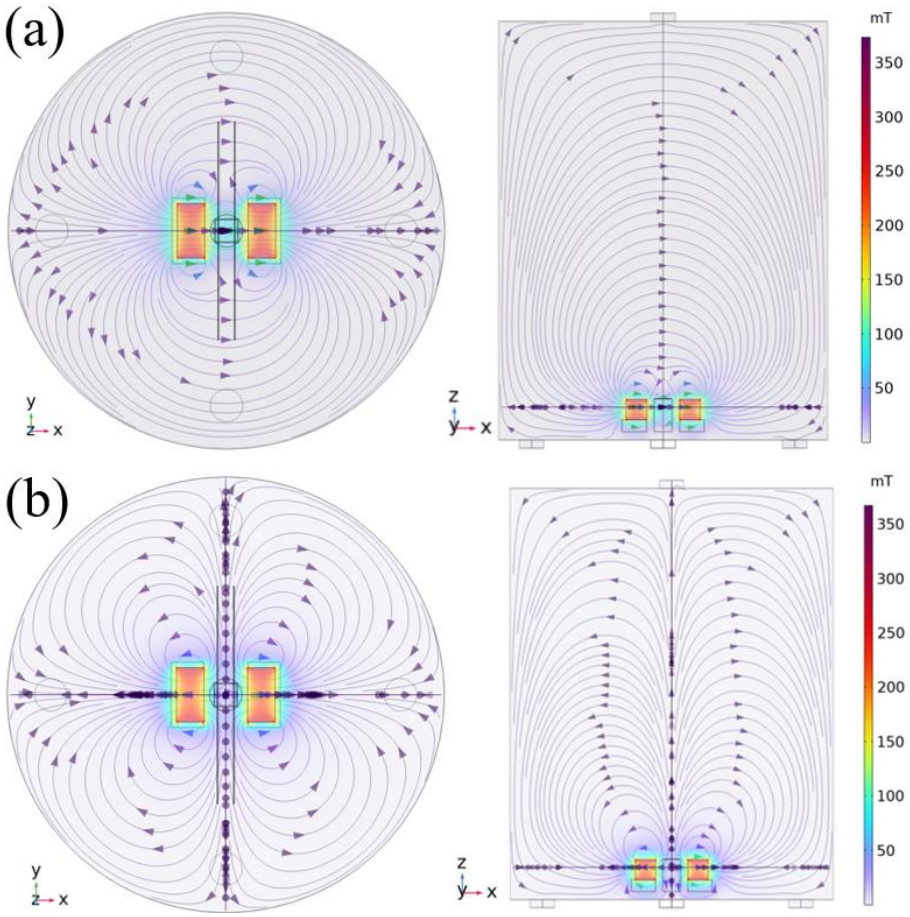

Figure 5.5 Simulation results for magnetic flux density at 400 mT. (a) Magnet attraction arrangement; (b) Magnet repulsion arrangement.

5.3.2 The influence of temperature field on deposition

Hydrogen and methane experience decomposition into reactive chemical species in close proximity to the hot filament at elevated temperatures. The transportation of these species towards the substrate is facilitated by molecular movement and the presence of a magnetic field. The temperature of the surface of the substrate plays a significant role in determining the orientation of diamond crystals. Alterations in substrate temperatures induce variations in the configuration of carbon

active species, leading to distinct grain sizes in the resulting diamond. Therefore, the substrate temperature is crucial in the context of diamond film deposition through the process of HFCVD. The temperature profile of the silicon substrate under different conditions, without rotation, is depicted in Figure 5.6 (a-c). The left panel illustrates the temperature distribution under a magnetic field strength of 0 mT. The middle panel represents the temperature profile under a magnetic field strength of 400 mT with magnets exhibiting repulsion. The right panel showcases the temperature distribution under a magnetic field strength of 400 mT with attracting magnets. In the absence of a magnetic field, the temperature of the wafer substrate ranges from 808 to 833°C. The uneven heat distribution from the hot filament and the lack of rotation contribute to higher temperatures at the substrate's periphery. When the magnets repel at a magnetic field strength of 400 mT, the central temperature of the wafer substrate varies from 845 to 863°C, whereas the edge temperature ranges from 865 to 872°C. Under a magnetic field strength of 400 mT, the central temperature of the magnets spans from 847 to 862 °C, with the edge temperature potentially reaching up to 874 °C. Figures 5.6 (d-f) present the temperature distribution of the wafer under different magnetic field conditions while the substrate is in rotation. At a magnetic field strength of 0 mT, the central temperature falls within the range of 804-814°C, characterized by a relatively uniform temperature distribution. With magnets exhibiting repulsion at a magnetic field strength of 400 mT, the central temperature ranges from 838 to 854°C, while the edge temperature varies from 860 to 867°C. Under a magnetic field strength of 400 mT, the central temperature varies from 845 to 867 °C, with the edge temperature ranging from 867 to 872 °C. The simulation outcomes reveal that the temperature of the wafer substrate increases with higher magnetic field strengths. This rise is attributed to the boost in molecular thermal movement of particles and active species induced by the

Lorentz force. The outermost section of a single substrate experiences elevated temperatures, gradually decreasing towards the centre. The temperature profile of the silicon wafer substrate demonstrates elevated temperatures at the centre and lower temperatures at the edges, which is closely linked to the thermal contact model of the graphite fixture. The central part of the substrate undergoes a faster cooling process, resulting in enhanced heat absorption by the graphite substrate in this region and consequently leading to a lower temperature at the centre.

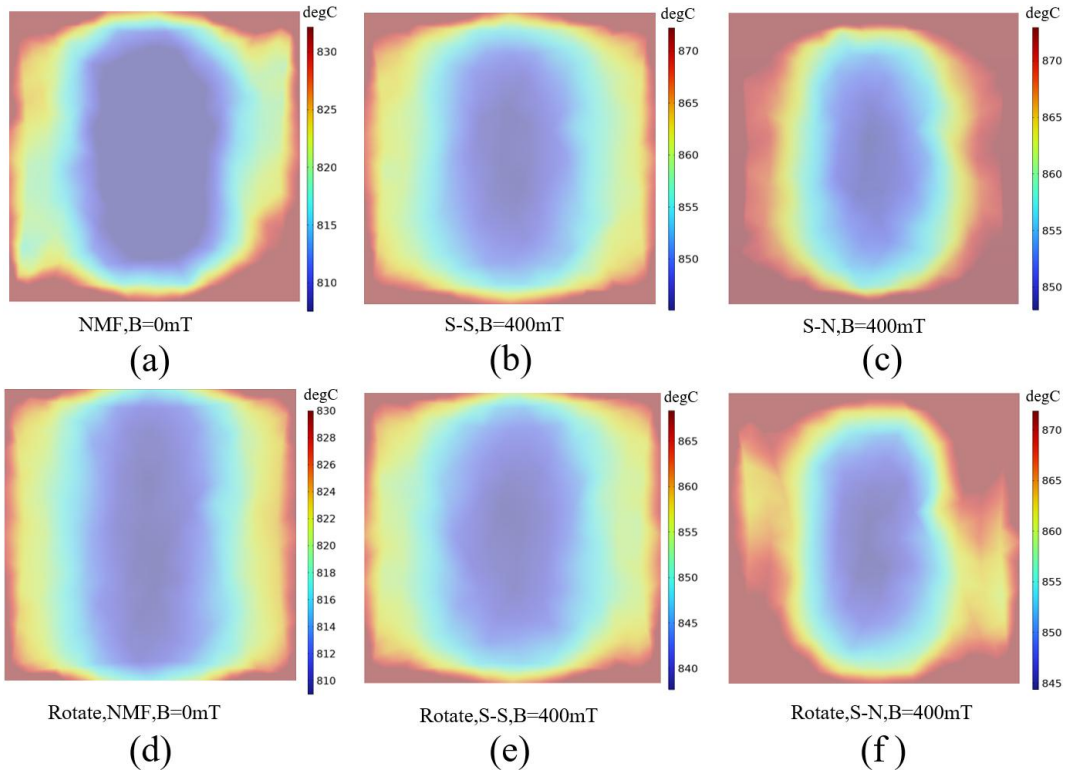

Figure 5.6 Simulation of substrate temperature distribution: (a-c) No magnetic field, magnets repelling each other, and magnets attracting each other; (d-f) With substrate rotation, no magnetic field, magnets repelling each other, and magnets attracting each other.

5.3.3 The influence of particle flow state on deposition

Methane and hydrogen are utilized to generate the carbon species essential for the deposition of diamond on the heated filament's surface. The concentration of carbon species present on the silicon wafer substrate's surface directly influences the efficacy and calibre of diamond deposition. A schematic diagram in Figure 5.7 delineates the distribution of free radicals' concentration in the vicinity of the silicon wafer substrate. The outcomes of the simulation reveal that the application of a magnetic field significantly boosts the concentration of free radicals on the substrate's surface by a magnitude of 10 to 100, thereby effectively heightening the nearby concentration of free radicals in the silicon wafer. Figure 5.7 (a-c) depicts the radicals' concentration on the substrate's surface under various magnetic field configurations without rotation: 0 mT, 400 mT with repelling magnets, and 400 mT with attracting magnets. In contrast, Figure 5.7 (d-f) illustrates the radicals' concentration on the substrate's surface when the magnetic field rotates at 2 rpm under the same magnetic field settings. The existence of a magnetic field substantially enriches the abundance of radicals on the silicon wafer substrate's surface. Through the rotation of the magnetic field at a specific speed, a more uniform dispersion of radicals on the silicon wafer's surface is accomplished.

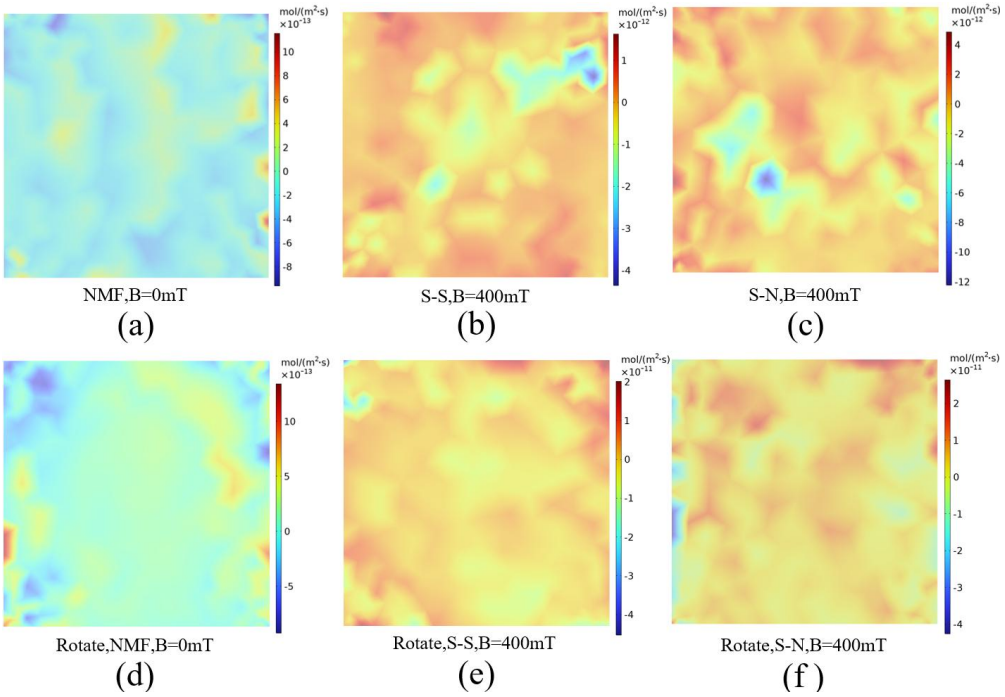

Figure 5.7 Simulation of CH3· radical concentration distribution on the substrate surface without a magnetic field, magnets repelling each other, and magnets attracting each other: (a-c) 0rpm; (d-f) 2rpm.

5.4 Experimental result and analysis

5.4.1 Thickness distribution

This section provides a detailed analysis of the effects of different magnetic field orientations on the thickness and consistency of diamond films deposited at the centre of silicon wafers using HFCVD. The study systematically measured the coating thickness under three magnetic field configurations: No Magnetic Field (NMF), South-South (SS), and South-North (SN), at rotational speeds of 0, 1 rpm, and 2 rpm, as illustrated in Figure 5.8 and Figure 5.10.

The absence of a magnetic field (NMF), the coating thickness at the wafer centre demonstrates stable growth regardless of rotational speed. Without magnetic influence, the deposition process remains largely unaffected by rotational variation. As shown in Figure 8(a), at 0 rpm, the coating appears uniform and smooth, indicating

consistent deposition. As the rotational speed increases to 1 rpm (Figure 5.8(b)) and 2 rpm (Figure 5.8(c)), the thickness remains similar, with overall uniformity and smoothness maintained. This consistency underscores the stability of the deposition process under NMF conditions.

When the magnetic field is aligned in the South-South (SS) configuration, deposition dynamics become more complex. At 0 rpm (Figure 5.8(d)), the film thickness is already higher than under NMF, with a slightly rougher surface. As rotational speed increases to 1 rpm (Figure 5.8(e)) and 2 rpm (Figure 5.8(f)), the surface roughness and variability in thickness increase, suggesting that SS alignment influences the concentration of reactive species at the wafer centre. This pattern indicates that rotational motion under SS alignment affects deposition dynamics, resulting in thicker and less uniform films compared to the NMF condition.

The South-North (SN) alignment excels in achieving uniformity and consistency in film thickness. At 0 rpm (Figure 5.8(g)), the SN alignment produces a thicker film than the NMF and SS configurations, with a smooth and homogeneous surface. As rotational speed increases to 1 rpm (Figure 5.8(h)) and 2 rpm (Figure 5.8(i)), the film thickness increases steadily and controllably, maintaining consistency across all increments. The SN alignment effectively harnesses rotational energy to optimize the distribution of reactive species, leading to a thicker and more uniform film, demonstrating the synergistic effect of SN alignment and rotation.

Figure 9 summarizes the coating thickness at the wafer centre for different configurations and rotational speeds. The SN configuration consistently results in the highest and most uniform thickness, increasing from 6.88 μm at 0 rpm to 7.41 μm at 2 rpm. The SS configuration shows increased thickness with higher rotational speeds, from 6.16 μm at 0 rpm to 6.61 μm at 2 rpm. In contrast, the NMF configuration

maintains relatively stable thickness, ranging from 6.33 µm to 6.46 µm, highlighting the minimal impact of rotational dynamics without a magnetic field.

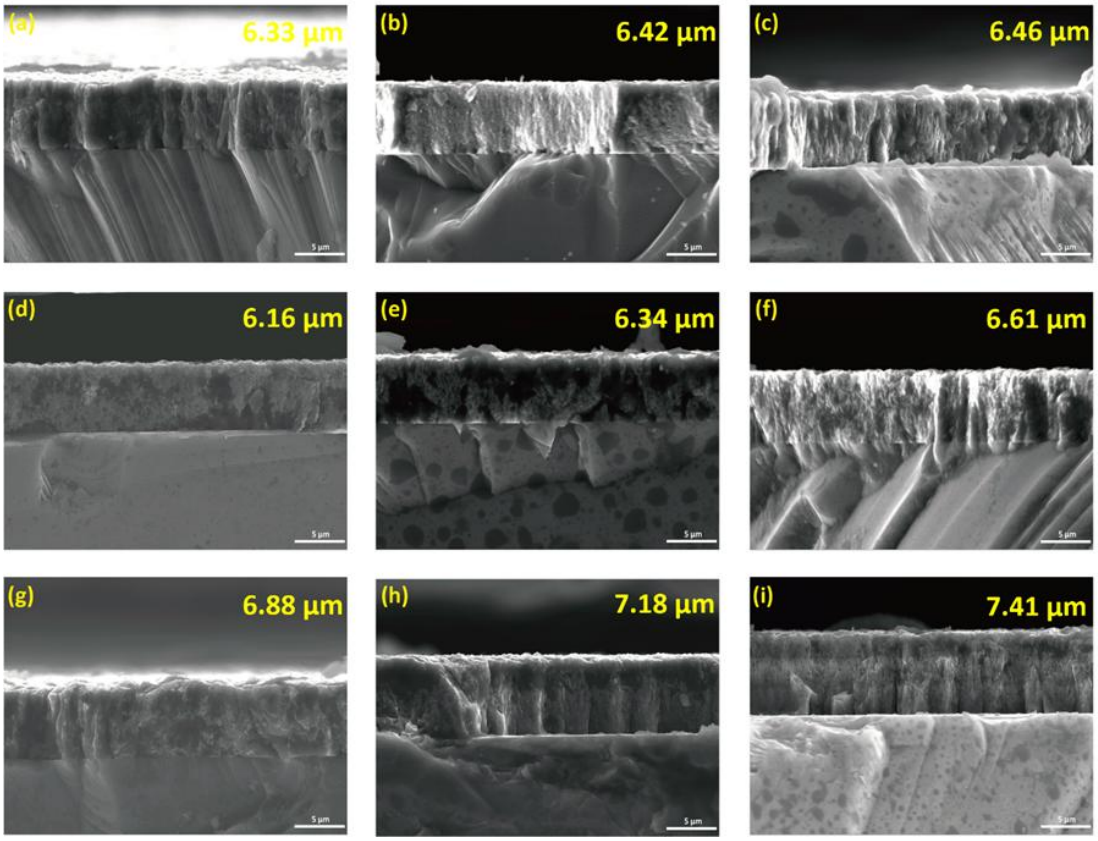

Figure 5.8 Cross section of film thickness on silicon wafer at the centre area with different magnetic field orientations and rotational speeds: (a) 0rpm NMF; (b) 1rpm NMF ; (c) 2rpm NMF ; (d) 0rpm SS ; (e) 1rpm SS; (f) 2rpm SS ; (g) 0rpm SN ; (h) 1rpm SN ; (i) 2rpm SN.

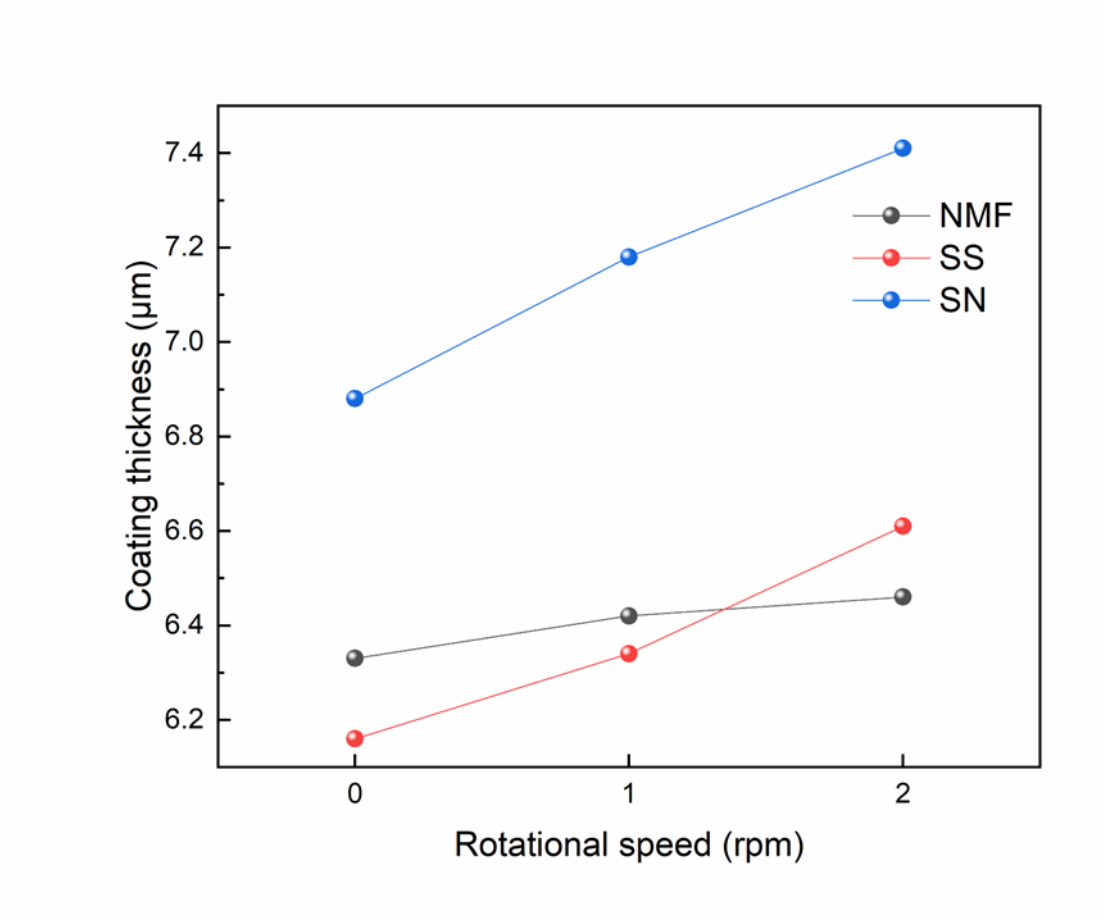

Figure 5.9 The summary of coating thickness of the centre area of the silicon wafer for different magnetic field configurations at various rotational speeds.

Under NMF conditions, the edge of the silicon wafer shows a nearly uniform thickness profile, with slight increases as speed increases, from 6.61 μm at 0 rpm to 6.69 μm at 2 rpm, reflecting the process's stability without magnetic influence (Figures 5.10a-c). This consistency emphasizes the deposition process's inherent stability in the absence of external magnetic forces.

Switching to the SS alignment, edge thickness dynamics change noticeably. At 0 rpm (Figure 5.10(d)), the edge thickness is initially higher, with a rougher surface compared to NMF. As rotational speed increases to 1 rpm (Figure 5.10(e)) and 2 rpm (Figure 5.10(f)), the edge thickness decreases, with reduced roughness and improved uniformity. This suggests that SS alignment and rotational motion affect the

distribution of reactive species, leading to a more even coating as speed increases. The initial thicker coating at 0 rpm and subsequent decrease with increased rotation highlight the interaction between magnetic fields and rotational dynamics, influencing the deposition process.

The SN alignment demonstrates superior performance in maintaining edge uniformity across varying rotational speeds. At 0 rpm (Figure 5.10(g)), the SN alignment produces a uniform and smooth coating, thinner than the SS alignment. As rotational speed increases to 1 rpm (Figure 5.10(h)) and 2 rpm (Figure 5.10(i)), the edge thickness shows minor decreases, resulting in a relatively consistent and uniform thickness profile. The surface remains smooth and homogeneous, indicating the SN alignment's ability to promote uniform deposition and effectively distribute reactive species. This configuration maintains a stable and even thickness, even at the wafer edges, where variations are typically more pronounced.

Figure 5.11 summarizes the edge thickness for different configurations and rotational speeds. The SN configuration shows the most consistent thickness, decreasing slightly from 7.82 μm at 0 rpm to 7.51 μm at 2 rpm. The SS configuration exhibits a significant reduction in thickness with increased speed, from 8.54 μm at 0 rpm to 7.83 μm at 2 rpm, indicating improved uniformity. The NMF configuration maintains stable thickness across all speeds, ranging from 6.61 μm to 6.69 μm, reflecting the lack of influence from rotational dynamics without a magnetic field.

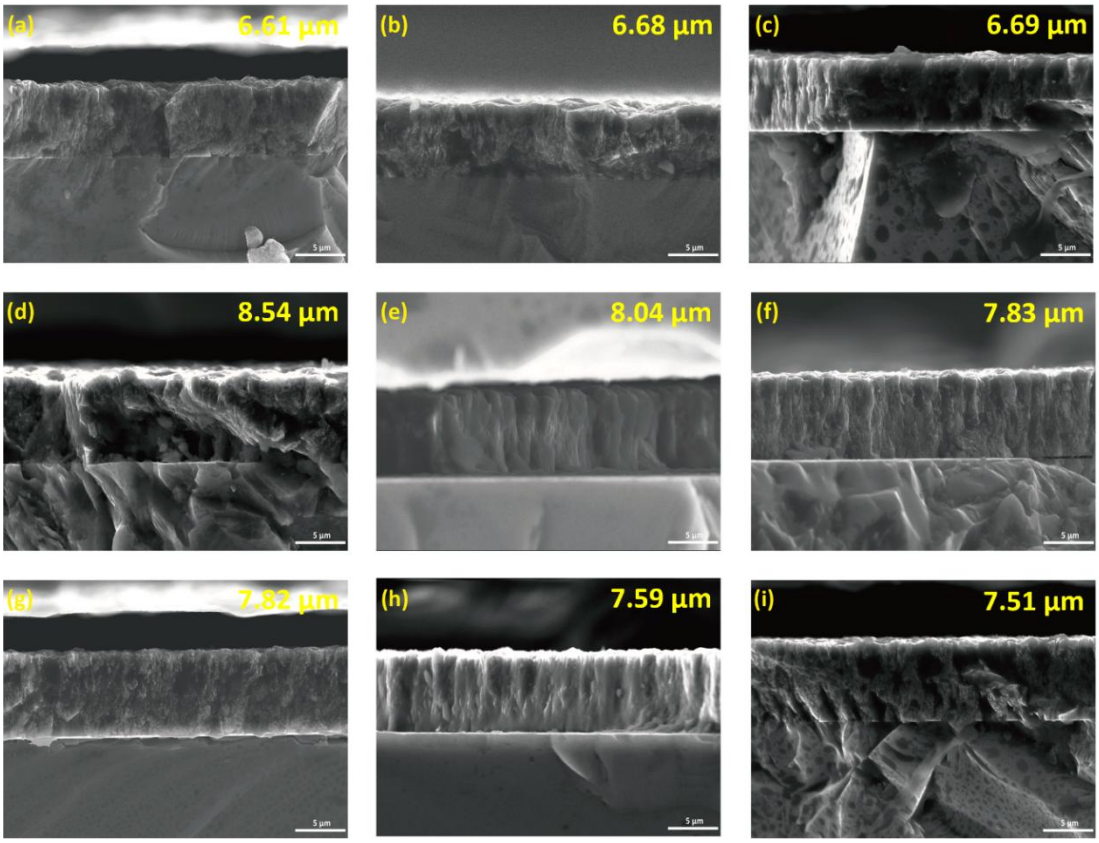

Figure 5.10 Cross section of film thickness on silicon wafer at the edge area with different magnetic field orientations and rotational speeds: (a) 0rpm NMF; (b) 1rpm NMF; (c) 2rpm NMF; (d) 0rpm SS; (e) 1rpm SS; (f) 2rpm SS; (g) 0rpm SN; (h) 1rpm SN; (i) 2rpm.

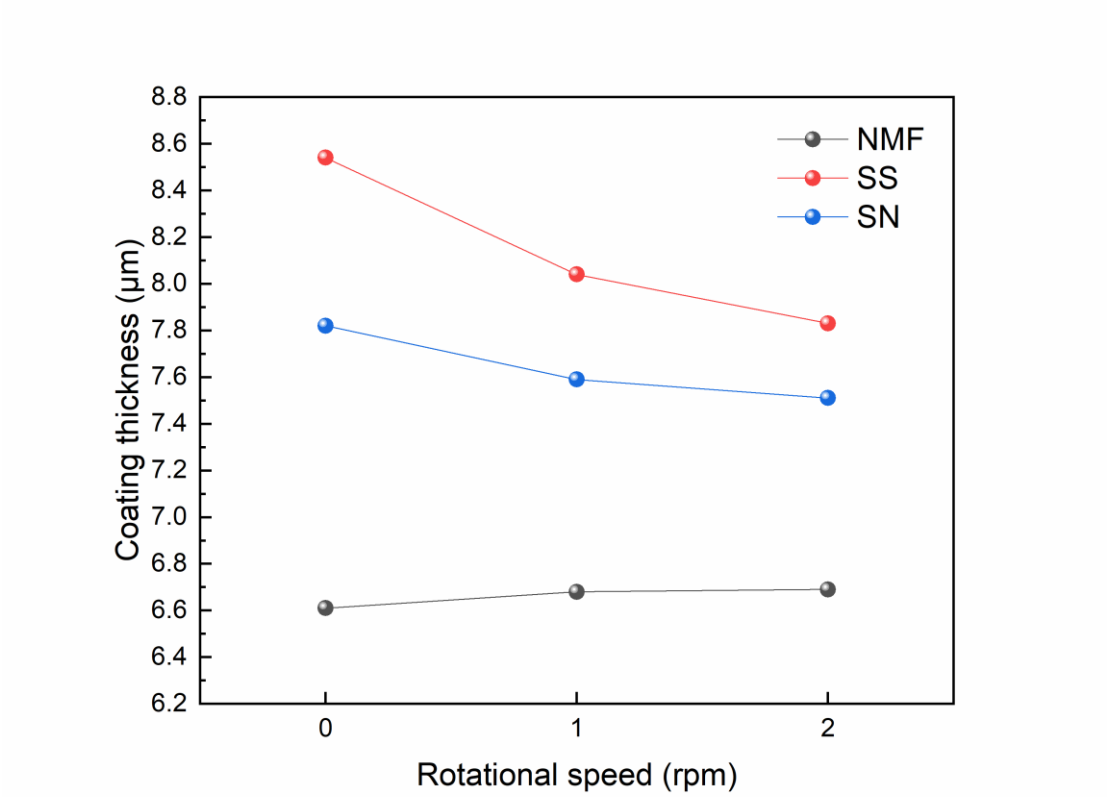

Figure 5.11Summary of coating thickness at the edge area of silicon wafer for different magnetic field configurations at various rotational speeds.

The data from Figures 5.9 and Figure 5.11 provide a comprehensive overview of coating thickness under different magnetic field orientations and rotational velocities. The SN configuration consistently produces the highest uniformity and thickness, regardless of speed. The SS configuration shows increased thickness with rising speeds, demonstrating how magnetic influence can enhance deposition, though careful management is required to ensure overall uniformity. The deposition dynamics and radical generation in HFCVD processes are intricately influenced by magnetic field orientation. The SS orientation may create localized high-intensity areas with amplified radical generation, risking non-uniform distribution across the substrate. Introducing rotational dynamics helps mitigate this by continuously redistributing chemical species, demonstrating the MA-HFCVD technique's capability to control film properties

through magnetic field manipulation and rotation. These findings highlight the critical role of magnetic field dynamics in optimizing film deposition by improving uniformity and consistency.

5.4.2 Diamond film morphology

The morphological characteristics of diamond films synthesized via MA-HFCVD are significantly influenced by both the alignment of the magnetic field and the rotational speed during deposition. At the centre of the silicon wafer, in the absence of a magnetic field (NMF), grain sizes exhibit random growth patterns. Figure 5.12(a) shows that at 0 RPM, the diamond film morphology consists of grains that are randomly distributed, with a mixture of small and moderately larger grains. This randomness persists even at 1 RPM (Figure 5.12b), with a slight tendency toward smaller grains, but the distribution remains relatively random. At 2 RPM (Figure 5.12c), the grain sizes decrease slightly, indicating that without the influence of a magnetic field, grain sizes tend to remain small and decrease marginally as rotational speed increases.

Under the South-South (SS) alignment, the grain sizes at the centre of the wafer exhibit more significant variation. At 0 RPM (Figure 5.12d), the grains are larger and more unevenly distributed compared to the NMF condition. As rotational speed increases to 1 RPM (Figure 5.12e), grain sizes remain relatively large but begin to show signs of reduced size and improved uniformity. At 2 RPM (Figure 5.12f), grain sizes decrease noticeably, suggesting that while SS alignment initially promotes larger grain sizes at the centre, increasing rotational speed leads to smaller, more uniform grains.

The South-North (SN) alignment produces the most consistent distribution of grain sizes at the centre of the wafer. At 0 RPM (Figure 5.12g), the grains are uniformly larger compared to those in the NMF and SS conditions, indicating a more controlled growth environment. As rotational speed increases to 1 RPM (Figure 5.12h), grain sizes

decrease slightly but maintain a uniform distribution. At 2 RPM (Figure 5.12i), grain sizes reduce further, resulting in a uniform orientation that promotes relatively larger grains at the centre compared to the NMF and SS configurations, though with a decrease in size as rotational speed increases.

These observations suggest that the SN alignment provides the most uniform and consistent grain sizes, while the SS alignment leads to larger grains that decrease in size with increased rotation. The NMF condition is characterized by random grain growth with a slight decrease in size as rotational speed increases. Overall, the impact of rotational speed is evident across all magnetic field alignments, with higher rotational speeds generally leading to smaller grain sizes by promoting a more even distribution of reactive species.

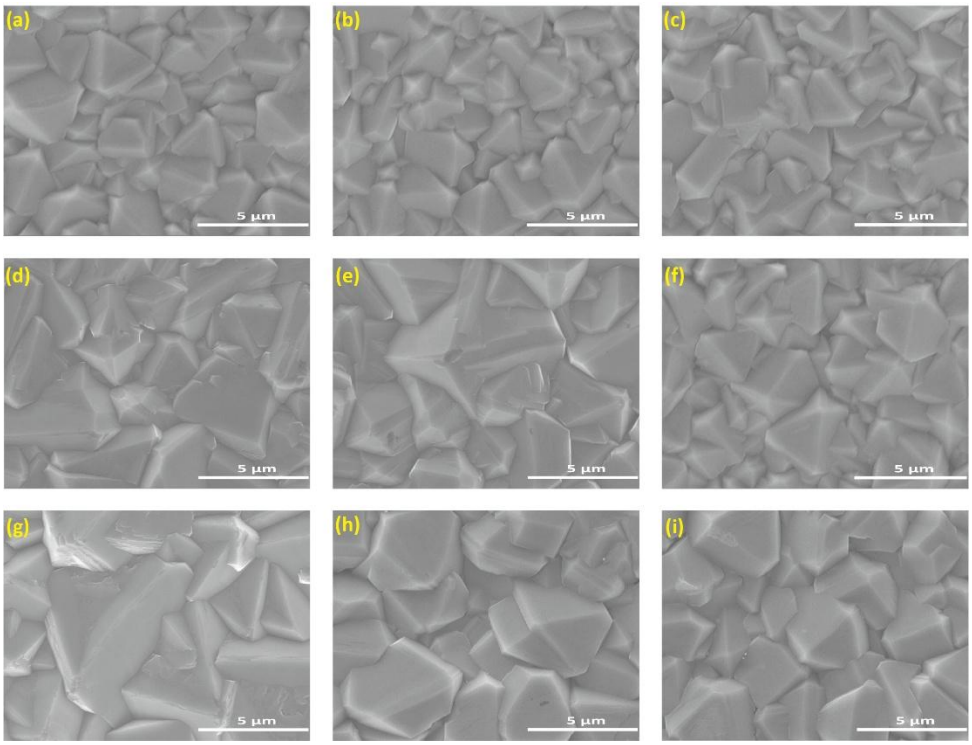

Figure 5.12 Surface morphology on silicon wafer centre deposit with different magnetic field orientations and rotational speeds: (a) 0rpm NMF; (b) 1rpm NMF; (c) 2rpm NMF; (d) 0rpm SS; (e) 1rpm SS; (f) 2rpm SS; (g) 0rpm SN; (h) 1rpm SN; (i) 2rpm SN.

Figure 5.13 summarizes the grain size distribution under different experimental setups, highlighting the impact of rotational speed. In the NMF configuration, grain size decreases slightly with increasing RPM, from 1.90 μm at 0 RPM to 1.75 μm at 2 RPM, showing limited sensitivity to rotation. Conversely, the SS configuration exhibits a more pronounced reduction in grain size with rotation, from 2.71 μm at 0 RPM to 1.90 μm at 2 RPM, suggesting that rotation enhances grain uniformity. The SN configuration begins with the largest grains at 3.34 μm at 0 RPM and experiences a steady decrease with rotation, reaching 2.95 μm at 2 RPM, underscoring the beneficial effect of rotation on grain size control. These findings indicate that rotational speed plays a more significant role in reducing grain size and enhancing uniformity in the SS and SN configurations than in NMF, with SN showing the most considerable improvement toward larger but more uniform grains under rotation.

PDI was calculated using the method defined in Chapter 4, based on SEM grain size measurements for each magnetic configuration and rotation speed. Grain size uniformity on the centre area of the silicon wafer was quantified using PDI for different magnetic field configurations at rotation speeds of 0, 1, and 2 rpm are summarised in Table 5.4. Under NMF, PDI increased from 0.16 at 0 rpm to 0.18 at 1 rpm and 0.21 at 2 rpm, indicating a broader grain size distribution with increasing rotation speed. Under SS, relatively high PDI values were obtained at 0 and 1 rpm (0.34 and 0.36), while a marked reduction occurred at 2 rpm (0.15), indicating improved grain size uniformity at higher rotation speed. Under SN, PDI decreased progressively with rotation speed from 0.22 at 0 rpm to 0.17 at 1 rpm and 0.09 at 2 rpm. The lowest PDI value on the centre region was obtained under SN at 2 rpm, corresponding to the narrowest grain size distribution among the tested conditions.

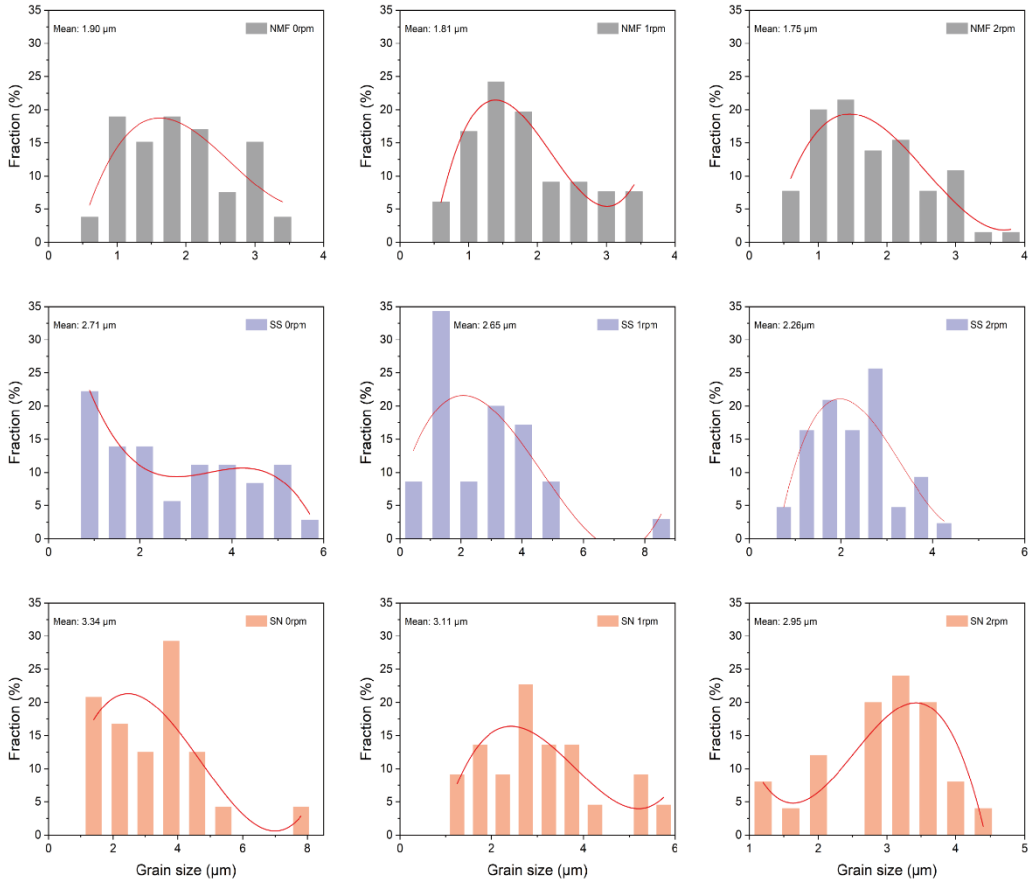

Figure 5.13 Grain size distribution on the centre area silicon wafer for different magnetic field configurations at various rotational speeds.

Table 5.4 PDI values at wafer centre for different magnetic configurations and rotation speeds.

Samples	0 rpm	1 rpm	2rpm
NMF	0.16	0.18	0.21
SS	0.34	0.36	0.15
SN	0.22	0.17	0.09

At the edges of the silicon wafer, in the absence of a magnetic field (NMF), grain sizes exhibit random growth patterns. The larger grain sizes at the edges are primarily attributed to temperature gradients that influence growth. Without specific numerical values, it is observed that at 0 RPM (Figure 5.14a), grain sizes are randomly distributed and larger than at the centre. As rotational speed increases to 1 RPM (Figure

5.14b), grain sizes decrease slightly but maintain a random distribution. At 2 RPM (Figure 5.14c), grain sizes decrease further, suggesting that without a magnetic field, grain growth at the edges remains relatively stable across different rotational speeds, with only slight decreases in size.

Under SS alignment, there is a notable accumulation of reactive species toward the edges, resulting in considerably larger grain sizes. At 0 RPM (Figure 5.14d), grain sizes are larger and more uneven compared to the NMF condition. As rotational speed increases to 1 RPM (Figure 5.14e), grain sizes decrease slightly but remain larger than those under the NMF condition. At 2 RPM (Figure 5.14f), grain sizes decrease further, indicating that SS alignment initially promotes larger grain sizes at the edges, but increasing rotational speed leads to smaller, more uniform grains.

The SN alignment shows consistent grain sizes at the edges. At 0 RPM (Figure 5.14g), grain sizes are larger and more uniform compared to the NMF and SS conditions. As rotational speed increases to 1 RPM (Figure 5.14h), grain sizes decrease slightly but maintain uniform distribution. At 2 RPM (Figure 5.14i), grain sizes decrease further, resulting in a uniform grain size distribution at the edges, larger than those in the NMF and SS configurations but decreasing in size with increased rotational speed. These observations suggest that the SN alignment provides the most uniform and consistent grain sizes, whereas the SS alignment initially leads to larger grains that decrease in size with increased rotation. The NMF condition shows random grain growth, with a slight decrease in size as rotational speed increases. Across all magnetic field alignments, higher rotational speeds generally promote smaller grain sizes by enhancing the distribution of reactive species.

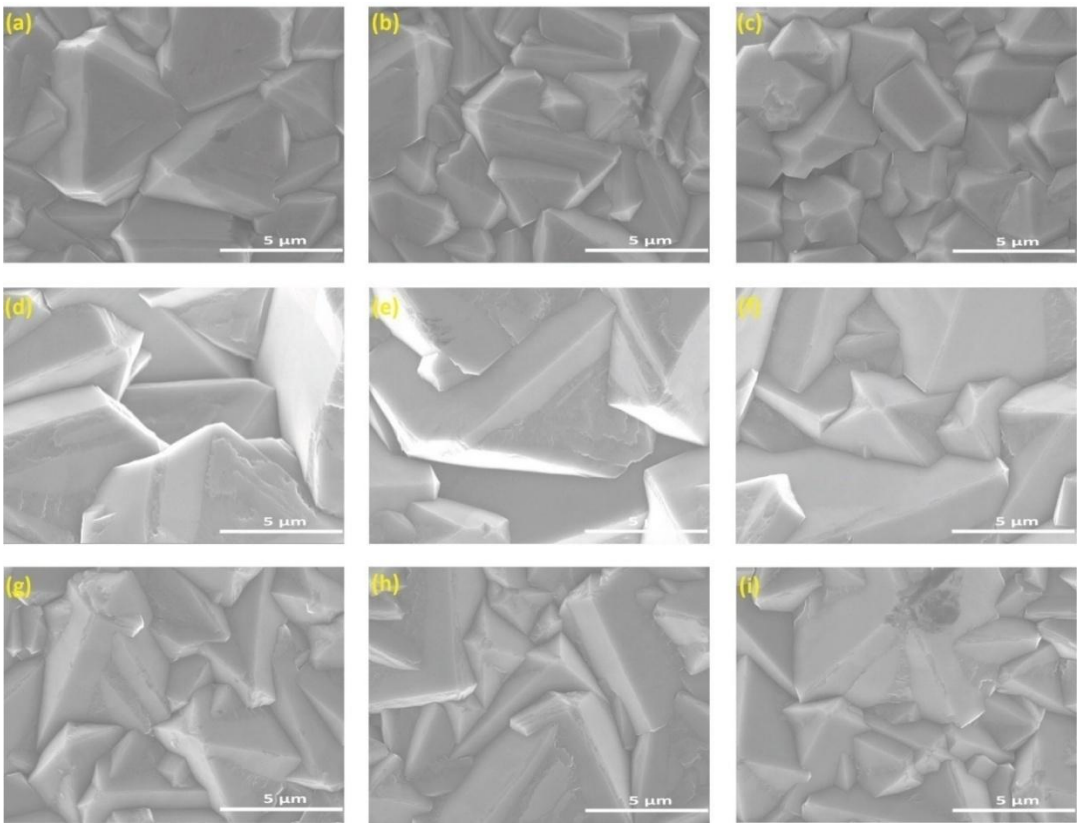

Figure 5.14 Surface morphology on silicon wafer edges deposit with different magnetic field orientations and rotational speeds: (a) 0rpm NMF; (b) 1rpm NMF; (c) 2rpm NMF; (d) 0rpm SS; (e) 1rpm SS; (f) 2rpm SS; (g) 0rpm SN; (h) 1rpm SN; (i) 2rpm SN.

Figure 5.15 provides further insights into the grain size distribution at the edges under various conditions. In the NMF setup, grain size changes minimally with increasing RPM, from 2.87 µm at 0 RPM to 2.85 µm at 2 RPM, indicating low sensitivity to rotation. The SS configuration demonstrates a substantial decrease in grain size with rotation, from 6.17 µm at 0 RPM to 4.67 µm at 2 RPM, highlighting the effectiveness of rotation in achieving more uniform grain sizes at the edges. The SN configuration also shows a decrease in grain size, starting at 3.59 µm at 0 RPM and reaching 3.39 µm at 2 RPM, while maintaining relatively larger but more uniform grains with rotation. These trends suggest that while the NMF setup is less affected by

rotation, both SS and SN configurations benefit significantly from increased RPM in achieving better grain size uniformity, with SS showing the most dramatic improvement. PDI values for the edge area under different magnetic configurations and rotation speeds are summarised in Table 5.5. Under NMF, PDI decreased from 0.31 at 0 rpm to 0.29 at 1 rpm and further to 0.10 at 2 rpm, indicating a narrower grain size distribution at higher rotation speed. Under SS, PDI increased from 0.25 at 0 rpm to 0.44 at 1 rpm and remained high at 0.38 at 2 rpm, indicating reduced grain size uniformity under SS with rotation. Under SN, PDI increased from 0.26 at 0 rpm to 0.33 at 1 rpm and then decreased to 0.27 at 2 rpm, indicating moderate dispersion with partial recovery at 2 rpm. The lowest PDI value at the edge was obtained under NMF at 2 rpm, while the highest PDI value was obtained under SS at 1 rpm.

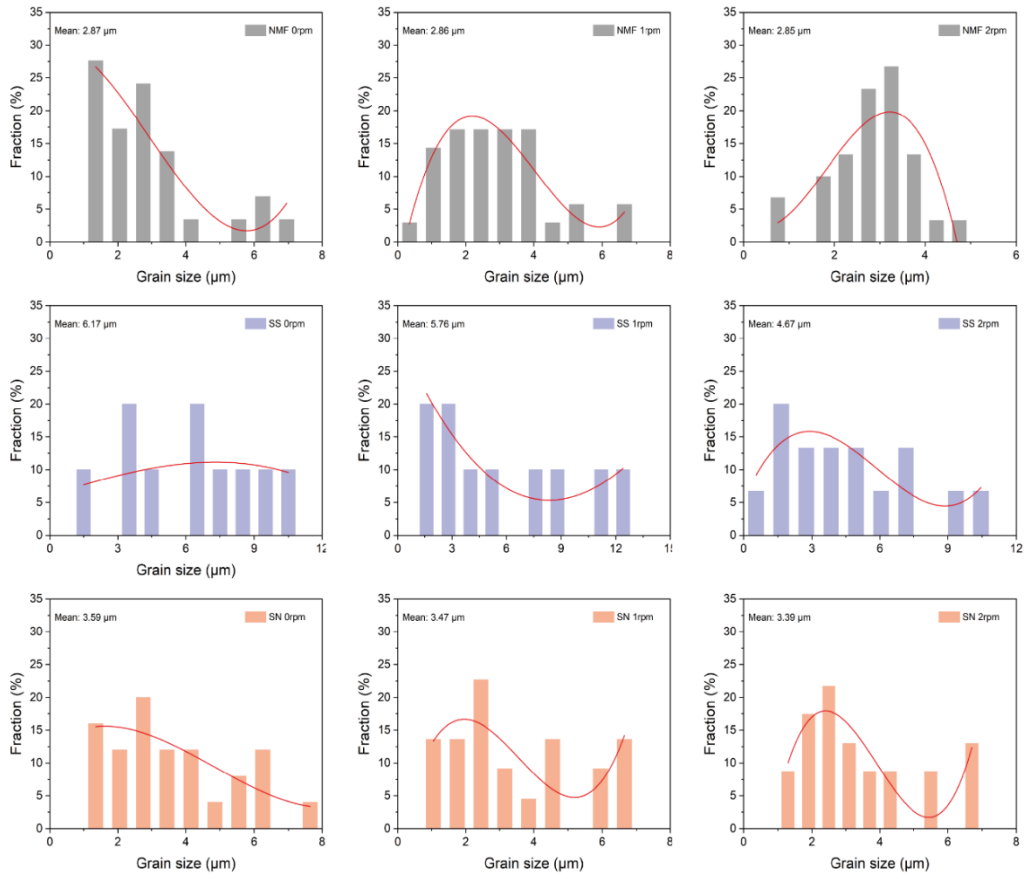

Figure 5.15 Grain size distribution on the edge area of silicon wafer for different magnetic field configurations at various rotational speeds.

Table 5.5 PDI values at wafer edge for different magnetic configurations and rotation speeds.

Samples	0 rpm	1 rpm	2rpm
NMF	0.16	0.18	0.21
SS	0.34	0.36	0.15
SN	0.22	0.17	0.09

The combined visual and numerical analyses of Figure 5.12, Figure 5.13, Figure 5.14, and Figure 5.15 highlight the significant impact of magnetic field orientation and rotational speed on the grain size distribution in diamond films synthesized through MA-HFCVD. The SN configuration consistently yields the most uniform and largest grains, benefiting greatly from rotational dynamics, while the SS configuration shows a reduction in grain size with increased rotation. The NMF configuration, both at the centre and edges, remains largely unaffected by rotational speed, emphasizing the crucial role of magnetic fields in optimizing diamond film deposition. These findings offer valuable insights into the controlled synthesis of diamond films, underscoring the importance of magnetic field manipulation in achieving desired film properties.

5.5 Thermal conductivity analysis

This session conducted a detailed investigation into the structural and thermal properties of diamond films synthesized using HFCVD, with a particular focus on the influence of magnetic field adjustments. The primary aim was to explore the correlation between the structural characteristics of the films such as coating uniformity and thickness and their thermal responses under varying HFCVD parameters. The thermal properties of the films were measured using the thermal response time measurement method, which provided precise real-time data on the thermal behaviour of the materials. Temporal readings were accurately captured using Type-K thermocouples,

offering valuable insights into the dynamic heating processes of these diamond-coated wafers. The thermal performance of the coated wafers was systematically monitored by placing them on a hot plate consistently heated to 200°C. The study concentrated on the nuanced effects of coating uniformity, thickness, and specific HFCVD parameters on thermal behaviour. The primary objective was to assess how variables such as magnetic field orientation and rotational speed during deposition impact the heating efficiency and uniformity of the films. These factors are critically important in applications where effective heat dissipation is necessary.

5.5.1 Real-time thermal profiling of diamond coated silicon wafers to reach specified temperatures

Figure 5.16 presents comprehensive data on the time required to heat both a single edge and all edges of diamond films to a temperature of 200°C under different conditions, highlighting differences in heating times.

Figure 5.16a illustrates the heating times at zero rotational speed across various magnetic field orientations. Under the No Magnetic Field (NMF) condition, it takes 32 seconds to heat one edge to 200°C and 42 seconds to heat all edges, indicating a baseline thermal efficiency without magnetic influence. The South-South (SS) orientation shows a slight enhancement, requiring 28 seconds to heat one edge and 46 seconds to heat all edges. This suggests that even minimal magnetic influence can affect thermal dynamics. The South-North (SN) orientation exhibits the best performance at this speed, taking only 18 seconds to heat one edge and 30 seconds to heat all edges, indicating superior heat dispersion and efficiency.

Figure 5.16b explores the heating durations at a rotational speed of 1 rpm across different magnetic orientations. Under the NMF condition, the time to heat one edge decreases to 28 seconds, and to heat all edges, it takes 40 seconds, showing improved

heat transfer due to increased rotation. The SS orientation further decreases the time to 25 seconds for one edge and 44 seconds for all edges, indicating that the focused deposition of reactants at the edges may contribute to more efficient edge heating. The SN orientation consistently outperforms the others, with a heating time of just 18 seconds for one edge and 26 seconds for all edges, confirming its capability to achieve rapid and even heating across the wafer.

Figure 5.16c examines heating times at a higher rotational speed of 2 rpm across various magnetic orientations. Under the NMF condition, the heating efficiency improves, reducing the time to heat one edge to 26 seconds and all edges to 38 seconds. This reflects the positive impact of increased rotational speed on thermal dynamics. In the SS orientation, the heating time for one edge decreases to 24 seconds, and for all edges to 41 seconds, indicating a slight yet noticeable improvement in heating efficiency, particularly at the edges. The SN orientation once again demonstrates superior performance, requiring only 18 seconds to heat one edge and 25 seconds for all edges, showcasing its excellent thermal management and uniformity across different rotational speeds.

Figure 5.16d provides a comparative analysis of the variations in heating times under different magnetic field orientations and rotational speeds. The absence of a magnetic field (NMF) results in moderate unevenness in heating durations, although higher rotational speeds help improve uniformity. The SS orientation displays significant variations in heating times, suggesting inconsistencies in thermal distribution across the films. Conversely, the SN orientation shows minimal variation in heating times between one edge and all edges at all rotational speeds, affirming its ability to produce films with high uniformity and efficient heat distribution.

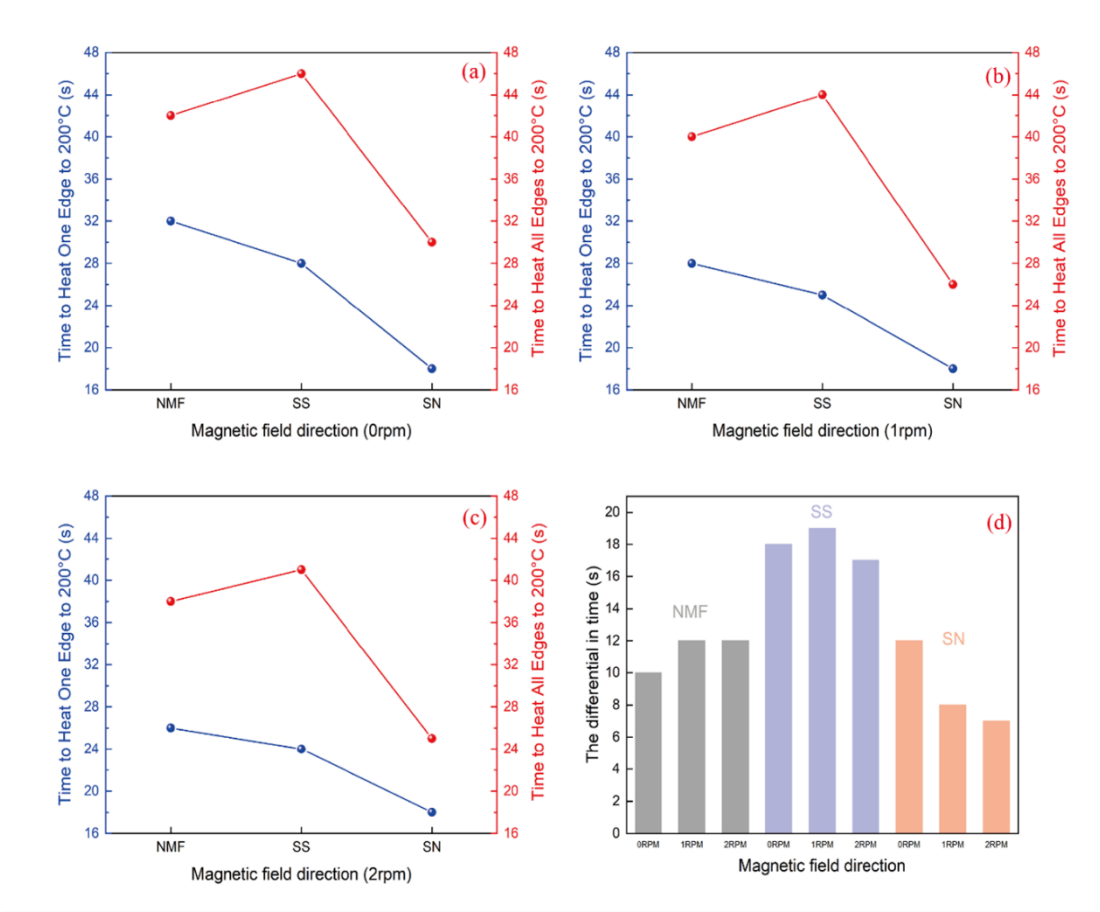

Figure 5.16 Time required to heat the workpiece to a temperature of 200°C for both one edge and all edges with different magnetic field orientations (a) 0 rpm; (b) 1 rpm; (c) 2 rpm; (d) Difference in heating times between MF-HFCVD conditions.

The experimental results highlight the substantial impact of magnetic field orientation and rotational speed on the heating efficiency and uniformity of diamond films synthesized using HFCVD. The South-North (SN) orientation consistently delivers superior performance by reducing heating times and achieving uniform temperatures across the substrate at all examined rotational speeds. This orientation effectively manages the distribution of thermal energy, ensuring optimal performance and consistency under varying conditions. The consistent success of the SN orientation

at different rotational speeds underscores its suitability for applications requiring precise thermal management.

5.6 Theoretical explanation of magnetic field and rotational effects on diamond film growth

The study of diamond film growth in MA-HFCVD systems provides a refined comprehension of the substantial impact of magnetic fields and rotational dynamics on the deposition process. This comprehensive theoretical perspective delves into the orientations of magnetic fields and rotational dynamics, thereby emphasizing their pivotal roles in the deposition of diamond films.

5.6.1 Influence of magnetic field orientation on deposition uniformity

The orientation of the external magnetic field in MA-HFCVD systems profoundly influences the physical and chemical processes essential for diamond film growth. Considering specific orientations, such as the South-South (S-S) and South-North (S-N), reveals how these configurations distinctly impact the behaviour and distribution of reactive species.

In the S-S orientation, a divergent magnetic field is created when like poles face each other, leading to a non-uniform distribution of magnetic field lines. This setup affects the trajectories and dynamics of both neutral radicals and charged plasma particles, causing a concentration of reactive species in localized areas. This can lead to uneven deposition rates and non-uniform film thickness across the substrate. The paramagnetic attraction forces in the S-S orientation cause spatial variability in radical species and plasma density, significantly influencing the growth regime and affecting the microstructural properties of the deposited diamond films. This explanation is accurate. The non-uniform magnetic field lines in an S-S configuration can indeed lead

to localized concentration of reactive species, resulting in non-uniform deposition. This is consistent with the principles of plasma physics and material deposition processes.

In the S-N orientation, a more uniform and direct magnetic field is generated when opposite poles are aligned, facilitating a homogeneous distribution of reactive species and charged particles across the substrate. This uniformity enhances the evenness of the chemical species flux and contributes to stable plasma conditions above the substrate. The uniformity in magnetic field distribution in the S-N orientation not only enhances the evenness of the chemical species flux but also contributes to stable plasma conditions above the substrate. This stability is crucial for achieving consistent diamond film growth, with uniform thickness and quality across the entire substrate surface. This is correct. A uniform magnetic field in an S-N configuration provides stable plasma conditions, leading to uniform deposition. This stability is crucial for achieving consistent diamond film growth.

5.6.2 Decomposition dynamics and radical generation

The decomposition dynamics and radical generation in HFCVD processes are intricately governed by the magnetic field orientation, significantly influenced by whether the setup is in an S-S or S-N orientation. The divergent magnetic field in the S-S orientation may lead to localized high-intensity areas where radical generation is amplified, but with a risk of non-uniform distribution across the substrate. This can result in areas of the substrate receiving a higher concentration of chemical species, potentially leading to localized overgrowth or variations in film properties. The divergent magnetic fields may lead to uneven distribution of chemical species, causing localized overgrowth or variations in film properties. This is accurate. Divergent magnetic fields can create localized hotspots for radical generation, leading to non-uniform film properties.

The introduction of rotational dynamics, particularly in the context of these magnetic field orientations, provides a dynamic mechanism for addressing the limitations inherent in static magnetic field configurations. For instance, a rotating magnetic field in an S-S oriented system can help mitigate the issue of localized radical concentration by continuously redistributing the plasma and reactive species. Similarly, in an S-N oriented system, rotational dynamics ensure that the uniform distribution of species is maintained throughout the deposition process, further enhancing the quality and uniformity of the diamond films.

The implementation of a rotational magnetic field, with its sweeping field lines, dynamically modulates the plasma properties, stimulating radical generation and ensuring a balanced distribution of chemical species and crystal defects. This dynamic approach, especially when applied in rotational frequencies between 1-2 rpm, effectively counters static field limitations, such as uneven distribution in the S-S orientation or potential stagnation in chemical species delivery in the S-N orientation.

In summary, the control of magnetic field orientation (S-S or S-N) combined with the application of rotational dynamics plays a crucial role in the MA-HFCVD process. This strategic approach allows for fine-tuning the deposition environment, leading to the synthesis of diamond films with enhanced uniformity and superior quality. By understanding and manipulating these parameters, it is possible to tailor the growth process to achieve specific desired properties in diamond films.

5.7 Summary

This study comprehensively investigates the impact of different static magnetic field orientations and rotational speeds on the growth and properties of diamond films synthesized using HFCVD. The findings highlight the substantial influence of these parameters on the uniformity, quality, and thermal properties of the diamond films.

The South-North (SN) magnetic field orientation consistently produced the most uniform diamond films, characterized by a homogeneous distribution of chemical precursors. This uniformity resulted in consistent film thickness and controlled grain size, attributed to enhanced precursor localization. Grain size dispersion was quantified using PDI, and the lowest centre-region PDI was obtained under SN at 2 rpm. This result confirms improved grain size uniformity at the wafer centre under SN with rotation. In contrast, the South-South (SS) setup exhibited significant thickness variations and edge irregularities, likely due to uneven precursor distribution caused by the divergent magnetic field. PDI results support reduced grain size uniformity under SS, with the highest edge-region PDI obtained under SS at 1 rpm. Introducing rotation to the SS configuration significantly mitigated these issues, promoting a more uniform distribution of chemical species and resulting in smoother film surfaces. In the NMF setup, rotation produced limited improvement at the wafer centre, while the wafer edge showed improved grain size uniformity at higher rotation speed based on PDI. The consistency of measurements across different speeds underscores the critical role of magnetic fields in achieving deposition uniformity in the HFCVD process. This finding emphasizes that magnetic assistance is essential for obtaining desired film characteristics, as the absence of a magnetic field fails to achieve the same level of uniformity.

Thermal distribution assessments further confirmed the superiority of the SN orientation in providing uniform and efficient heat distribution during the HFCVD process, which is vital for applications requiring precise thermal control. Films grown under the SN orientation exhibited optimal thermal properties, ensuring consistent heat management. Although the SS orientation initially struggled with thermal uniformity, the introduction of rotational dynamics improved both thermal distribution and film

quality. This highlights the synergistic effect of combining rotation with specific magnetic field orientations to enhance film properties.

Overall, this study conclusively demonstrates that magnetic field orientation and rotational parameters play a crucial role in the HFCVD process, significantly affecting the uniformity, quality, and thermal behaviour of the synthesized diamond films. Specifically, the SN orientation combined with controlled rotation yields the most favourable results, showing promise for achieving highly controlled film properties. These advancements are essential for the integration of diamond films into specialized high-tech applications, where uniformity, quality, and precise thermal management are critical, thereby expanding the applicability of this technology within advanced industries.

Chapter 6 Conclusions and suggestions for future work

6.1 Conclusions

Diamond films have numerous applications in various industries such as electronics, optics, wear-resistant coatings, and thermal management systems. Traditional methods of diamond film deposition face challenges in terms of uniformity, quality, and efficiency. This thesis addresses these issues by exploring innovative approaches to HFCVD with a focus on magnetic field assistance and rotational dynamics. The main contributions and findings of this research are summarized as follows:

Incorporating magnetic field assistance in the HFCVD process has notably improved the uniformity and quality of diamond films. The South-North (SN) magnetic field orientation was identified as the most effective configuration, promoting uniform grain size and consistent coating thickness across the substrate. This enhancement is attributed to the optimized distribution of chemical species and improved plasma stability under the SN orientation.

Introducing rotational dynamics to the magnetic field system further refined the deposition process. Rotating the magnetic field around the stationary substrate significantly improved the uniformity of diamond films. The study showed that rotational speeds of 0 RPM, 1 RPM, and 2 RPM influenced the deposition process, with higher rotational speeds contributing to more uniform grain size and coating thickness. This dynamic approach mitigates the limitations of static magnetic field configurations and enhances film quality.

The studies confirmed that diamond films deposited with magnetic assistance exhibit superior thermal conductivity properties. This finding is pivotal for applications in thermal management systems where efficient heat dissipation is critical. The

improved thermal properties are linked to the enhanced structural uniformity and reduced defects within the diamond films.

These findings provide a comprehensive understanding of the interplay between magnetic fields, rotational dynamics, and HFCVD process parameters. The research highlights the potential for tailored diamond film properties through controlled adjustments of these factors, paving the way for advanced applications in various industrial contexts, including cutting tools, thermal management systems, and wear-resistant coatings.

6.2 Suggestions for the future work

In this study, the focus was on investigating the impact of different static magnetic field orientations and rotational dynamics on the growth and properties of diamond films deposited using HFCVD. The findings have significantly enhanced our understanding of how magnetic fields can influence film uniformity, grain size, and thermal properties. However, to further advance this field and broaden the applications of diamond films, several areas warrant further exploration.

Firstly, exploring the effects of open-field and closed-field magnetic configurations in the HFCVD process presents a promising avenue for future research. Open-field configurations, where magnetic field lines extend outward and are not confined within the deposition chamber, may interact differently with the plasma and reactive species compared to closed-field configurations, where magnetic field lines loop back into the chamber. Investigating these configurations could provide deeper insights into how magnetic fields can be optimized to control film growth, uniformity, and properties. Understanding the influence of these magnetic field topologies on the distribution of chemical species and energy within the deposition environment is crucial for fine-tuning the HFCVD process.

Secondly, diamond films offer a route to improved cutting-tool durability and thermal management due to their high hardness and thermal conductivity. Future work should apply the optimized HFCVD conditions developed in this thesis to coat cutting tools under magnetic-field-assisted operation, explicitly comparing open-field and closed-field configurations. Building on prior demonstrations of MCD/NCD coatings for PCB drilling using conventional HFCVD, extending to magnetic-assisted configurations will enable controlled evaluation of wear progression, cutting efficiency, and process-dependent failure modes under industrially relevant conditions.

In addition, the effect of magnetic-field strength/orientation and substrate rotation on film substrate adhesion should be quantified. Translating improvements in thickness uniformity and microstructural control into reliable tool performance requires a direct assessment of interfacial integrity under the same process conditions. Adhesion should be quantified using Rockwell A indentation across the full parameter matrix (e.g., 0 mT, intermediate levels, and 400 mT; SN vs SS; 0, 1, and 2 RPM), evaluated using both qualitative failure-mode ranking and quantitative measurements such as crack radius and delamination/spallation diameter. To complement Rockwell indentation, progressive-load scratch testing should be used to extract critical loads for cohesive and adhesive failure and to distinguish interfacial delamination from near-surface cracking. These adhesion metrics should then be correlated with coating thickness, grain-size statistics, thickness non-uniformity, and tool wear performance.

Additionally, extending the research to include substrates with different magnetic properties, such as paramagnetic and non-magnetic materials, will help determine the versatility of the magnetic field-assisted HFCVD process. Understanding how these substrates interact with both open-field and closed-field magnetic configurations and influence the deposition process is essential for expanding the range

of potential applications. This includes assessing how magnetic susceptibility and permeability of the substrates affect the growth kinetics and film adherence.

Furthermore, investigating the deposition of diamond films on irregularly shaped substrates is another important area for future research. Adapting the HFCVD process to coat complex geometries uniformly, especially under different magnetic field configurations, is critical for many industrial applications. This would involve studying the effects of magnetic field-assisted deposition on three-dimensional substrates and developing techniques to achieve consistent film quality over intricate surfaces.

Moreover, integrating magnetic field-assisted HFCVD processes with other deposition techniques could open new possibilities for tailoring diamond film properties. For instance, combining magnetic fields with plasma-enhanced CVD methods may enhance film deposition rates and quality. Investigating the synergistic effects of such hybrid processes could lead to advanced methods for producing diamond films with customized properties.

Finally, considering the scalability of magnetic field-assisted HFCVD processes for industrial applications is essential. Future work should address challenges associated with scaling up the process, including the design of magnetic field systems suitable for large-area or high-throughput deposition. Optimizing process parameters to maintain film quality at larger scales, while ensuring energy efficiency and cost-effectiveness, will be vital for the commercial viability of this technology.

In conclusion, by exploring these areas such as the impact of open-field and closed-field magnetic configurations, application to cutting tools, substrate versatility, coating of irregular geometries, integration with other techniques, and future research

can significantly contribute to the advancement of diamond film deposition technologies and their industrial applications.

Reference

Allen, R. D., Glasier Jr, L. F., & Jordan, P. L. (1960). Spectral emissivity, total emissivity, and thermal conductivity of molybdenum, tantalum, and tungsten above 2300 K. *Journal of Applied Physics*, *31*(8), 1382–1387.

Asmussen, J., & Reinhard, D. K. (2002). Diamond Films Handbook. In *Diamond Films Handbook*. https://doi.org/10.1201/9780203910603

Auciello, O., & Aslam, D. M. (2021). Review on advances in microcrystalline, nanocrystalline and ultrananocrystalline diamond films-based micro/nano-electromechanical systems technologies. *Journal of Materials Science*, *56*, 7171–7230.

Auciello, O., & Sumant, A. V. (2010). Status review of the science and technology of ultrananocrystalline diamond (UNCD^{TM}) films and application to multifunctional devices. *Diamond and Related Materials*, *19*(7–9), 699–718.

Barnes, D., Johnson, S., Snell, R., & Best, S. (2012). Using scratch testing to measure the adhesion strength of calcium phosphate coatings applied to poly(carbonate urethane) substrates. *Journal of the Mechanical Behavior of Biomedical Materials*, *6*, 128–138. https://doi.org/10.1016/j.jmbbm.2011.10.010

Bian, R., Ferraris, E., Ynag, Y., & Qian, J. (2018). Experimental investigation on ductile mode micro-milling of ZrO2 ceramics with diamond-coated end mills. *Micromachines*, *9*(3). https://doi.org/10.3390/mi9030127

Bohlmark, J., Blomqvist, H., Landälv, L., Amerioun, S., & Ahlgren, M. (2011). Evaluation of arc evaporated coatings on rounded surfaces and sharp edges. *Materials Science Forum*, *681*, 145–150.

Broitman, E. (2017). Indentation Hardness Measurements at Macro-, Micro-, and Nanoscale: A Critical Overview. *Tribology Letters*, *65*(1), 1–18.

https://doi.org/10.1007/s11249-016-0805-5

Cabral, G., Gäbler, J., Lindner, J., Grácio, J., & Polini, R. (2008). A study of diamond film deposition on WC-Co inserts for graphite machining: Effectiveness of SiC interlayers prepared by HFCVD. *Diamond and Related Materials*, *17*(6), 1008–1014. https://doi.org/10.1016/j.diamond.2008.03.017

Chattopadhyay, A., Sarangi, S. K., & Chattopadhyay, A. K. (2008). Effect of negative dc substrate bias on morphology and adhesion of diamond coating synthesised on carbide turning tools by modified HFCVD method. *Applied Surface Science*, *255*(5 PART 1), 1661–1671. https://doi.org/10.1016/j.apsusc.2008.04.065

Chen, N., Shen, B., Yang, G., & Sun, F. (2013). Tribological and cutting behavior of silicon nitride tools coated with monolayer- and multilayer-microcrystalline HFCVD diamond films. *Applied Surface Science*, *265*, 850–859. https://doi.org/10.1016/j.apsusc.2012.11.133

Chengyong, W., Lijuan, Z., Xin, H., Shan, L., Bingmiao, L., Hongqun, T., Bing, W., & Lipeng, Y. (2016). *Research on Printed Circuit Board Mechanical Drilling*. *4*(59), 14–25.

Chou, C. C., Lee, J. W., & Chen, Y. I. (2008). Tribological and mechanical properties of HFCVD diamond-coated WC-Co substrates with different Cr interlayers. *Surface and Coatings Technology*, *203*(5–7), 704–708. https://doi.org/10.1016/j.surfcoat.2008.08.055

Codina, R., Principe, J., & Ávila, M. (2010). Finite element approximation of turbulent thermally coupled incompressible flows with numerical sub-grid scale modelling. *International Journal of Numerical Methods for Heat & Fluid Flow*, *20*(5), 492–516.

Contreras, O., Hirata, G. A., & Avalos-Borja, M. (2000). Interface analysis of CVD

diamond on TiN surfaces. *Applied Surface Science*, *158*(3), 236–245. https://doi.org/10.1016/S0169-4332(00)00014-3

Cui, J. B., & Fang, R. C. (1996). The influence of bias on gaseous composition and diamond growth in a hot-filament chemical vapour deposition process. *Journal of Physics D: Applied Physics*, *29*(11), 2759–2762. https://doi.org/10.1088/0022-3727/29/11/006

Das, D., & Singh, R. N. (2007). A review of nucleation, growth and low temperature synthesis of diamond thin films. *International Materials Reviews*, *52*(1), 29–64. https://doi.org/10.1179/174328007X160245

Dawedeit, C., Kucheyev, S. O., Shin, S. J., Willey, T. M., Bagge-Hansen, M., Braun, T., Wang, Y. M., El-Dasher, B. S., Teslich, N. E., Biener, M. M., Ye, J., Kirste, L., Roehlig, C. C., Wolfer, M., Woerner, E., Van Buuren, A. W., Hamza, A. V., Wild, C., & Biener, J. (2013). Grain size dependent physical and chemical properties of thick CVD diamond films for high energy density physics experiments. *Diamond and Related Materials*, *40*, 75–81. https://doi.org/10.1016/j.diamond.2013.10.001

Deuerler, F., Van Den Berg, H., Tabersky, R., Freundlieb, A., Pies, M., & Buck, V. (1996). Pretreatment of substrate surface for improved adhesion of diamond films on hard metal cutting tools. *Diamond and Related Materials*, *5*(12), 1478–1489. https://doi.org/10.1016/S0925-9635(96)00569-9

Dumpala, R., Chandran, M., Madhavan, S., Ramamoorthy, B., & Rao, M. S. R. (2015). High wear performance of the dual-layer graded composite diamond coated cutting tools. *International Journal of Refractory Metals and Hard Materials*, *48*, 24–30. https://doi.org/10.1016/j.ijrmhm.2014.07.023

Dumpala, R., Chandran, M., & Ramachandra Rao, M. S. (2015). Engineered CVD

Diamond Coatings for Machining and Tribological Applications. *Jom*, *67*(7), 1565–1577. https://doi.org/10.1007/s11837-015-1428-2

Dumpala, R., Kumar, N., Kumaran, C. R., Dash, S., Ramamoorthy, B., & Rao, M. S. R. (2014). Adhesion characteristics of nano- and micro-crystalline diamond coatings: Raman stress mapping of the scratch tracks. *Diamond and Related Materials*, *44*, 71–77. https://doi.org/10.1016/j.diamond.2014.02.007

Ferraris, E., Vleugels, J., Guo, Y., Bourell, D., Kruth, J. P., & Lauwers, B. (2016). Shaping of engineering ceramics by electro, chemical and physical processes. *CIRP Annals - Manufacturing Technology*, *65*(2), 761–784. https://doi.org/10.1016/j.cirp.2016.06.001

Francis, L. F., Stadler, B. J. H., & Roberts, C. C. (2016). *Ceramics and Polymers* (Issue Chapter 7).

Gäbler, J., Schäfer, L., & Westermann, H. (2000). Chemical vapour deposition diamond coated microtools for grinding, milling and drilling. *Diamond and Related Materials*, *9*(3–6), 921–924. https://doi.org/10.1016/S0925-9635(99)00278-2

Gaydaychuk, A., Zenkin, S., & Linnik, S. (2019). Influence of Al-Si-N interlayer on residual stress of CVD diamond coatings. *Surface and Coatings Technology*, *357*(March 2018), 348–352. https://doi.org/10.1016/j.surfcoat.2018.10.030

Gracio, J. J., Fan, Q. H., & Madaleno, J. C. (2010). Diamond growth by chemical vapour deposition. *Journal of Physics D: Applied Physics*, *43*(37). https://doi.org/10.1088/0022-3727/43/37/374017

Handschuh-Wang, S., Wang, T., & Tang, Y. (2021). Ultrathin Diamond Nanofilms—Development, Challenges, and Applications. *Small*, *17*(30), 2007529. https://doi.org/https://doi.org/10.1002/smll.202007529

Haubner, R., & Kalss, W. (2010). Diamond deposition on hardmetal substrates - Comparison of substrate pre-treatments and industrial applications. *International Journal of Refractory Metals and Hard Materials*, *28*(4), 475–483. https://doi.org/10.1016/j.ijrmhm.2010.03.004

Hojman, E., Akhvlediani, R., Layyous, A., & Hoffman, A. (2013). Diamond CVD film formation onto WC-Co substrates using a thermally nitrided Cr diffusion-barrier. *Diamond and Related Materials*, *39*, 65–72. https://doi.org/10.1016/j.diamond.2013.08.002

Hu, N., Wang, Y., Li, J., Wei, Q., Jiang, Y., Ma, L., Yu, Z., Zhou, K., & Long, H. (2019). Manipulation of nanostructured carbon films as field emitters in an electric-and-magnetic-field-assisted chemical vapor deposition process. *Surface and Coatings Technology*, *359*(August 2018), 459–467. https://doi.org/10.1016/j.surfcoat.2018.12.048

Huang, X., Wang, C., Yang, T., He, Y., Li, Y., & Zheng, L. (2020). Wear characteristics of micro-drill during ultra-high speed drilling multilayer PCB consisting of copper foil and ceramic particle filled GFRPs. *Procedia CIRP*, *101*, 326–329. https://doi.org/10.1016/j.procir.2020.10.007

Kanaya, K., & Kawakatsu, H. (1972). Secondary electron emission due to primary and backscattered electrons. *Journal of Physics D: Applied Physics*, *5*(9), 1727.

Kanda, K., Takehana, S., Yoshida, S., Watanabe, R., Takano, S., Ando, H., & Shimakura, F. (1995). Application of diamond-coated cutting tools. *Surface and Coatings Technology*, *73*(1–2), 115–120. https://doi.org/10.1016/0257-8972(94)02370-0

Kao, W. H., Su, Y. L., Yao, S. H., & Huang, H. C. (2010). Optimizing the tribological properties and high-speed drilling performance of a-C:H coatings via nitrogen

addition. *Surface and Coatings Technology*, *204*(8), 1277–1287. https://doi.org/10.1016/j.surfcoat.2009.10.016

Kim, Y.-C., & Kang, S.-J. L. (2011). Novel CVD diamond-coated conditioner for improved performance in CMP processes. *International Journal of Machine Tools and Manufacture*, *51*(6), 565–568. https://doi.org/https://doi.org/10.1016/j.ijmachtools.2011.02.008

Kromka, A., Babchenko, O., Potocky, S., Rezek, B., Sveshnikov, A., Demo, P., Izak, T., & Varga, M. (2013). Diamond nucleation and seeding techniques for tissue regeneration. In *Diamond-Based Materials for Biomedical Applications*. Woodhead Publishing Limited. https://doi.org/10.1533/9780857093516.2.206

Kubečka, M., Obrusník, A., Zikán, P., Jilek Jr, M., Vencels, J., & Bonaventura, Z. (2019). Predictive simulation of antenna effect in PVD processes using fluid models. *Surface and Coatings Technology*, *379*, 125045.

Kumar Mallik, A., Bhar, R., & Bysakh, S. (2016). An effort in planarising microwave plasma CVD grown polycrystalline diamond (PCD) coated 4in. Si wafers. *Materials Science in Semiconductor Processing*, *43*, 1–7. https://doi.org/https://doi.org/10.1016/j.mssp.2015.11.016

Kwok, F. M., Du, X., Sun, Z., Ng, M. C., Liu, Q., Luo, F. L., Yip, W. S., Kwok, D. K. Y., & To, S. (2024). Fabrication of diamond film under low methane concentration by hot filament chemical vapor deposition with magnetic field assistance. *Surface and Coatings Technology*, *483*, 130802.

Kwok, F. M., Sun, Z., Yip, W. S., Kwok, K. Y. D., & To, S. (2022). Effects of Coating Parameters of Hot Filament Chemical Vapour Deposition on Tool Wear in Micro-Drilling of High-Frequency Printed Circuit Board. *Processes*, *10*(8). https://doi.org/10.3390/pr10081466

Lee, D. H., Park, H. J., & Ligrani, P. (2012). Milliscale confined impinging slot jets: Laminar heat transfer characteristics for an isothermal flat plate. *International Journal of Heat and Mass Transfer*, *55*(9–10), 2249–2260.

Lei, X. L., He, Y., & Sun, F. H. (2016). OPTIMIZATION of CVD DIAMOND COATING TYPE on MICRO DRILLS in PCB MACHINING. *Surface Review and Letters*, *23*(2), 1–8. https://doi.org/10.1142/S0218625X15501085

Lei, X., Shen, B., Cheng, L., Sun, F., & Chen, M. (2014). Influence of pretreatment and deposition parameters on the properties and cutting performance of NCD coated PCB micro drills. *International Journal of Refractory Metals and Hard Materials*, *43*, 30–41. https://doi.org/10.1016/j.ijrmhm.2013.10.016

Li, J., Wang, Y., Wei, Q., Xie, Y., Long, H., Deng, Z., Ma, L., Yu, Z., Jiang, Y., Hu, N., & Zhou, K. (2017). Plasma-enhanced synthesis of carbon nanocone arrays by magnetic and electric fields coupling HFCVD. *Surface and Coatings Technology*, *324*, 413–418. https://doi.org/10.1016/j.surfcoat.2017.06.008

Li, X., Li, C., Chen, C., Liu, C., Lyu, F., Jiang, M., & Hu, X. (2019). Adherent and smooth diamond film deposited on stainless steel by using AlSiN interlayers. *Applied Surface Science*, *487*(May), 464–472. https://doi.org/10.1016/j.apsusc.2019.05.084

Liang, X., Wang, L., Zhu, H., & Yang, D. (2007). Effect of pressure on nanocrystalline diamond films deposition by hot filament CVD technique from CH4/H2 gas mixture. *Surface and Coatings Technology*, *202*(2), 261–267. https://doi.org/10.1016/j.surfcoat.2007.05.032

Liang, Y., & Dutta, S. P. (2001). Application trend in advanced ceramic technologies. *Technovation*, *21*(1), 61–65. https://doi.org/10.1016/S0166-4972(00)00019-5

Little, R. B., Wang, X., & Goddard, R. (2005). Nano-diamond synthesis in strong

magnetic field. *Journal of Cluster Science*, *16*(1), 53–63. https://doi.org/10.1007/s10876-005-2715-9

Liu, H., & Dandy, D. S. (1995). Diamond Nucleation Mechanisms. *Diamond Chemical Vapor Deposition*, 46–78. https://doi.org/10.1016/b978-081551380-3.50005-0

Liu, X., Shi, H., Huang, G., Tao, S., & Gao, Z. (2020). Investigation on Drill Wear and Micro Hole Quality in High Speed Drilling of High Frequency Printed Circuit Board. *IOP Conference Series: Materials Science and Engineering*, *825*(1). https://doi.org/10.1088/1757-899X/825/1/012034

Liu, X., Wen, K., Duan, X., Wang, C., & Long, H. (2023). CVD Diamond Growth Enhanced by a Dynamic Magnetic Field. *Coatings*, *13*(2), 441.

Locher, R., Wild, C., Herres, N., Behr, D., & Koidl, P. (1994). Nitrogen stabilized ⟨100⟩ texture in chemical vapor deposited diamond films. In *Applied Physics Letters* (Vol. 65, Issue 1, pp. 34–36). https://doi.org/10.1063/1.113064

Long, H., Li, S., Luo, H., Wang, Y., Wei, Q. P., & Yu, Z. M. (2015). The effect of periodic magnetic field on the fabrication and field emission properties of nanocrystalline diamond films. *Applied Surface Science*, *353*, 548–552. https://doi.org/10.1016/j.apsusc.2015.06.151

Lu, P., Gomez, H., Xiao, X., Lukitsch, M., Durham, D., Sachdeve, A., Kumar, A., & Chou, K. (2013). Coating thickness and interlayer effects on CVD-diamond film adhesion to cobalt-cemented tungsten carbides. *Surface and Coatings Technology*, *215*, 272–279. https://doi.org/10.1016/j.surfcoat.2012.08.093

Lu, P., Xiao, X., & Chou, Y. K. (2014). Interface delamination study of diamond-coated carbide tools considering coating fractures. *Surface and Coatings Technology*, *260*, 239–245. https://doi.org/10.1016/j.surfcoat.2014.08.080

Macak, E. B., Münz, W.-D., & Rodenburg, J. M. (2003). Plasma–surface interaction at

sharp edges and corners during ion-assisted physical vapor deposition. Part I: Edge-related effects and their influence on coating morphology and composition. *Journal of Applied Physics*, *94*(5), 2829–2836.

Marton, M., Ižák, T., Veselý, M., Vojs, M., Michalka, M., & Bruncko, J. (2007). Effect of argon and substrate bias on diamond thin film surface morphology. *Vacuum*, *82*(2 SPEC. ISS.), 154–157. https://doi.org/10.1016/j.vacuum.2007.07.008

May, P. W. (2000). Diamond Thin Films: A 21st-Century Material. *Philosophical Transactions: Mathematical, Physical and Engineering Sciences*, *358*(1766), 473–495. http://www.jstor.org/stable/2666865

May, P. W., Everitt, N. M., Trevor, C. G., Ashfold, M. N. R., & Rosser, K. N. (1993). Diamond deposition in a hot-filament reactor using different hydrocarbon precursor gases. *Applied Surface Science*, *68*(3), 299–305. https://doi.org/10.1016/0169-4332(93)90249-B

Montes-Gutiérrez, J. A., Alcantar-Peña, J. J., de Obaldia, E., Zúñiga-Rivera, N. J., Chernov, V., Meléndrez-Amavizca, R., Barboza-Flores, M., Garcia-Gutierrez, R., & Auciello, O. (2018). Afterglow, thermoluminescence and optically stimulated luminescence characterization of micro-, nano-and ultrananocrystalline diamond films grown on silicon by HFCVD. *Diamond and Related Materials*, *85*, 117–124.

Moustakas, T. D. (1989). The role of the tungsten filament in the growth of polycrystalline diamond films by filament-assisted CVD of hydrocarbons. *Solid State Ionics*, *32–33*(PART 2), 861–868. https://doi.org/10.1016/0167-2738(89)90368-8

Piconi, C., & Maccauro, G. (1999). Zirconia as a ceramic biomaterial. *Biomaterials*, *20*(1), 1–25.

Polini, R. (2006). Chemically vapour deposited diamond coatings on cemented

tungsten carbides: Substrate pretreatments, adhesion and cutting performance. *Thin Solid Films*, *515*(1), 4–13. https://doi.org/10.1016/j.tsf.2005.12.042

Polini, R., Barletta, M., & Cristofanilli, G. (2010). Wear resistance of nano- and micro-crystalline diamond coatings onto WC-Co with Cr/CrN interlayers. *Thin Solid Films*, *519*(5), 1629–1635. https://doi.org/10.1016/j.tsf.2010.07.128

Polini, R., D'Antonio, P., Lo Casto, S., Ruisi, V. F., & Traversa, E. (2000). Cutting performance and indentation behaviour of diamond films on Co-cemented tungsten carbide. *Surface and Coatings Technology*, *123*(1), 78–83. https://doi.org/10.1016/S0257-8972(99)00471-5

Polini, R., Mantini, F. P., Barletta, M., Valle, R., & Casadei, F. (2006). Hot filament chemical vapour deposition and wear resistance of diamond films on WC-Co substrates coated using PVD-arc deposition technique. *Diamond and Related Materials*, *15*(9), 1284–1291. https://doi.org/10.1016/j.diamond.2005.09.045

Raghuveer, M. S., Yoganand, S. N., Jagannadham, K., Lemaster, R. L., & Bailey, J. (2002). Improved CVD diamond coatings on WC-Co tool substrates. *Wear*, *253*(11–12), 1194–1206. https://doi.org/10.1016/S0043-1648(02)00244-2

Roy, M., George, V. C., Dua, A. K., Raj, P., Schulze, S., Tenne, D. A., Salvan, G., & Zahn, D. R. T. (2002). Feed gas dependence of the surface nanophase on HFCVD grown diamond films studied by surface enhanced Raman spectroscopy. *Applied Surface Science*, *191*(1–4), 334–337.

Schwander, M., & Partes, K. (2011). A review of diamond synthesis by CVD processes. *Diamond and Related Materials*, *20*(9), 1287–1301. https://doi.org/https://doi.org/10.1016/j.diamond.2011.08.005

Sein, H., Ahmed, W., Rego, C. A., Jones, A. N., Amar, M., Jackson, M., & Polini, R. (2003). CVD diamond coating on WC dental cutting tools. *J. Phys.: Condens.*

Matter, *15*, S2961–S2967.

Shen, B., & Sun, F. (2009). Deposition and friction properties of ultra-smooth composite diamond films on Co-cemented tungsten carbide substrates. *Diamond and Related Materials*, *18*(2–3), 238–243. https://doi.org/10.1016/j.diamond.2008.10.053

Shen, X., Wang, X., Sun, F., & Ding, C. (2017). Sandblasting pretreatment for deposition of diamond films on WC-Co hard metal substrates. *Diamond and Related Materials*, *73*, 7–14. https://doi.org/10.1016/j.diamond.2016.10.025

Shi, H., Liu, X., & Lou, Y. (2019). Materials and micro drilling of high frequency and high speed printed circuit board: a review. *International Journal of Advanced Manufacturing Technology*, *100*(1–4), 827–841. https://doi.org/10.1007/s00170-018-2711-5

Song, C. W., Lee, Y. H., Heo, S. Y., Hwang, N.-M., Choi, S., & Kim, K. H. (2017). Computer simulation of temperature parameter for diamond formation by using hot-filament chemical vapor deposition. *Coatings*, *8*(1), 15.

Taher, M. A., Schmidt, W. F., Brown, W. D., Nasrazadani, S., Nasseem, H. A., & Malshe, A. P. (1996). Effect of methane concentration on mechanical properties of HFCVD diamond-coated cemented carbide tool inserts. *Surface and Coatings Technology*, *86–87*(PART 2), 678–685. https://doi.org/10.1016/S0257-8972(96)03062-9

Takeuchi, S., Oda, S., & Murakawa, M. (2001). Synthesis of multilayer diamond film and evaluation of its mechanical properties. *Thin Solid Films*, *398*(399), 238–243. https://doi.org/10.1016/S0040-6090(01)01499-7

Tang, J., Xiong, J., Guo, Z., Yang, T., Liang, M., Yang, W., Liu, J., & Zheng, Q. (2016). Microstructure and properties of CVD coated on gradient cemented carbide with

different WC grain size. *International Journal of Refractory Metals and Hard Materials*, *61*, 128–135. https://doi.org/10.1016/j.ijrmhm.2016.09.003

Thomas, E. L. H., Nelson, G. W., Mandal, S., Foord, J. S., & Williams, O. A. (2014). Chemical mechanical polishing of thin film diamond. *Carbon*, *68*, 473–479. https://doi.org/https://doi.org/10.1016/j.carbon.2013.11.023

Umezawa, H., Nagase, M., Kato, Y., & Shikata, S. (2012). High temperature application of diamond power device. *Diamond and Related Materials*, *24*, 201–205.

Van der Drift, A. (1967). Evolutionary selection, a principle governing growth orientation in vapour-deposited layers. *Philips Res. Rep*, *22*(3), 267.

Vidakis, N., Antoniadis, A., & Bilalis, N. (2003). The VDI 3198 indentation test evaluation of a reliable qualitative control for layered compounds. *Journal of Materials Processing Technology*, *143–144*(1), 481–485. https://doi.org/10.1016/S0924-0136(03)00300-5

Wang, H., Wang, C., Wang, X., & Sun, F. (2021). Effects of carbon concentration and gas pressure with hydrogen-rich gas chemistry on synthesis and characterizations of HFCVD diamond films on WC-Co substrates. *Surface and Coatings Technology*, *409*(October 2020), 126839. https://doi.org/10.1016/j.surfcoat.2021.126839

Wang, X., Shen, X., Sun, F., & Shen, B. (2016). Mechanical properties and solid particle erosion of MCD films synthesized using different carbon sources by BE-HFCVD. *International Journal of Refractory Metals and Hard Materials*, *54*, 370–377. https://doi.org/10.1016/j.ijrmhm.2015.09.004

Wang, X., Zhao, T., Sun, F., & Shen, B. (2015). Comparisons of HFCVD diamond nucleation and growth using different carbon sources. *Diamond and Related*

Materials, *54*(1), 26–33. https://doi.org/10.1016/j.diamond.2014.11.009

Wang, Y., Li, J., Hu, N., Jiang, Y., Wei, Q., Yu, Z., Long, H., Zhu, H., Xie, Y., & Ma, L. (2018). Effect of magnetic and electric coupling fields on micro-and nano-structure of carbon films in the CVD diamond process and their electron field emission property. *Materials Research Express*, *5*(3), 35009.

Wang, Y., Li, J., Hu, N., Jiang, Y., Wei, Q., Yu, Z., Long, H., Zhu, H., Xie, Y., Ma, L., Lin, C. Te, & Su, W. (2018). Effect of magnetic and electric coupling fields on micro- and nano- structure of carbon films in the CVD diamond process and their electron field emission property. *Materials Research Express*, *5*(3). https://doi.org/10.1088/2053-1591/aab11b

Wang, Y., Li, J., Long, H., Luo, H., Zhou, B., Xie, Y., Li, S., Wei, Q., & Yu, Z. (2016). A periodic magnetic field assisted chemical vapor deposition technique to fabricate diamond film with preferred orientation. *Surface and Coatings Technology*, *292*, 49–53.

Wang, Y., Wei, Q., Yu, Z., Long, H., Deng, Z., Xie, Y., Li, J., Lin, C.-T., Ma, L., & Zhou, K. (2017). Field emission properties of the caterpillar-like structural carbon film grown by magnetic and electric fields coupling HFCVD. *Applied Surface Science*, *423*, 788–792.

Wang, Y., Zou, B., & Yin, G. (2019). Wear mechanisms of Ti(C7N3)-based cermet micro-drill and machining quality during ultra-high speed micro-drilling multi-layered PCB consisting of copper foil and glass fiber reinforced plastics. *Ceramics International*, *45*(18), 24578–24593. https://doi.org/10.1016/j.ceramint.2019.08.187

Watanabe, H., Tsuzaka, H., & Masuda, M. (2008). Microdrilling for printed circuit boards (PCBs)-Influence of radial run-out of microdrills on hole quality. *Precision*

Engineering, *32*(4), 329–335. https://doi.org/10.1016/j.precisioneng.2008.02.004

Wen, B., Li, T., Dong, C., Zhang, X., Yao, S., Cao, Z., Wang, D., Ji, S., & Jin, J. (2003). Preparation of diamond nanocrystals from catalysed carbon black in a high magnetic field. *Journal of Physics Condensed Matter*, *15*(46), 8049–8054. https://doi.org/10.1088/0953-8984/15/46/019

Wild, C., Herres, N., & Koidl, P. (1990). Texture formation in polycrystalline diamond films. *Journal of Applied Physics*, *68*(3), 973–978. https://doi.org/10.1063/1.346663

Wu, X., Yu, Z., You, X., Tian, M., & Gong, Y. (2012). Characterization of diamond films deposited on Re substrate by magnetic field-assisted hot filament chemical vapor deposition. *Applied Surface Science*, *258*(6), 2117–2120.

Xu, F., Xu, J. H., Yuen, M. F., Zheng, L., Lu, W. Z., & Zuo, D. W. (2013). Adhesion improvement of diamond coatings on cemented carbide with high cobalt content using PVD interlayer. *Diamond and Related Materials*, *34*, 70–75. https://doi.org/10.1016/j.diamond.2013.01.012

Yan, G., Wu, Y., Cristea, D., Lu, F., Wang, Y., Zhao, D., Tierean, M., & Liu, L. (2019). Machining performance of hard-brittle materials by multi-layer micro-nano crystalline diamond coated tools. *Results in Physics*, *13*(March), 102303. https://doi.org/10.1016/j.rinp.2019.102303

Yang, Q., Zhao, J., Huang, Y., Zhu, X., Fu, W., Li, C., & Miao, J. (2019). A diamond made microchannel heat sink for high-density heat flux dissipation. *Applied Thermal Engineering*, *158*, 113804.

Ye, F., Li, Y., Sun, X., Yang, Q., Kim, C. Y., & Odeshi, A. G. (2016). CVD diamond coating on WC-Co substrate with Al-based interlayer. *Surface and Coatings Technology*, *308*, 121–127. https://doi.org/10.1016/j.surfcoat.2016.06.088

You, X., Yu, Z., Shi, L., & Wang, L. (2009). Influence of periodic magnetic field on the growth of CVD diamond films at lower temperature. *Journal of Crystal Growth*, *311*(23–24), 4675–4678. https://doi.org/10.1016/j.jcrysgro.2009.09.019

Yu, J., Huang, R., Wen, L., & Shi, C. (1997). Enhancement of the HFCVD diamond growth process by directed gas flow. *Materials Letters*, *32*(2–3), 143–146.

Yuan, Z., Guo, Y., Li, C., Liu, L., Yang, B., Song, H., Zhai, Z., Lu, Z., Li, H., Staedler, T., Huang, N., & Jiang, X. (2020). New multilayered diamond/β-SiC composite architectures for high-performance hard coating. *Materials and Design*, *186*, 108207. https://doi.org/10.1016/j.matdes.2019.108207

Zhang, B., & Zhou, L. (1997). Effect of sandblasting on adhesion strength of diamond coatings. *Thin Solid Films*, *307*(1–2), 21–28. https://doi.org/10.1016/S0040-6090(97)00297-6

Zhang, T., Feng, Q., Yu, Z., Zhang, L., & Sun, F. (2019). Effect of mechanical pretreatment on nucleation and growth of HFCVD diamond films on cemented carbide tools with a complex shape. *International Journal of Refractory Metals and Hard Materials*, *84*(June), 105016. https://doi.org/10.1016/j.ijrmhm.2019.105016

Zhang, W., Lu, C., Ge, M., Bu, F., & Zhang, J. (2020). Surface modified and gradation-mixed Al2O3 as an effective filler for the polyphenylene oxide (PPO) insulative layer in copper clad laminates. *Journal of Materials Science: Materials in Electronics*, *31*(23), 21602–21616. https://doi.org/10.1007/s10854-020-04673-0

Zheng, L. J., Wang, C. Y., Fu, L. Y., Yang, L. P., Qu, Y. P., & Song, Y. X. (2012). Wear mechanisms of micro-drills during dry high speed drilling of PCB. *Journal of Materials Processing Technology*, *212*(10), 1989–1997. https://doi.org/10.1016/j.jmatprotec.2012.05.004

Zheng, L. J., Wang, C. Y., Song, Y. X., Yang, L. P., Qu, Y. P., Ma, P., & Fu, L. Y. (2011). A review on drilling printed circuit boards. *Advanced Materials Research*, *188*(December 2015), 441–449. https://doi.org/10.4028/www.scientific.net/AMR.188.441

Zheng, L., Wang, C., Zhang, X., Huang, X., Song, Y., Wang, K., & Zhang, L. (2016). The tool-wear characteristics of flexible printed circuit board micro-drilling and its influence on micro-hole quality. *Circuit World*, *42*(4), 162–169. https://doi.org/10.1108/CW-08-2015-0040

Zheng, L., Wang, C., Zhang, X., Song, Y., Zhang, L., & Wang, K. (2015). The entry drilling process of flexible printed circuit board and its influence on hole quality. *Circuit World*, *41*(4), 147–153. https://doi.org/10.1108/CW-11-2014-0054